Andrey W. Golubkov

TEMPERATURE DEPENDENT CHARACTERIZATION OF CHARGE TRANSPORT IN ORGANIC THIN FILM TRANSISTORS

Diploma thesis

Supervisor:

Ao.Univ.-Prof. Dipl.-Ing. Dr.techn. Egbert Zojer

Institute of Solid State Physics,
GRAZ UNIVERSITY OF TECHNOLOGY

November 13, 2008

Andrey W. Golubkov

Temperaturabhängige charakterisierung von Ladungsträgertransportvorgängen in organischen Dünnschichttransistoren

Diplomarbeit

Betreuer:

Ao.Univ.-Prof. Dipl.-Ing. Dr.techn. Egbert Zojer

Institut für Festkörperphysik,
Technische Universität Graz

November 13, 2008

It gets worse. I have, before now, waited for a pen to perform a macro.

Terry Pratchett, alt.fan.pratchett

Acknowledgement

This diploma work was done under the supervision of Egbert Zojer. I would like to thank for his brilliant mentoring and his dedicated and friendly support.

Peter Pacher introduced me into the experimental handling and Marco Marchl together with Harald Etschmaier accompanied me throughout my diploma work, I'm greatfull for their help. I also want to thank the members of theoretical group of Egbert Zojer for the pleasant time.

Moreover, I would like to thank Heinz-Georg Flesch for the XRR measurements, Adolf Winkler for the permission to use his AFM equipment, Roland Resel for the heating stage, Harald Kerschbaumer and Birgit Kunert for stuff in the laboratory, Robert Krauß for his patience and help in the workshop and Paul Frank for his advices.

I want to thank my family, and all the friends from the student council.

This research was supported by a grant from the FWF (Research Project cluster 0700 - Research Project No. P19959-N20).

Abstract

In the present work charge carrier transport in semiconducting polymers is investigated. Two samples of regioregular poly(3-hexylthiophene) (RR-P3HT) with different molecular weight and one RR-P3HT based co-polymer are used to build thin film transistors. These devices are then electrically characterized at temperatures ranging from 80 - 300 K. Charge carrier mobilities are extracted from these measurements and compared to predictions of various transport models that are present in the literature. They include: hopping models and mobility edge models. Additionally, the influence of the gate voltage on the mobility is discussed and the shift of the threshold voltage (zero voltage) caused by temperature is presented.

The investigated transistors consist of top source and drain gold contacts evaporated through a shadow mask on organic semiconductor films with 160nm SiO_2 as dielectric and highly doped Si as bottom gate. The semiconductor films were produced by spin coating RR-P3HT solutions in 1,2,4-trichlorobenzene onto the SiO_2 layers.

Kurzfassung

Die vorliegende Arbeit befasst sich mit dem Ladungsträgertransport in halbleitenden Polymeren. Zwei regioreguläre poly(3-Hexylthiophene) (RR-P3HT) mit verschiedenen Molekulargewichten und ein Copolymer das zu 90 % aus RR-P3HT besteht, wurden benutzt um Dünnschichttransistoren herzustellen. Diese wurden im Temperaturbereich von 80 K bis 300 K elektrisch charakterisiert. Aus den gemessenen Strom- Spannungskurven wurde die Mobilität der Ladungsträger ermittelt und mit den Vorhersagen verschiedener Ladungsträgertransportmodellen verglichen. Zu den in der Literatur gefundenen Modellen gehören sogenannte Hopping und Mobility Edge Modelle. Zusätzlich wurde der Einfluss der Gatespannung auf die Mobilität diskutiert und es wurden temperaturabhängige Schwellspannungen präsentiert.

Die untersuchten Transistoren wurden folgendermaßen angefertigt: Auf ein hochdotiertes Si Substrat mit einer thermisch hergestellten SiO_2 Schicht wurde eine Lösung aus RR-P3HT in 1,2,4-Trichlorobenzol durch Rotationsbeschichtung aufgebracht. Auf den so entstandenen Halbleiterfilm wurden Drain- und Sourcekontakte aus Gold aufgedampft.

Contents

Chapter 1

Introduction

Organic semiconductors are a new class of material which combine the electrical properties of conventional inorganic semiconductors and the versatility of organic chemistry. From these materials it is possible to produce devices like light emitting diodes (LEDs),[32] field effect transistors[26] and solar cells[20, 24] with performances approaching their inorganic counterparts. Their production is far more customizable, organic materials can be deposited on almost all kinds of substrate like ITO, glass or flexible plastic foils. They can be structured by photolitography, soft lithography[63] and ink-jet printing[56] without the need of aggressive chemical substances and with low energy costs. Small matrix displays driven by LEDs have already been on the market for severall years, large area organic LED displays are on the way and organic radio frequency identification tags and chemical sensing devices are proposed.[16]

Although there is very much interest and high market potential in organic semiconductors, some fundamental physical questions remain unresolved. Electronic properties of single crystal inorganic semiconductors can be calculated while, the situation is more difficult for less well defined organic semiconductors especially in the case of semiconducting polymers. Instead of atoms in a periodic lattice with low concentration of doping and impurities a far more complicated picture is present. Soluble semiconducting polymers can react chemically with their surroundings and form different morphological structures depending on ambient conditions and their deposition technique. This reflects in variation of charge carrier mobility, memory effects, contact resistances and optical properties.

The scope of this work is the electrical characterisation of field-effect transistors based on the semiconducting polymer poly(3-hexylthiophene) (P3HT) at temperatures ranging from 80 K up to room temperature. Base on these data appropriate charge carrier transport models can be selected. Three different P3HT samples are investigated and then compared to publications from other groups.

This diploma thesis is structured as follows: in the first part, the function of the field effect transistor (FET) is explained, since FETs are used to probe the electrical properties of P3HT. The second part deals with various charge transport models found in the literature; their assumptions and predictions are summarized and compared. In the third part, morphology, optical and electric properties measured by other groups who used P3HT are discussed; this is a challenging task, considering all the degrees of freedom in fabricating organic FETs. Our own cryostatic measurements accompanied by some supplementary experiments are presented in part four.

Part I

Operation of organic field effect transistors

Chapter 2

General overview

In (Fig. 2.1) a sketch of an organic field effect transistor (OFET) is given. The transistor consists of several thin layers; therefore, it's also often referred to as organic thin film transistor (OTFT).[1] The transistor has 3 terminals, source drain and gate. The semiconducting channel is located between source and drain. It has a length L and a width W. Usually the length is much smaller than the width $L \ll W$.

It is the convention to keep the source at ground potential. Drain and gate voltage can be applied. The gate volage has direct impact on the varying charge distribution inside the channel. Depending on the charge density in the channel, a drain current I_D can flow driven by the drain source voltage V_{DS}. In short, I_D can be switched on and of by V_{GS}. The gate current I_G should be zero for an ideal SiO_2 insulating layer, but a leaking current is always observed in real devices.

---

[1] To be more precise, there also may be differences in the electric operation. In an OTFT with a very thin organic semiconductor film, charges are injected from the electrodes into the accumulation layer, when gate voltage is applied. In an OFET with a possibly higher thickness of the organic semiconductor, charges can be accumulated directly from the organic semiconductor bulk.

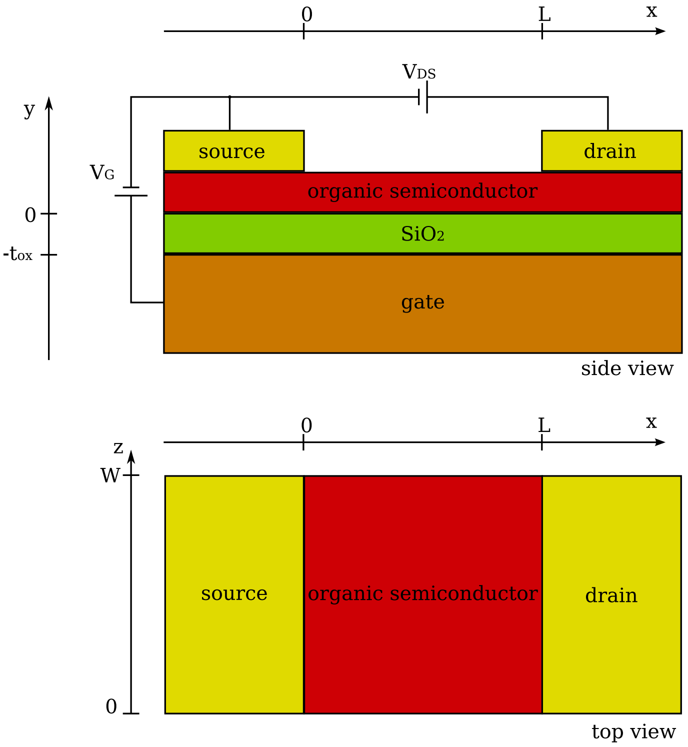

Figure 2.1: Geometry of an organic thin film transistor. Dimensions are not to scale.

Chapter 3

Metal oxide semiconductor structure

Models used for OTFTs are derived from models used for classical inorganic FETs. In this chapter, basic electrostatic equations are used to describe some characteristic of FETs. Especially, the interactions of the three layers, metal, oxide and semiconductor (MOS) are discussed, because they are very similar to those in organic FETs.

3.1 MOS working regimes

First, the charge distribution in the channel is evaluated. Note, that the following discussion is, strictly speaking, only valid for inorganic semiconductors, but the results can be adapted for organic semiconductors.

Starting with a classical 1D structure of the metal, oxide and (silicon) semiconductor layer (MOS) the electrostatic profile can be calculated. The structure of the channel crossection in devices used in this work (Fig. 3.1) is simmilar to this MOS structure. In our case, the first layer is highly doped silicon (metal), the second layer is SiO_2 (oxide) and the third layer is an organic semiconductor (semiconductor). In the following analysis, the terms from the inorganic semiconductor science are used, since they are derived of comprehensive literature in that field. P-type semiconductors are used for the explanations since only holes can be effectively injected into the polymer used in our experiments.

The qualitative situation in a classical MOS layer structure is showed in Fig. 3.2. The charge sheet on the metal side and accumulated holes, depletion region and the depletion layer on the semiconductor side are controlled by the so called gate body voltage V_{GB}. In our devices the body potential of the semiconductor layer is assumed to be identical to the source potential. The source contact is grounded for our setup, therefore, V_{GB} is identical to V_G. Numerical simulations, that were done by Possaner et al.,[47] show, that the potential in TFT devices is of a more complicated shape, but for simple calculations the above approach is used in the following.

There are several working regimes in a MOS structure:

Accumulation: Starting with negative gate voltages an electron charge layer develops at the metal insulator interface and holes are accumulated on the other side of the insulator.

Flatband: By increasing V_G the absolute charge decreases on both sides like in a capacitor. When V_G reaches V_{FB} no charges are present on both sides.

Depletion: At gate voltages between flatband and zero a depletion region develops at the insulator semiconductor interface.

Zero bias: At zero gate voltage the build in voltage V_{FB} determines the charge distribution.

Depletion: The depletion width increases at positive V_G until V_T is reached.

Threshold: The threshold voltage V_T specifies the point at which an inversion layer at the semiconductor insulator interface emerges.

Inversion: Gate voltages higher than V_T lead to a higher electron concentration in a very thin layer at the semiconductor insulator interface, while the depletion region width doesn't change much. Inversion regime is not possible in organic semiconductors, because they do not have an electronic band structure.

For quantitative discussion the electronic situation must be solved. First the distribution of charge and potential is calculated. Then the influence of the gate voltage is examined.

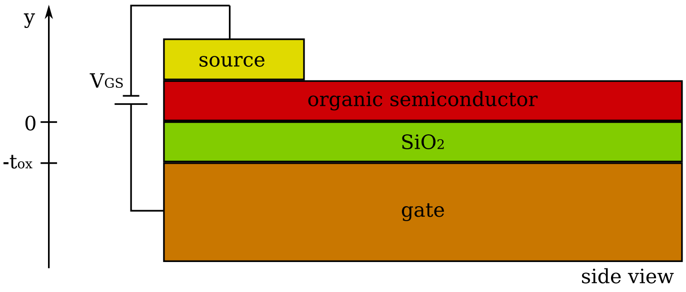

Figure 3.1: Geometry of an organic thin film transistor.

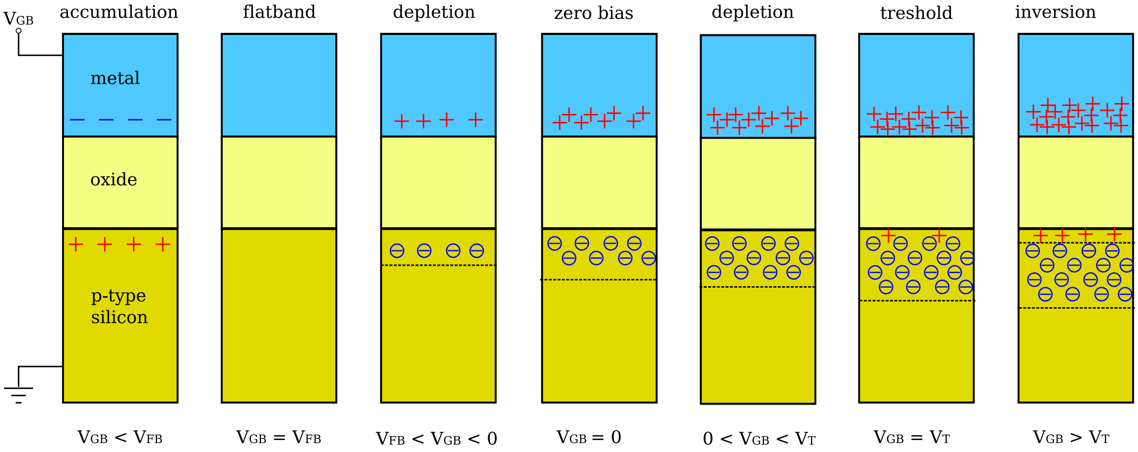

Figure 3.2: Different regimes in a classical MOS layer structure depending on gate voltage.

3.2 Zero bias

At zero bias $V_{GS} = 0$ (metal) gate and (body) p-type semiconductor contacts are electrically connected. The oxide insulates the gate from the semiconductor, but diffusion and drift current can flow through a connecting wire. The highly conductive metal side accepts no space charge, only a sheet charge in the vicinity of the oxide is possible. The oxide does not conduct at all; there are no free charge carriers in the oxide bulk, so it does not contribute to space charge. The semiconductor can have volume charge: majority carriers can be depleted, the immobile ionized dopands remain. Holes from the semiconductor diffuse into the electron rich metal[1] and create the depletion region and the sheet charge. Through this charge redistribution, a potential difference ϕ_{FB} and the related *build in voltage* $V_{FB} = q\phi_{FB}$ between metal and semiconductor emerges. ϕ_{FB} should be calculated here. The following derivations and plots in this section are based on MIT open course ware lecture notes (Microelectronic Devices and Circuits).[14]

The charge distribution is given by

$$\begin{array}{lll} \rho_0(y) = & Q_G\delta(-t_{ox}) & y \leq -t_{ox}, \\ \rho_0(y) = & 0 & -t_{ox} < y \leq 0, \\ \rho_0(y) = & -qN_a & 0 < y \leq y_{do}, \\ \rho_0(y) = & 0 & y_{do} < y, \end{array} \tag{3.1}$$

where ρ_0 is the space charge density at zero bias, Q_G is the sheet charge on the metal side, q is the elementary charge, t_{ox} is the depletion width and N_a is the dopand density of the semiconductor. The electric field is calculated using Gauss equation

$$E(y_2) - E(y_1) = \frac{1}{\epsilon}\int y_1 y_2 \rho(y)dy, \tag{3.2}$$

where ϵ is permittivity in vacuum and ρ is the space charge density. At the semiconductor oxide interface the electric field changes due to different permittivity of the two materials [2]

$$\epsilon_{ox}E_{ox} = \epsilon_s E_s. \tag{3.3}$$

Intergrating (3.1) gives

$$\begin{array}{lll} E(y) = & 0 & y_{do} < y, \\ E(y) = & -\frac{qNa}{\epsilon_s}(y - y_{do}) & 0 < y \leq y_{do}, \\ E(y) = & \frac{\epsilon_s}{\epsilon_{ox}}E(y = 0^+) = \frac{qN_a y_{do}}{\epsilon_{ox}} & -t_{ox} < y \leq 0, \\ E(y) = & 0 & y \leq -t_{ox}. \end{array} \tag{3.4}$$

Another integration leads to the potential

$$\begin{array}{lll} \phi(y) = & \phi_p & y_{do} < y, \\ \phi(y) = & \phi_p + \frac{qN_a}{2\epsilon_s}(y - y_{do})^2 & 0 < y \leq y_{do}, \\ \phi(y) = & \phi_p + \frac{qN_a}{2\epsilon_s}y_{do}^2 + \frac{qNay_{do}}{\epsilon_{ox}}(-y) & 0 < y \leq y_{do}, \\ \phi(y) = & \phi_n^+, & \end{array} \tag{3.5}$$

---

[1] In our case the "metal side" of the MOS structure was a highly doped Silicon substrate

[2] Relative permittivity ϵ was 3.9 and 3 for the oxide and our P3HT organic semiconductor respectively.[10]

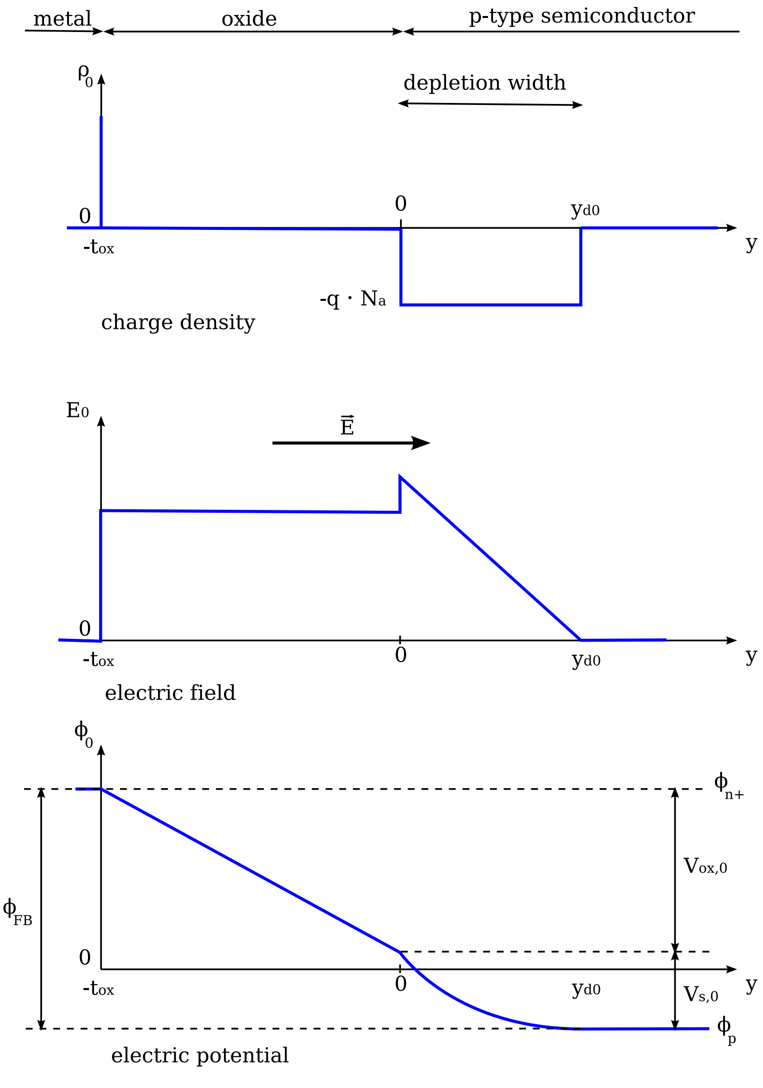

Figure 3.3: Charge density, electric field and electric potential in a MOS structure at zero gate voltage.

where ϕ_p is the potential deep inside the semiconductor and ϕ_n^+ is the gate potential. The potential drop across the whole structure under zero bias is called build in potential ϕ_{FB}.

$$\phi_{FB} = \frac{qN_a}{2\epsilon_s} y_{do}^2 + \frac{qN_a y_{do} t_{ox}}{\epsilon_{ox}} \tag{3.6}$$

With a reference potential $\phi = 0$ at $n_0 = p_0 = n_i$ (ϕ is zero in an undoped semiconductor), ϕ_n^+ is given by the Boltzmann relation

$$\phi = -\frac{kT}{q} \ln \frac{p_0}{n_i} \tag{3.7}$$

Also ϕ_{FB} equals the difference in the workfunction on the 'metal' side and the Fermi-energy on the semiconductor side. Fig. 3.4 shows the energies for the MOS structure in the flatband condition. This flatband condition is achieved by applying a negative voltage equal to V_{FB} to the gate.

$$\phi_{FB} = \phi_M - \phi_s = \phi_M - \chi - \frac{E_g}{2q} - \frac{k_b T}{q} ln \frac{N_a}{n_i}, \tag{3.8}$$

where ϕ_M is the metal side workfunction and can be set equal to the electron affinity of the highly doped silicon gate which is 4.05 eV. χ is the electron affinity of the semiconductor, E_g is the gap energy of the semiconductor, N_a is the acceptor dopand density and n_i is the intrinsic carrier density of the semiconductor. The associated build in voltage equals roughly $q\phi_{FB} \approx -1\,\mathrm{V}$ for the organic semiconductor used in this work. This is a small value for our test setup, but it should affect low voltage circuits in industrial applications.

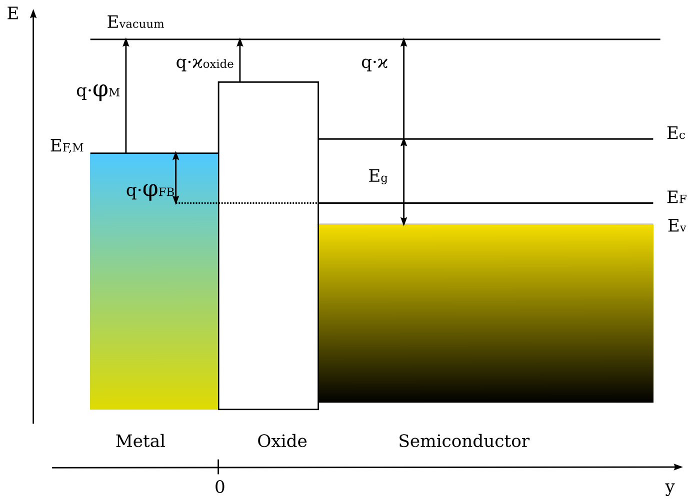

Figure 3.4: Energy levels of a MOS structure under flatband conditions.

Chapter 4

Model for organic FETs

In this chapter, a model for organic FETs is presented and differences to conventional MOSFETs are emphasized. It is based on the work of Horowitz et al.[18] Organic FET and conventional TFT work in accumulation regime. For hole only FETs, the gate is negatively biased in order to inject charge carriers with gradually onsetting drain current which increases with the number of charge carriers. When no V_G is applied, the carrier density n has some small value depending on intentional doping or impurities; therefore, some small conductivity still exists between source and drain. There does not exist a highly insulating depletion layer as in inorganic MOSFETs. Another consequence is that since no depletion regime must be "overcome" the threshold voltage should be zero. This is not he case for real world OFETs, but the threshold has other origins than in inorganic MOSFETs.

For the following calculations it is assumed, that holes are the majority charge carriers. Most organic semiconductor behave as p-type material, because of effective trapping of electrons at the semiconductor-SiO$_2$ interface[12] and because of better alignment of HOMO levels relative to the fermi energy of gold.[1] In order to develop the model two (accumulation) regimes are defined, linear regime with $|V_G| > |V_{DS}|$ and saturation regime with $|V_G| < |V_{DS}|$.

4.1 Linear regime

The elemental resistance along the channel in the x-axis (Fig. 2.1) direction is

$$dR = \frac{1}{W\mu Q(x)}dx, \tag{4.1}$$

where W is the channel width, μ is the mobility and $Q(x)$ is the surface charge density at x. Horowitz and coworkers differentiate between two kinds of charge:

Bulk charge , Q_0, is the surface charge density calculated from the density of free charges in the bulk n_0, the semiconducting layer thickness d_s and the elemental charge q by

$$Q_0 = qn_0d_s \tag{4.2}$$

---

[1] Gold is frequently used as electrode material for source and drain contacts.

Induced charge , Q_s, is injected by gate biasing. Similar to a capacitor, charge carriers accumulate on both sides of the insulator layer and forms charge layers at the interfaces.

$$Q_s = -C_i(V_G - V_{FB} - V(x)) \tag{4.3}$$

Here C_i is the capacitance per unit area of the insulating layer, V_G is the gate voltage, V_{FB} is the build in voltage which accounts for work-function difference between the gate material and the semiconductor and $V(x)$ is the voltage that accounts for the drain bias V_{DS}. The build in voltage can be estimated with equation (3.8). For OFET with highly doped silicon as gate and P3HT as semiconducting material it is

$$V_{FB} \approx q\phi_{HOMO}(\mathrm{Si}) - IP(\mathrm{P3HT}) \approx 4.05\,\mathrm{V} - 5.2 \pm 0.2\,\mathrm{V} \approx -1 \pm 0.2\,\mathrm{V},$$

where $\phi_{HOMO}(\mathrm{Si})$ is the HOMO energy of highly doped silicon and $IP(P3HT)$ is the ionisation energy of the organic semiconductor poly-(3-hexylthiophene). $IP(\mathrm{P3HT})$ was calculated by Sainova et al.[48] Note that V_{FB} is fairly small. Since voltages are much higher in our experiments (up to 100 V) this value is within fitting errors.

As usual, the *gradual channel* approximation is applied. It is valid when the electrical field perpendicular to the substrate in y direction largely exceeds the one along the channel in x direction. The former electrical field comes from the gate bias and the latter originates from the drain source voltage. The assumption holds when $L \gg d_s$ for V_G and V_{DS} of the same order of magnitude. In this case $V(x)$ gradually decreases from V_{DS} to 0 as one moves from the drain position to the source.
Now (4.1) is multiplied by I_D

$$dV = I_D dR = \frac{I_D}{W\mu(Q_s(x) + Q_0)} dx, \tag{4.4}$$

and by using the equations (4.2) and (4.3) it can be integrated along the channel from $x = 0$ to $x = L$ and $V = 0$ to $V = V_{DS}$:

$$I_D \int_0^L dx = I_D L = W \int_0^{V_D} \mu \left[C_i(V_G - V_{fb} - V) + qn_0 d_s\right] dV \tag{4.5}$$

For a constant and not gate voltage dependent mobility equation (4.5) gives

$$I_D = \mu C_i \frac{W}{L}\left[(V_G - V_0)V_{DS} - \frac{V_{DS}}{2}\right], \tag{4.6}$$

with the *zero voltage* V_0 given by

$$V_0 = \frac{qn_0 d_s}{C_i} + V_{FB}. \tag{4.7}$$

Equation (4.6) is similar to that used for inorganic MOSFETs in linear inversion regime. In the case of MOSFETs, V_0 would be equal to the threshold voltage V_t in inversion regime. For OFETs the term V_t is not used, because they are operated in accumulation regime and so the assumptions in the definition of V_t

in the MOSFET world do not apply here. As sugested by equation (4.7) V_0 is proportional to the free charge carrier density n_0 (if some exists in the bulk). Also, V_0 is lovered by a the small negative build in voltage V_{FB}. Another reason for non-zero V_0 could be deep traps that trap some amount of charge carriers before conduction starts. This would equal to some negative n_0 and consequently V_0 values. If some residual charge carrier density n_0 is present, it can be depleted by applying positive gate voltage.

From equation (4.6) the field effect mobility in the linear regime can be estimated from the slope of a linear fit, when I_D is plotted against V_G in the region where $|V_G| > 2 * |V_{DS}|$.

4.2 Saturation regime

When the drain source voltage exceeds the gate voltage $|V_{DS}| > |V_G|$ the accumulation layer is depleted near the drain (Fig. 4.1). Instead of a layer of free charge carriers at the whole interface, a depletion region emerges which reduces the effective thickness of the semiconductor layer. No free carriers are present at the interface, and bulk conductivity is lowered in the depletion region. The current in the depletion region can not be calculated by (4.1), instead it's governed by bulk conductivity with reduced d_s:

$$I_D = Wqn_0\mu(d_s - W_d(x))dV \tag{4.8}$$

with the thickness of the depleted layer W_d (in y direction)

$$W_d(V) = \frac{\varepsilon_s}{C_i}\left[\sqrt{1+\frac{2C_i^2(V(x)-V_G}{qN\varepsilon_s}}-1\right], \tag{4.9}$$

where ε_s is the permittivity of the semiconductor and N is the concentration of dopands. Horowitz et al. note that N can differ from n_0.

In the following, the saturation current is calculated by dividing the channel into two regions and by integrating them separately, as suggested by Brown et al.[5] In the first region, the accumulation layer dominates and at some point x where $V_G = V(x)$ the depletion region starts. Equation (4.5) now becomes

$$I_D L = W\int_0^{V_G}\mu\left[C_i(V_G - V)\right]dV + W\mu qn_0\int_{V_G}^{V_{Dsat}}(d_s - W_d(V))dV, \tag{4.10}$$

here V_{Dsat} is defined as the drain source voltage, at which the charge density of the channel at the point $x = L$ is zero ($Q(L) = 0$). This occurs, when the depletion layer at the drain electrode extends over the whole semiconducting layer $W_d(L) = d_s$. In order to estimate the second term Horowitz et al.[25] change the integration variable from V to W_d using equation (4.9). The drain current (4.10) now reads

$$I_D L = W\int_0^{V_G}\mu\left[C_i(V_G - V)\right]dV + W\mu\frac{q^2n_0N}{\varepsilon_s}\int_0^{d_s}(d_s - W_d)\left(W_d + \frac{\varepsilon_s}{C_i}\right)dW_d, \tag{4.11}$$

and after doing the integration

$$I_D = \mu\frac{W}{L}\left[C_i\left(\frac{V_G^2}{2} - V_0V_G\right) + \frac{q^2n_0N}{\varepsilon_s}\frac{d_s^3}{6}\left(1 + 3\frac{C_s}{C_i}\right)\right]. \tag{4.12}$$

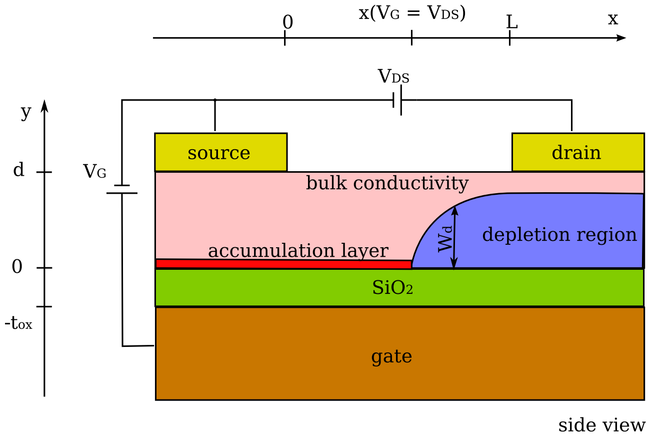

Figure 4.1: OFET in saturation regime. The accumulation layer does not stretch all the way across the channel, instead a depletion region forms starting at x where $V_G = V_{DS}$.

Using further approximations, namely that the capacitance of the semiconductor layer $C_s = \varepsilon_s/d_s$ is higher then the capacitance of the insulator layer C_i and that $n_0 = N$ Horowitz and co-workers derive the final equation for the saturation current:

$$I_D = \frac{W}{2L}\mu C_i \left(V_G - V_0\right)^2 . \tag{4.13}$$

Again, the mobility can be extracted from the plot of I_D vs. V_G this time for lower gate voltages $|V_G| < |V_{DS}|$. In practice $\sqrt{I_D}$ and not I_D is plotted, in order to make simple linear fits.

A comprehensive discussion of the OFETs in saturation regime and a more detailed derivation of (4.13) can be found in the publications of Horowitz et al.[25] and Brown et al.[5]

Part II

Charge transport models

In metals and conventional semiconductors, mobility is limited by phonon scattering. This is typically not the case in organic semiconductors, where the mobility is much lower. The mean free path of the carrier can be calculated from the mobility with

$$L = \frac{\mu m^{\star} \nu_c}{e}. \tag{4.14}$$

Here, $m^{\star}$ is the effective mass of the charge carrier and ν_c is the thermal velocity

$$\nu_c = \sqrt{\frac{3k_bT}{m^{\star}}}. \tag{4.15}$$

According to this equations, even one of the highest mobilities reported for P3HT by Chang et al.[9] ($\mu \approx 0.1\,\mathrm{cm^2/Vs}$) correspond to a mean free path of 0.01 nm (at room temperature, and when $m^{\star}$ is assumed to be equal to the mass of a free electron). That value is lower than the interatomic distance, therefore other conducting mechanisms than for conventional semiconductors must be considered.[26]

Organic semiconductor polymer films consist of cristallites with high degree of spatial disorder, as seen from AFM images and diffraction analysis. The conductivity is limited by defects caused by this disorder where the delocalized wave function is interrupted. Examples for disorder are bends of the crystalline nanorods and cross or merging points of the cristallites. Even single crystal organic semiconductors like rubrene exhibit thermally activated behavior bacause of high disorder.[43]

Conduction is, therefore, governed by trap states; these are states where charges are localized for some finite time in contrast to delocalized (extended) conduction band. The energy of these trap states lies in the band gap, between HOMO and LUMO. There are several possible conducting mechanisms, where localized states are included.[57] They can be roughly categorized into two groups:

Extended state conduction Carriers are thermally activated from the trap states from the Fermi energy into the conduction band which lies above the so called mobility edge (that is, into extended state). Mobility in the conduction band has a non zero value. Trapped charges have zero mobility.[57]

Hopping conductivity Conduction happens by hopping/tunneling between localized traps. Tunneling between states is only slightly temperature dependent, but this changes when polaron effects are included. Increased density of traps promotes a higher tunneling rate because of reduced mean distance between the sites. The carriers are completely localized at the traps, no extended state exists.[57]

In the following chapters transport models which are based on these mechanisms are explained in more detail.

Chapter 5

Extended state models

The effective mobility in the extendend state models is governed by the ratio of free and trapped carriers. The percentage of trapped charges depends on the density of traps and on the overall number of (intrinsic or injected) charge carriers. A trapped charge can be thermally activated into the extended (delocalized) state; to estimate the required activation energy, the energetic distributions of traps must be considered. In the following pages one numerical and one analytical model are presented.

5.1 Mobility edge (ME) model

This section is largely based on a paper from Salleo et al.[49]

In the ME theory, charge carriers are classified in two groups: mobile carriers and trapped carriers. These two possible classes of charge carriers are separated by a defined energy, the so called mobility edge (ME). charge carriers Mobile carriers are delocalyzed in individual crystal grains, whereas trapped carriers are located in disordered grain boundaries. Hopping between trap states is not considered in the ME model.

To make the following explanations more understandable, only hole conductivity is taken into account. The mobility edge can be set to $E = 0$ without loss of generality. The DOS is assumed to be band-like[1] for negative energies and exponentially decreasing for positive energies:

$$\begin{aligned} D(E) = &\ \tfrac{N_{tot}}{E_b\sqrt{E_v}}\sqrt{E_v - E} && E < 0, \\ D(E) = &\ \tfrac{N_{tot}}{E_b}e^{-\frac{E}{E_b}} && E \geq 0, \end{aligned} \tag{5.1}$$

with N_{tot} beeing the total concentration of tail states and the E_b specifying the width of the exponential tail. Completely randomly distributed trap states would be explained more accurately by a Gaussian distribution, but this would make calculations more difficult. The exponential approximation is generally accepted for organic semiconductors, as stated by Salleo et al.[49] Holes in the conducting band have constant intrinsic mobility μ_0, while trapped charges in the exponential tail are spatially fixed. The parameter E_v is used to shift the band-DOS along the energy axis in order to avoid discontinuities at $E = 0$.

---

[1] The band- DOS obeys the $D(E) \sim \sqrt{E}$ law for the 3D electron gas.

When $|V_G|$ is increased, more charge carriers are induced into the accumulation layer. At first, energetically favorable states in the band tail are filled up. With further rising $|V_G|$ the hole distribution reaches into the band-like DOS, and the mobile charge carrier density increases, leading to a higher conductivity. In Fig. 5.1 typical DOS and charge carrier densities are plotted.

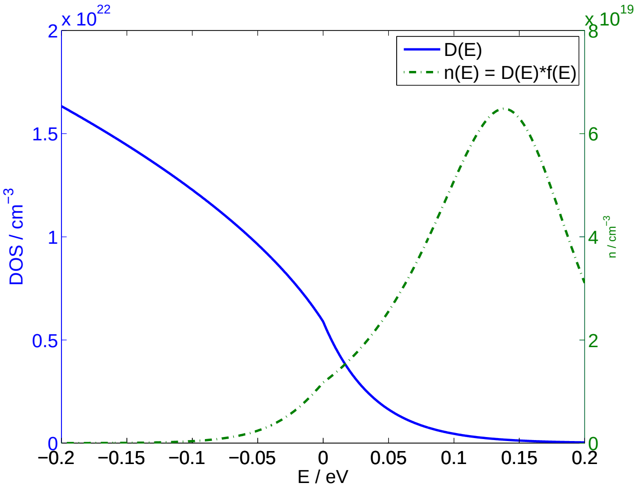

Figure 5.1: DOS and carrier density for holes as a function of the energy in the ME model. The carrier density is calculated for $T = 280\,\mathrm{K}$ and $E_F = 0.15\,\mathrm{eV}$. Only charge carrier $n(E < 0)$ contribute to conductivity.

Quantitatively, the Fermi energy must be calculated from

$$N_{tot}(V_G) = \frac{C_i|V_G - V_0|}{h} = \int_{-\infty}^{+\infty} D(E) f(E_F, E) dE \tag{5.2}$$

and

$$f(E_F, E) = 1 - \frac{1}{1 + \exp\left(\frac{E - E_F}{k_b T}\right)}, \tag{5.3}$$

where C_i is the capacity of the gate dielectric, V_0 is the zero voltage, h is the accumulation layer height (assumed to be equal 1 nm), $D(E)$ is taken from (5.1) and $f(E_F, E)$ is the Fermi-Dirac distribution for holes. This can be done numerically. When E_F is known, the charge carrier density in the band can be found by integrating the band part of the distribution:

$$N_{mob}(V_G, T) = \int_{-\infty}^{0} D(E) f(E_F, E) dE. \tag{5.4}$$

Only free charges account for effective mobility:

$$\mu_{eff}(V_G, T) = \mu_0 \frac{N_{mob}}{N_{tot}}. \tag{5.5}$$

Now the drain current of a FET in the linear regime can be calculated as usual:

$$I_d = \frac{W}{L} \mu_{eff}(V_G, T) V_{DS} N_{tot} = \frac{W}{L} \mu_{eff} V_{DS} C_i (V_G - V_0). \tag{5.6}$$

The mobility is dependent on two external parameters, the temperature and the gate bias. Increased $|V_G|$ forces the Fermi energy towards the band edge, promoting the carrier population in the conducting band. On the other hand, temperature affects the width of the Fermi Dirac distribution. Therefore higher temperatures give a broader decline into the band. This also increases the probability of band state occupation.

The drawback of the ME model is, that calculations can not be done analytically. Especially the dependence of μ_{eff} on the temperature can't be written explicitly. Implicitelly it is included in the integral over the Fermi-Dirac distribution. Nevertheless, impressive fitting results of transfer curves for P3HT at different temperatures have been published by Chang et al.[9]

5.1.1 Expansions to the ME model

The single exponential tail can be replaced by a double exponential, denoting shallow and deep traps. This gives better fit results below the zero voltage of the transfer curves: at low $|V_G|$ the Fermi energy is located further in the band gap; there, deep traps play an important role.[9] An example for a double exponential tail is given in Fig. 5.2

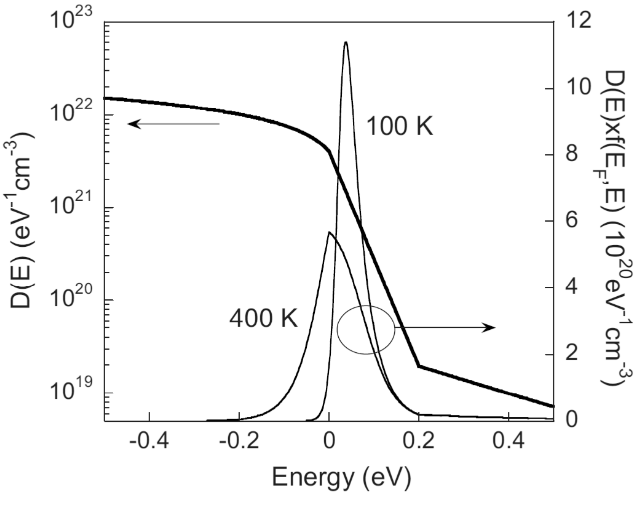

Figure 5.2: DOS and charge carrier density for 400 K and 100 K that fit P3HT transistors. This figure is taken from Chang et al.[9]

Mobility in the conduction band μ_0 is assumed to be a constant parameter like for the simple ME model. For these free carriers polaronic properties can also be included. When charge carriers are not delocalyzed over neighboring molecules, energy for molecular reorganisation must be taken into account. Thr polaron activation energy E_a is required to overcome this reorganisation. It can be extracted from charge modulated spectra (CMS) measurements.[9] The equation for the overall mobility 5.5 is modified by an additional term:

$$\mu_{eff}(V_G, T) = \mu_0 e^{-\frac{E_a}{k_b T}} \frac{N_{mob}}{N_{tot}}. \tag{5.7}$$

Inclusion of the polaron effect only affects the temperature, but not the gate bias dependence of the mobility. Note that the contribution of the polarons to the activation energy is not high enough, to describe the temperature dependence of the conductivity as a stand alone model.

Dhoot et al.[15] incorporate electric-field assisted carrier tunneling between occupied localized states. According to their observations, a transition from insulator to metallic conducting behaviour happens at low temperature and high electric fields between source and drain ($E \approx 20\,{}^{\mathrm{kV}}/_{\mathrm{cm}}$), when high transition probability

$$p \approx \exp\left(-2\sqrt{\frac{\phi_b - eEb}{\phi_b}}\right) \tag{5.8}$$

is reached. Here ϕ_b is the barrier height, b is the barrier width.

5.2 Multiple trapping and thermal release (MTR) model

This section is based on a review by Gilles Horowitz.[26]
The MTR model, as explained by Horowitz, is a derivative of the ME model. In order to make analytical predictions for temperature dependencies approximations must be accepted. Especially distributions must be simplified in order to go beyond numerical calculations.

5.2.1 Single trap energy

As in the ME model, two charge carrier species (that are injected by $|V_G|$) exist in the MTR model. Trapped carrier reside at locally fixed trap sites, while carriers in the transport band are free to move around.

In the simples case, only trap sites with one single energy E_t and density N_t exist. Charge carriers can either reside at trap sites or be thermally released into the conductive band and move there according to the electric field (Fig. 5.3). It is required that $N_t \gg \sigma$ where σ is the induced charge carrier density. Otherwise the Boltzmann statistics would not hold, as the traps would be completely filled up at some gate bias.

The total charge concentration splits into free carriers

$$n_f = N_c e^{-\left(\frac{E_c - E_F}{k_b T}\right)} \tag{5.9}$$

and trapped carriers

$$n_t = N_t e^{-\left(\frac{E_t - E_F}{k_b T}\right)}. \tag{5.10}$$

Here, N_c is the effective density of states of the transport band edge and E_c is the transport band edge energy. The effective mobility is then given by the product of μ_0 and the ratio of free to trapped carriers:

$$\mu_{eff} = \mu_0 \frac{n_f}{n_f + n_{t0}} = \mu_0 \frac{1}{1 + \frac{N_t}{N_f} e^{\frac{E_C - E_T}{k_b T}}} \approx \mu_0 \frac{N_t}{N_c} e^{-\frac{E_C - E_T}{k_b T}}. \tag{5.11}$$

Note that there is no gate voltage dependence, and that mobility relates to temperature in Arrhenius fashion.

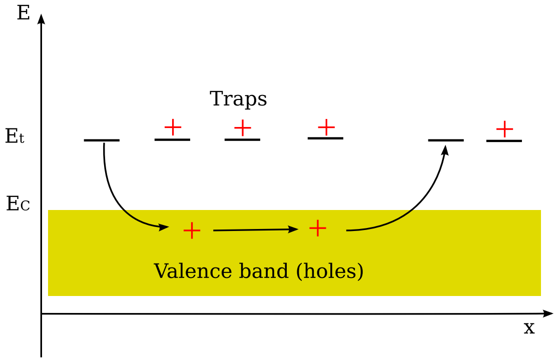

Figure 5.3: Traps with a single energy E_t are distributed randomly in the spatial dimension x. Holes can be either trapped, or move in the conduction band. Excitation into the band is thermally assisted.

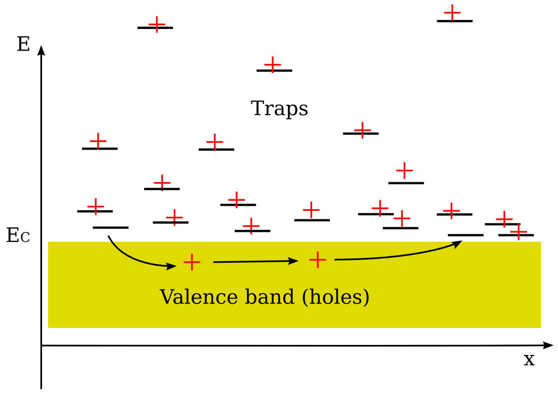

Figure 5.4: Traps with a exponential energy distribution and random spatial distribution. Holes can be either trapped, or move in the conduction band. Excitation into the band is thermally assisted and gate voltage dependent.

5.2.2 Distributed trap energy

Mobility becomes V_G dependent, when energy distributed traps are considered, as in the ME model. An exponentially distributed

$$D(E) = \frac{N_t}{k_b T_c} e^{-\frac{E}{kT_c}} \quad E > 0, \tag{5.12}$$

trap DOS is shown in Fig. 5.4. It can be handled analytically, when the Fermi-Dirac distribution is approximated by a step function. The hole conduction band edge energy is set to zero $E_c = 0$ for simplicity. The density of trapped charges is equal to the charge density induced by gate bias. It is assumed, that the total density of trap states N_t is higher than the density of induced charge carriers. So the induced holes fill up the tale states, until E_F is reached.

$$n_t = \int_{E_f}^{\infty} D(E)dE = N_t e^{-\frac{E_f}{k_b T_c}} = \frac{C_i(V_G - V_0)}{q}. \tag{5.13}$$

With this the Fermi energy can be solved:

$$E_f = k_b T_c \ln \left(\frac{C_i(V_G - V_0)}{qN_t} \right). \tag{5.14}$$

According to the Boltzmann statistics, charges can be thermally excited from the trap sites into the conduction band. The density of free charges is then

$$n_f = \int_{E_f}^{\infty} D(E) \cdot e^{-\frac{E}{k_b T}} dE = N_t \left(1 + \frac{T}{T_c}\right) \left(\frac{C_i(V_G - V_0)}{qN_t} \right)^{\frac{T_c}{T} - 1}. \tag{5.15}$$

Thr effective mobility is again calculated from the ratio of free to induced charges. For $n_t \gg n_f$:

$$\mu_{eff} \approx \mu_0 \frac{n_f}{n_t} = \frac{N_t \left(1 + \frac{T}{T_c}\right) \left(\frac{C_i(V_G - V_0}{qN_t} \right)^{\frac{T_c}{T} - 1}}{\frac{Ci(V_G - V_0)}{q}} = \mu_0 \left(1 + \frac{T}{T_c}\right) \left(\frac{C_i(V_G - V_0}{qN_t} \right)^{\frac{T_c}{T} - 2}. \tag{5.16}$$

The temperature prefactor can be neglected in the face of the more relevant exponent term:

$$\mu_{eff} \propto \left(\frac{C_i(V_G - V_0}{qN_t} \right)^{\frac{T_c}{T} - 2}. \tag{5.17}$$

As in the case of one single trap energy, mobility has Arrhenius temperature behavior, but there is also a power law dependence in $(V_G - V_0)$. Typical characteristic temperatures T_c and total trap densities N_t are in the range of $\approx 450\,\mathrm{K}$ and $\approx 4 \times 10^{20}\,\mathrm{cm}^{-3}$ respectively.[9]

Chapter 6

Hopping models

In this chapter, first tunneling and polaron hopping equations are reviewed. Later, those equations are embedded into different trap densities and occupation profiles. After solving this systems either analytically or numerical, dependencies of mobility on temperature, charge carrier concentration and electric field strength are given.

6.1 Tunneling

Tunneling of charge carriers from one localized state to another occurs when some overlap of the wavefunctions exists. Fig. 6.1 shows an example for tunneling between two states with different energies. R_0 is the typical delocalization radius of the charges with exponentially decreasing probability density. Higher overlap (decreased distance of the sites R and increased R_0) gives higher probability for tunneling. The energy difference leads to a temperature dependent term, since thermal activation is needed for tunneling into higher potential states. Probabilities for tunneling from site i to site j are given by

$$\gamma_{ij} = \begin{cases} \gamma_0 e^{-\frac{2R}{R_0}} e^{-\frac{E_j - E_i}{k_b T}} & \text{for } E_j > E_i, \\ \gamma_0 e^{-\frac{2R}{R_0}} & \text{for } E_j \leq E_i, \end{cases} \tag{6.1}$$

where γ_0 is some weakly temperature dependent material constant. This equation is often referred to as Miller-Abrahams formula.[36] The delocalization radius depends on the state energy:

$$R_0(E) = \sqrt{\frac{\hbar^2}{m(E - E_C)}} \tag{6.2}$$

where E_c is the conducting band edge energy (or some equivalent when no band conductivity exist). Note that tunneling conductivity between traps with the same energy is not temperature dependent. It could become the dominant charge transport mechanism at very low temperatures.

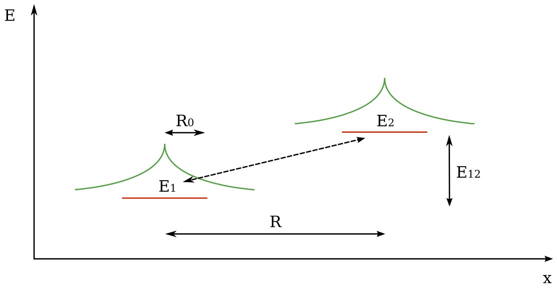

Figure 6.1: Tunneling of charge carriers between states with energies E1 and E2. R is the spatial distance of the two sites, E12 is the energy difference and R0 is the localization length. After R. A. Street.[57]

6.2 Polaron hopping

The polaron is a quasiparticle composed of a charge and some spatial deformation of the crystal induced by the electric field originating from the centre of the charge.[26] Additionally, the P3HT molecules can experience some distortion, when the occupation of their HOMOs or LUMOs change. For organic semiconducting polymers this manifests in a coupling of the charge with low-frequency phonon modes of the molecule.[52] In comparison to a plain charge, the polaron binding energy is lowered by E_P, which is one half of the reorganisation energy λ. If λ is sufficiently high, the charge is localized on the molecule, and the resulting polaron is called Holstein small polaron or molecular polaron (MP). On the other hand, if λ is low in comparison to the transfer integral t between two molecules, the polaron is delocalized. The transfer integral is a complicated function of the geometry of neighboring molecules. High t result from better overlap of the molecular orbitals. The criterion for molecular polarons is

$$2t < \lambda. \tag{6.3}$$

Otherwise, the transport happens bandlike and not by hopping.

The transport mechanism in the MP case is shown in Fig. 6.2. In order to hop from one molecule R to the molecule P the spatial configurations of the molecules must change from the equilibrium coordinates q_R and q_P to q_C. When the force constant of the oscillator is given by f, and the site energies are equal ($E_P = E_R$), the reorganisation energy reads:

$$\lambda = \frac{f}{2}(q_R - q_P)^2 \tag{6.4}$$

and the reorganisation energy part of the hopping barrier is

$$\Delta G = \frac{\lambda}{4} \tag{6.5}$$

as seen from Fig. 6.2. The transfer integral lowers the energy barrier, which results in

$$\Delta G = \frac{\lambda}{4} - t, \quad t < \lambda \tag{6.6}$$

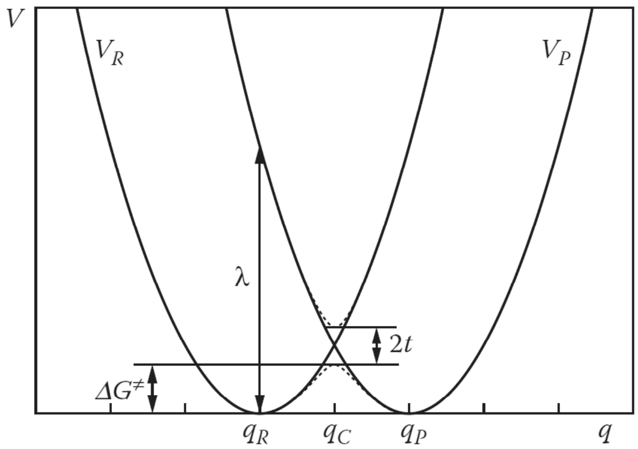

Figure 6.2: Potential energy V of two sites P and R depending on coordinates q that account for spatial deformation. λ is the reorganization energy, t is the transfer integral and $\Delta G^{/}=$ is the resulting barrier height. The equilibrium positions are q_R and q_P. The Energy at q_C must be spent for charge transfer. Figure taken from Horowitz.[26]

To overcome this barrier, even for $E_P = E_R$ thermal activation is required. In contrast to tunneling, polaron hopping leads to zero conductivity as the temperature approaches zero Kelvin.

The associated transition probability[17] as developed by Marcus is given by

$$W_{ij} \propto \frac{t^2}{\sqrt{4\pi\lambda k_b T}} \times \exp\left(-\frac{(E_i - E_j + FR_{ij} + \lambda)^2}{4\lambda k_b T}\right) \tag{6.7}$$

for zero field F and equal site energies $E_i - E_j$ this reduces to

$$W_{ij} \propto \frac{t^2}{\sqrt{4\pi\lambda k_b T}} \times \exp\left(-\frac{\lambda}{4k_b T}\right). \tag{6.8}$$

The hopping frequency is then estimated by the Einstein relation

$$\gamma_{ij} = \frac{qR^2}{k_b T} \times W_{ij}. \tag{6.9}$$

In contrast to the tunneling equation (6.1), polaron hopping (6.9) is more symmetric. For example, if the destination site energy is lower, the hop probability is not 100% but depends on thermal activation to overcome the reorganisation energy.

6.3 Variable range hopping

Models based on variable range hopping (VRH) include microscale information like overlap parameter and disorder induced width of the DOS, but mesoscale structures (like the size of the cristallites) are not taken into account.[50]

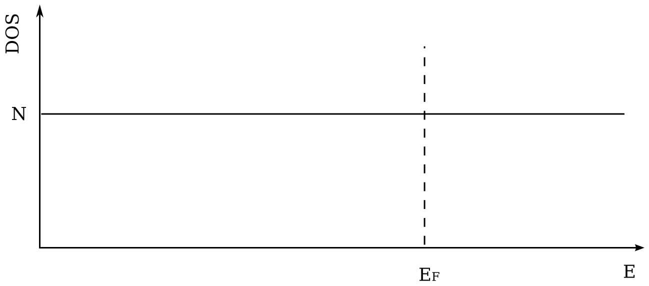

Figure 6.3: Constant density of (trap) states as used by Mott for his transport model. E_F denotes the Fermi energy.

The starting point for the VRH model is a highly disordered energetic and spatial configuration of the semiconductor. No long range ordering (translation symmetry) such as in Si single crystals is present. As there is no repetition of unit cells, no periodic potential and so no Bloch states exist, which would lead to some band structure with conduction bands.[58] Instead only localized states exist, described by two distributions:

energy distribution describes the DOS that gives the probability for a certain binding energy of a charge in a trap site.

spatial distribution accounts for the variable spacings of the traps sites with respect to the ideal repetitive points in a crystal.

These two types of disorder are also called *diagonal disorder* in the case of energy variance, and *off-diagonal disorder* in the case of positional disorder. The names originate from the hopping matrix of neighboring sites. Note that not all hopping models take spatial distribution into account.

Conduction happens through hopping between the states. It is assumed that coupling of the charge to molecular modes is weak (molecular deformation energy as in the polaron model is not considered), thus the activation energy reflects the energetic disorder of the sites.[4] Energy differences of the states result in absorption or emission of phonons. The probability for successful hopping is given by 6.1. The emission of phonons is necessary to remove excess energy, when hopping to a low energy trap site. The probability for emission is assumed to be equal to one, but if larger energy differences in the order of 2 eV are present, this approximation no longer holds. The mobility would then be more strongly temperature dependent.[3]

Mott has calculated the conductivity for a constant DOS (Fig. 6.3):

$$\sigma \propto e^{-\left(\frac{T_1}{T}\right)^{1/4}}, \tag{6.10}$$

with

$$T_1 k_b = \frac{128}{9} \frac{\pi \alpha^3}{N_F}, \tag{6.11}$$

where α is the size of the localized state and N_F is the density of states at the Fermi edge. A constant DOS might be a to crude approximation.[37]

Ambegaokar et al.[3] introduced percolation theory into this hopping model. They also modified the probability for hopping (6.1) by the electric field in a way, that electric potential is added to the trap energies. This yields:

$$\gamma_{ij} = \begin{cases} \gamma_0 e^{-\frac{2R}{R_0}} e^{-\frac{E_j - E_i + e\vec{E}\cdot\vec{R}}{k_b T}} & \text{for } E_j > E_i, \\ \gamma_0 e^{-\frac{2R}{R_0}} & \text{for } E_j \leq E_i, \end{cases} \tag{6.12}$$

where $\vec{E}$ is the electric field. The resulting conductivity has the same temperature dependence as (6.10),

$$\sigma \propto e^{-\left(\frac{T_0}{T}\right)^{1/4}}, \tag{6.13}$$

with a material constant

$$k_b T_0 = \frac{4\nu_c \alpha^3}{N_F} \tag{6.14}$$

where the dimensionless constant ν_c describes conductivity in a percolation system. For three dimensions it equals ≈ 4.

6.4 Bässler's model

Bässler's model is based on VRH with a trap state DOS approximated by a Gaussian function.[4] This shape is chosen because spectroscopic measurements on organic semiconductors show Gaussian distributions with typical widths of $\sigma = 500\,\mathrm{cm}^{-1}$ (60 meV) as measured for amorphous tetracene by Jankowiak et al.[28] The model is sometimes referenced as Gaussian disorder model (GDM). The DOS distribution is then given by

$$N(E) = \frac{N_t}{(2\pi\sigma)^2} e^{-\frac{E^2}{2\sigma^2}}, \tag{6.15}$$

where N_t is the total density of trap states per unit space, σ is the width of the Gaussian and E is the energy in respect to the maximum of the distribution.

Bässler assumes in his calculations, that the charge density is much lower than the density of sites. In this dilute system no charge-charge interaction occurs and the Fermi-Dirac statistics is irrelevant. When charges are placed into an otherwise empty DOS the mean energy equilibrates to

$$< E_\infty >= \frac{\int_{-\infty}^{\infty} E n(E) e^{-\frac{E}{k_b T}} dE}{\int_{-\infty}^{\infty} n(E) e^{-\frac{E}{k_b T}} dE} = -\frac{\sigma^2}{k_b T}, \tag{6.16}$$

as dictated by the Boltzmann statistics. In the long-time limit $n(E)$ becomes Gaussian and acquires the same width σ as the DOS. Bässler argues, that for $\sigma \approx 0.1\,\mathrm{eV}$ and $T = 295\,\mathrm{K}$ only a very small fraction of the DOS is filled. The fraction of states with energies lower than $\langle E_\infty(\sigma = 0.1\,\mathrm{eV}, T = 295\,\mathrm{K})\rangle = -4\sigma$ is given by

$$\frac{n_{E<\langle E_\infty\rangle}}{N_t} = \int_{-\infty}^{-4\sigma} N(E) dE \approx 3 \times 10^{-5}. \tag{6.17}$$

A charge at $\langle E_\infty\rangle$ would on average find far more sites, where thermal assistance is needed, than sites with lower energy. If all carriers would be located at $\langle E_\infty\rangle$, and when conduction would occur only at $E = 0$ in the center of the DOS, the transport activation energy would be $E_a = \frac{\sigma^2}{k_b T}$. So E_a would be temperature dependent, and the conduction mechanism would be similar to the MTR model with one single trap energy (page 24). Temperature dependent mobility would, however, have a non Arrhenius behavior:

$$\mu(T) = \mu_0 e^{-\left(\frac{\sigma}{k_b T}\right)^2}. \tag{6.18}$$

Bässler did Monte Carlo simulations, an observed such T^{-2} dependence. From fitting μ vs. T an effective transport energy, which lies below $E = 0$ could be found, resulting in a prefactor in the exponent of (6.18):

$$\mu(T) = \mu_0 e^{-\left(\frac{2}{3}\frac{\sigma}{k_b T}\right)^2}. \tag{6.19}$$

The conduction mechanism is shown in Fig. 6.4.

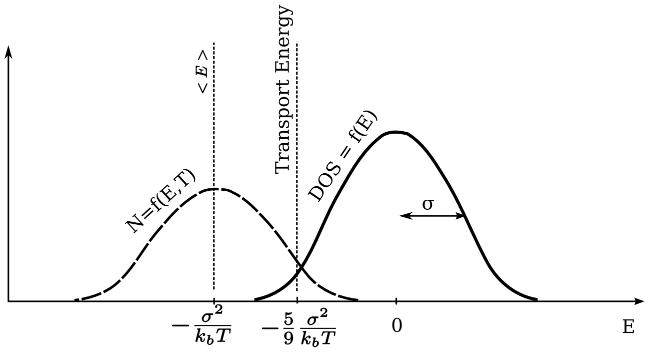

Figure 6.4: Bässler hopping model. DOS and the charge carrier density at equilibrium are of Gaussian shape. Conduction happens, when charges are excited from their immobile sites to an effective conduction energy with finite mobility. Here the charge carrier density is ploted in a much larger scale than the DOS.

6.4.1 Field dependence

Until now, spacial disorder did not play a role since it does not influence the equilibrium energy (6.16). This picture becomes different, when, the μ dependence on the electric field $\vec{E}$ is analysed.

Appling an electric field "tilts" the DOS, as the average potentials for uphill jumps is reduced as in (6.12). In order to reflect such a mobility increase, $\langle E_\infty \rangle$ must rise towards $E = 0$. Indeed Bässler observes nearly a Poole-Frenkel relation (Fig. 6.5) in his MC simulation without spatial disorder:

$$\ln(\mu) \propto \sqrt{|\vec{E}|}. \tag{6.20}$$

In a more realistic model with off-diagonal disorder, a more complicated $\vec{E}$ behaviour is seen. Spatial disorder can be introduced by variation of the

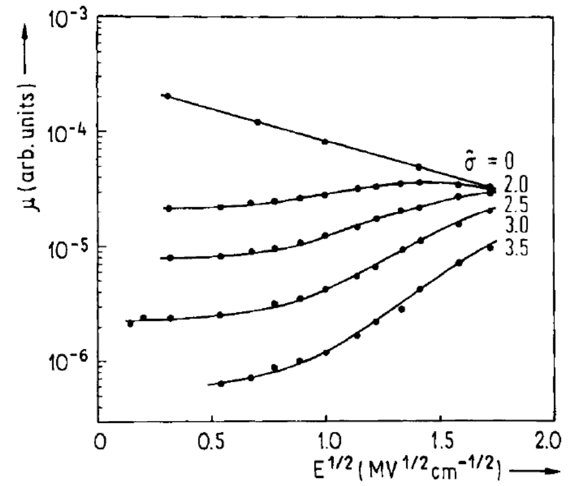

Figure 6.5: Simulated dependence of μ on the electric field E for different equilibrium energies $\hat{\sigma} = -\frac{\sigma^2}{k_b T}$. Calculated without considering spatial disorder of the sites. Figure is taken from Bässler.[4]

overlap integral between two sites. Individual molecule positions vary from a perfect crystal in position and angle. The overlap integral γ_0 (6.1) between two molecules strongly depends on the molecular coordinates. Therefore, γ_0 must be subject to some distribution as well. Instead of a constant γ_0, a Gaussian distribution Γ_{ij} characterized by the width Σ is used. The tunneling probability (6.1) now reads

$$\gamma_{ij} = \begin{cases} \Gamma_{ij} e^{-\frac{2R}{R_0}} e^{-\frac{E_j - E_i}{k_b T}} & \text{for } E_j > E_i, \\ \Gamma_{ij} e^{-\frac{2R}{R_0}} & \text{for } E_j \leq E_i, \end{cases} \tag{6.21}$$

where Γ_{ij} depends on the two sites i and j.

This off-diagonal disorder, can be easily included into the Monte Carlo simulation. The resulting mobility vs. $\vec{E}$ curves reveal strikingly different features (compare Fig. 6.5 to Fig. 6.6):

Mobilities experience negative slopes at low fields, when Σ reaches a critical value. This unexpected behaviour, where mobility decreases for a rising electric field can be explained in context of percolation a model. As shown in (Fig. 6.7) several conducting paths are considered between two sites with a larger distance from each other. While one direct route has higher barriers, another indirect path has a more favorable intersite coupling. Unfortunately it involves hopping against the electric field direction, and gives rise to a lowering in the mobility. With further increasing $|\vec{E}|$ this can be overcompensated and the change of mobility with $\vec{E}$ becomes positive. In the limit of high electric fields

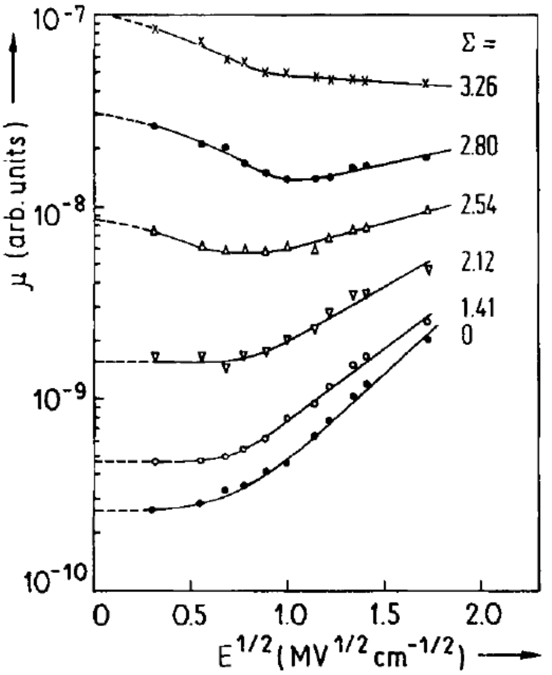

Figure 6.6: Simulated dependence of μ on the electric field E at different spatial disorders Σ and a fixed energetical disorder and temperature parameter $\hat{\sigma} = -\frac{\sigma^2}{k_bT} = 3$. Figure is courtesy of Bässler.[4]

($F > 1 \times 10^8$ V/m) this effect gives additional T and F dependent terms:

$$\mu(T) = \mu_0 e^{-\left(\frac{2\sigma}{3k_bT}\right)^2} \times \begin{cases} \exp\left[C\left(\left(\frac{\sigma}{k_bT}\right)^2 - \Sigma^2\right)\sqrt{|\vec{E}|}\right], & \text{if } \Sigma \geq 1.5 \\ \exp\left[C\left(\left(\frac{\sigma}{k_bT}\right)^2 - 2.5\right)\sqrt{|\vec{E}|}\right], & \text{if } \Sigma < 1.5 \end{cases} \tag{6.22}$$

with a constant C that depends on site spacing.

When energy distribution of neighboring trap sites is assumed to be correlated, mobility for lower fields can be found. This correlation means, that adjacent sites have lower energy difference than two sites at larger distance from each other. Correlation in trap energies may evolve from long-range charge dipole interactions in the material.[58] Bässlers model (or GDM) with this conditions is called correlated disordered model (CDM). The empirical mobility is now given by a similar expression proposed by Novikov and coworkers:

$$\mu(T) = \mu_0 e^{-\left(\frac{3\sigma}{5k_bT}\right)^2} \times \exp\left[C_0\left(\left(\frac{\sigma}{k_bT}\right)^{3/2} - \Gamma\right)\sqrt{\frac{eaF}{\sigma}}\right], \tag{6.23}$$

where $C_0 = 0.78$, a is the intersite separation and $\Gamma = 2$ for organic materials.[39]

CDM was used to fit temperature and field dependent mobility curves of PPV based LEDs, but it turned out not to be that usefull for FETs. A major

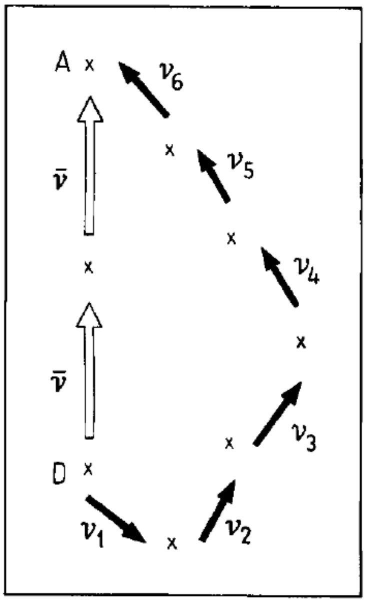

Figure 6.7: Schematic view of one direct and one indirect path, that a charge carrier can follow from the site D to A. The electric field $\vec{E}$ direction points from D to A. The jump rate ν_1 is hindered by the electric field. Figure is taken from Bässler.[4]

drawback of CDM and GDM models is that the resulting mobility is not gate bias dependent. In (6.16) it is even assumed, that the site density is much higher then the carrier density; therefore no charge-charge interaction occurs and the carriers act completely independent of each other. The model is successful in explaining the field dependence of mobility in organic LEDs, where the charge carrier density is much lower[58] ($n < 1 \times 10^{17}\,\mathrm{cm}^{-3}$) than in FETs where charges are injected by gate bias ($n \approx 2.5 \times 10^{21}\,\mathrm{cm}^{-3}$).[1] On the other hand, the electric field between source and drain in a FET is much lower, than the field in a LED between the anode and cathode (max. $E = 40\,\mathrm{kVcm}^{-1}$ in our case, compared to $E = 1\,\mathrm{MVcm}^{-1}$ in LEDs[4]). Electric fields dependence is therefore not as critical for FETs.

6.4.2 Carrier concentration dependence

In order to incorporate carrier- carrier interaction in a VRH, model Fermi-Dirac statistics must be used. Fishchuk et al. have developed such an analytical theory for hopping in a Gaussian DOS.[17] They use the effective medium approximation to calculate an affective jump rate for two cases: tunneling and polaron hopping between the sites. As in Bässler's model, an affective transport energy E_t is considered. In a hopping process, the carrier must be excited from his site energy E_1 to the transport energy E_t. The probability of a carrier to occupy a site with an energy E_1 is given by $P(E_1) = g(E_1)f(E_1, E_F)$ with a Gaussian

---

[1] Calculated for our FET geometry, when the accumulation layer is assumed to be 1 nm thick and $V_{GS} - V_0 = 20\,\mathrm{V}$

DOS $g(E)$ and the Fermi-Dirac statistics $f(E, E_F)$.

As a result, the authors find that for tunneling, at low charge carrier concentrations ($n/N < 1 \times 10^{-6}$) the mobility follows a sub Arrhenius relation $\ln(\mu) \propto 1/T^2$, but changes gradually to Arrhenius type $\ln(\mu) \propto 1/T$ as the concentration increases to $n/N > 1 \times 10^{-3}$ (Fig. 6.8). At fixed, low temperature, μ first increases with rising carrier concentration. Later, at very high concentration, when more than 10% of the sites are filled, the transport energy E_t comes into the upper region of the Gaussian with low DOS and μ decreases abruptly (Fig. 6.9). This would not be the case for an exponential DOS distribution. For polaron hopping, μ is independent of the carrier concentration, until the same saturation effect at 10% occupied states happens.

Effects of spatial disorder and the electric field dependence were not evaluated in this analytical model.

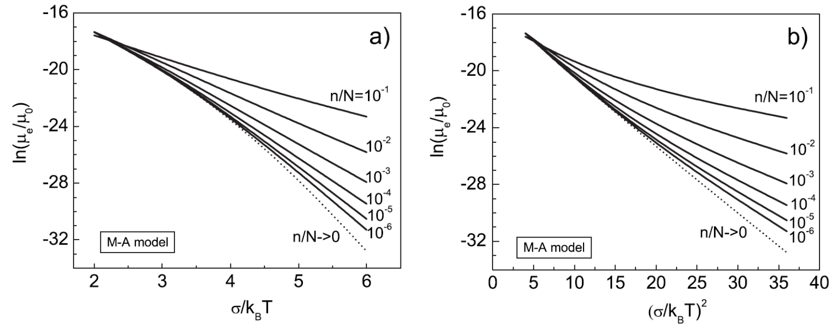

Figure 6.8: (a) Arrhenius plot of the effective mobility μ_e vs. T for different carrier concentrations. N is the total density of sites, σ is the width of the Gaussian DOS. (b) the same data plotted against $1/T^2$. Figure taken from Fishchuk et al.[17]

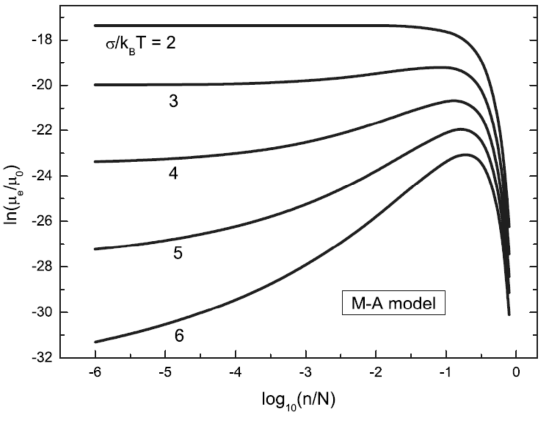

Figure 6.9: Dependence of effective mobility μ_e on charge carrier concentration at different temperatures. N is the total density of sites, σ is the width of the Gaussian DOS. Figure taken from Fishchuk et al.[17]

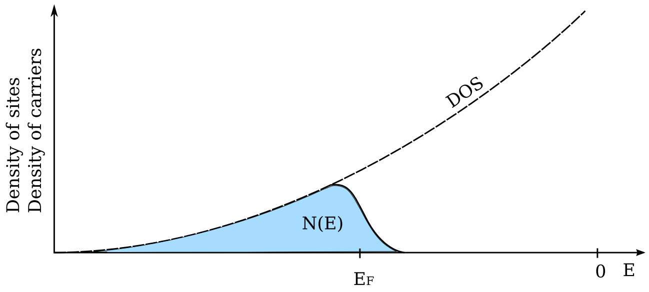

Figure 6.10: Exponential DOS and density of carriers vs. energy as used in the Vissenberg ans Matters percolation model.

6.5 Vissenberg and Matters hopping model

Vissenberg and Matter developed a model that is based on variable range hopping (VRH) in an exponential tail through a percolative resistor network. This section is based on their paper.[60]

The exponential site density is given by

$$N(E) = \frac{N_t}{k_b T_0} e^{\frac{E}{k_b T_0}} \quad (-\infty < E \leq 0) \tag{6.24}$$

with the total trap density per unit volume N_t and T_0 the characteristic temperature which is proportional to the width of the exponential tail. Injected charges will fill the lower-lying states deep in the exponential tail. Further added carriers will occupy higher states, where the DOS is higher, so they will find more suitable neighboring sites with low energy difference. The mobility will increase with higher gate bias in this fashion.

Fermi-Dirac statistics is used to calculate the relation of the Fermi energy E_F to the fraction of filled trap sites θN_t:

$$\theta \approx e^{\frac{E_F}{k_b T_0}} \Gamma\left(1 - \frac{T}{T_0}\right) \Gamma\left(1 + \frac{T}{T_0}\right) \tag{6.25}$$

Here, Γ is the gamma function. This approximation (6.25) is valid for $T < T_0$ and $E_F \ll -k_b T_0$. At higher temperatures and charge densities the assumption that all carriers are located in the exponential tail (Fig. 6.10) far below $E = 0$ no longer holds.

The conductance between two electrodes is described by a resistor network. The carriers hop from one site i to another site j with hopping probabilities that can be represented by resistances between i and j. The intersite conductances are given by a modified tunneling equation (6.1):

$$G_{ij} = G_0 e^{-s_{ij}} \tag{6.26}$$

where

$$s_{ij} = 2\alpha R_{ij} + \frac{|E_i - E_F| + |E_j - E_F| + |E_i - E_j|}{2 k_b T}. \tag{6.27}$$

Here $2\alpha R_{ij}$ is responsible for the tunneling process, with the intersite distace R_{ij} and the effective overlap parameter α. The second term includes the activation energy which is needed to overcome the energy difference between two sites, and also the occupation probabilities of the sites i and j. Note that the simple tunneling equation (6.1) as used in Mott's and Bässler's model does not take occupation probabilities into account.

In the next step, the overall conductivity is calculated using percolation theory.[3] More details can be found in the paper of the Vissenberg and Matters[60] The resulting mobility is given by

$$\mu_{FE} = \frac{\sigma_0}{e}\left(\frac{\pi(T_0/T)^3}{(2\alpha)^3 B_C \Gamma\left(1-\frac{T}{T_0}\right)\Gamma\left(1+\frac{T}{T_0}\right)}\right)^{T/T_0} \times\left(\frac{(C_i(V_G-V_0))^2}{2k_bT_0\epsilon_s}\right)^{(T/T_0)-1}, \tag{6.28}$$

where B_C is the critical number of bonds in a percolation system[2], ϵ_s is the dielectric constant of the semiconductor and σ_0 is an unknown prefactor.

The mobility follows the Arrhenius behaviour $\ln\mu \propto E_0/T$ with a weakly temperature dependent activation energy. There is also a power dependence in $(V_G - V_0)$ in the second term. The fitting parameters are σ_0, α and T_0. Their typical values are $\sigma_0 \approx 4\times10^{11}\,\mathrm{S/m}$, $k_bT_0 \approx 30\,\mathrm{meV}$ and $\alpha^{-1} \approx 0.1\,\mathrm{nm}$ (as given by Salleo at al.[49] for PQT-12).

The model is criticized by Salleo et al. for difficulties in assigning a physical meaning to σ_0. The prefactor represents the limit of conductivity at high temperatures, but the model does not apply for temperatures where $T > T_0$.[49] It is questionable that this percolation model can be applied to partly crystalline material such as P3HT, where spectroscopic data suggests charge delocalization over several molecules.[9] Tunneling would only occur in disorder regions between crystallites, and not between individual P3HT polymer chains inside a cristallite as assumed by the model.

---

[2] For three-dimesion amorphous system $B_C \approx 2.8$.

Chapter 7

Summary of charge transport models

Now its time to summarize the assumptions and predictions of the models discussed above. In all models, temperature and trap distributions play a major role but the electric field between the electrodes or the overall carrier density is missing in some descriptions.

In the mobility edge (ME) models the charge carriers are either localized in trap states or delocalized when excited to energies beyond the mobility edge energy. Contrary, in hopping models all charge carriers contribute to conduction through thermally activated hopping between immobile trap states. Those hopping models were analyzed by numerical simulations of individual charge carriers that were hopping in a cubic lattice with sites obeying some energy distribution. The results from these simulations were compared to analytical models, that are based on the assumption, that carriers in thermal equilibrium have an average energy $\langle E \rangle$ and must be excited to an effective transport energy E_t. So there are some similarities to the ME models, where carriers must also be excited to higher energies.

In the case of ME models, the traps are filled up with charge carriers and the Fermi energy comes closer to the mobility edge, as the gate bias is increased in FETs. So the energetic distance between mobility edge and carriers at Fermi energy decrease, and more charges are excited to delocalized states.

In hopping models conduction should be affected in the same way by the carrier concentration n, but since it was originally developed to describe LEDs with far lower n than in the accumulation layer in FETs, carrier-carrier interactions were dismissed. In the approximation of diluted n, the probability for occupation of states within the DOS of the traps depends only on the temperature. The average energy of carriers become temperature dependent $\langle E \rangle = f(T)$, with rising T (1) higher states are occupied and (2) thermal excitation to E_t becomes easier. Temperature is therefore involved in "two ways" and mobility shows a non-Arrhenius dependence $\ln(\mu) \propto 1/T^2$. Where in ME models gate bias decrease the activation energy E_a, temperature determines E_a in hopping models with diluted n.

Numerical simulations of individual charges at high carrier densities are not possible, but analytical approximations including Fermi-Dirac statistics showed that $\ln(\mu) \propto 1/T^2$ dependence changes to $\ln(\mu) \propto 1/T$ with rising n. Distinguishing between ME and hopping models, when only the temperature dependent mobility is given is therefore not easy.

In LEDs high electric field are applied between the electrodes. Usually mobilities show a Poole-Frenkel relation to the electric field: $\ln(\mu) \propto \sqrt{\vec{E}}$ as simulated in the hopping models. When spatial disorder is taken into account, simulations give a negative $\partial\mu/\partial\vec{E}$ -value for low $|\vec{E}|$ and the usual positive $\partial\mu/\partial\vec{E}$ -value at higher $|\vec{E}|$. To our knowledge $\vec{E}$ and its effect in combination with spatial disorder were not considered in ME models which are usually applied to FETs, where far lower $\vec{E}$ exists in the channel.

General ideas and predictions of models discussed above are shown in Fig. 7.1 and Fig. 7.2 respectively.

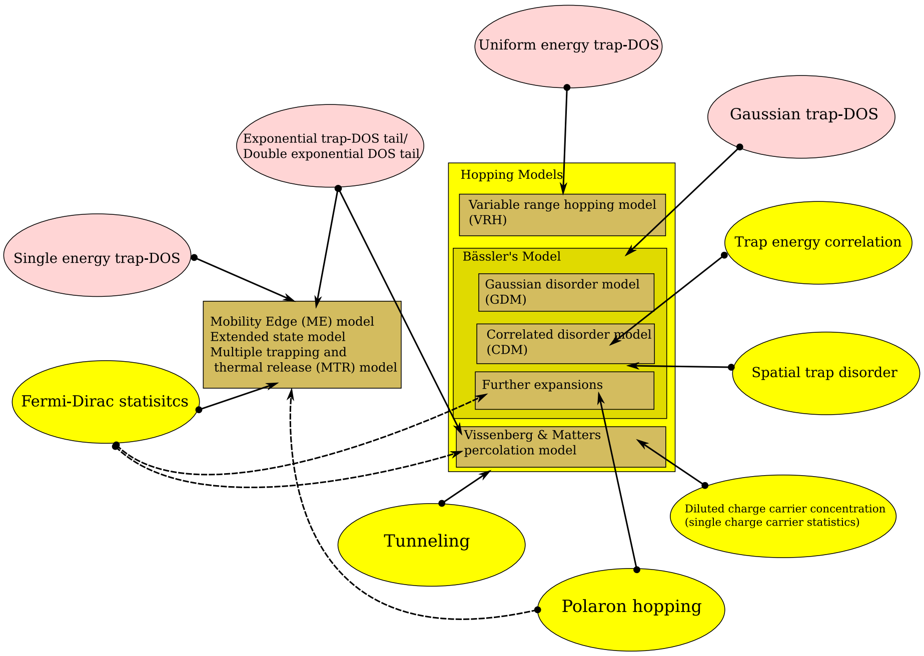

Figure 7.1: Concepts that are included in charge carrier transport models in disordered systems.

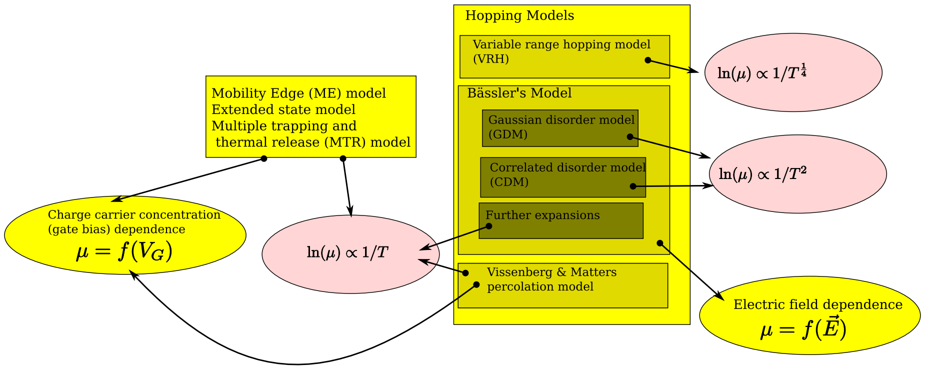

Figure 7.2: Predictions of different models for charge carrier transport in disordered systems.

Part III

Research on P3HT

Chapter 8

Morphology

In this chapter research results as found in the literature regarding chemical and crystal structure as well as morphology of poly(3-hexylthiophene) films are presented. All this properties do have an impact on the charge carrier transport and therefore on the performance of rr-P3HT based FETs as will be shown in the following sections. There is a vast number possibilities on how to prepare and to treat films from rr-P3HT and so the comparableness is limited. In every research group the preferred film casting method may differ and every group may have an emphasis on some different specific material properties. For this reasons it is difficult to draw definite conclusions from all the reports presented in this chapter.

8.1 Chemical structure

The chemical structure of one regioregular poly(3-hexylthiophene) (rr-P3HT) unit cell is given in Fig. 8.1. One unit cell consisting of two monomers contains two thiophene rings and two head to tail (HT) coupled hexyl side groups. The atomic weight of such a cell is 363.2 $^{g}/_{mol}$. This unit cells polymerize and form a conjugated backbone with good electrical conductivity.

Polythiophenes with molecular weight greater than 3 $^{kg}/_{mol}$ are not soluble in hot chloroform.[61] Alkyl side groups equal or greater than butyl ($-C_4H_9$) must be added to make it soluble in common organic solvents (chloroform, THF, xylene, toluene, methylene chloride, anisole, nitrobenzene, benzonitrile and nitropropane).[34] There are three possible orientations for the side groups of two adjoined thiophenes, head to tail (HT), head to head (HH) and tail to tail (TT) (Fig. 8.2). HH couplings cause a loss of conjugation because of a sterically driven twist of the two neighboring thiophenes, whereas repeated HT couplings promote planar conjugated structure of the π-system. This is shown by ab initio gas phase calculations.[35] Long conjugation lengths lead to good conductivity along the backbone. The percentage of HT couplings in a polymer chain is called *head to tail regioregularity*, or sometimes just *regioregularity*. The degree of regioregularity can be determined by NMR measurements.[34]

Spectroscopic analysis in the UV-vis region typically reveals a $\lambda_{max} = 442 - 456\,\text{nm}$ for the $\pi - \pi^*$ transition, and a band edge energy ranging from 1.7 to 1.8 eV.

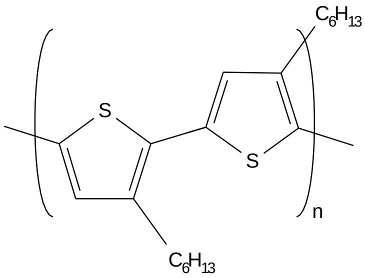

Figure 8.1: Chemical structure of one Poly(3-hexylthiophene) (P3HT) unit.

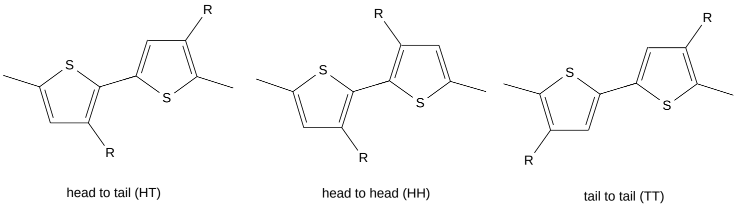

Figure 8.2: Possible regiochemical side group couplings for Poly(3-alkylthiophene) (PAT).

8.2 Crystal Structure and Crystal Alignment

The crystal structure of P3HT can be acquired by X-Ray and electron diffraction methods. The unit cell of a P3HT crystal is orthorhombic and has lattice of constants 0.39 nm, 0.836 nm and 1.66 nm (Fig. 8.3), as deduced from selected-area electron diffraction (SAED) patterns on single crystals wires.[13]

Surprisingly, polythiophenes with long insulating side groups such as dodecyl ($C_{12}H_{25}$) in regioregular coupling exhibit conductivities up to twice those for unsubstituted polythiophenes. This is attributed to enhanced self organizing of the polymer chains upon film formation. From powder X-Ray measurements on poly(3-octylthiophene) and poly(3-dodecylthiophene) interdigitated alkyl side chains are proposed.[44]

P3HT performance strongly depends on the orientation of the backbone with respect to the substrate SiO_2 plane (Fig. 8.4). The orientation is affected by the regioregularity and surface modifications. Treating the surface with hexamethydisilazane (HDMS) in order to make it hydrophobic is quite popular. HDMS replaces the natural hydroxyl group termination of SiO_2 substrates with apolar methyl groups. It is believed, that they attract the hexyl side groups and promote the edge on position of the backbone with respect to the substrate plane. HDMS treated substrates were found to increase the mobility by a factor of 2-10 to untreated hydrophilic SiO_2 substrates.[54]

On the other hand, in devices annealed above the melting point ($T_M \approx 216\,°C$) of P3HT ($M_W = 54\,\mathrm{kg/mol}$) the backbone adopted face on orientation, where thiophene rings lie flat (parallel to octyltrichlorsilane (OTS) treated substrate).[30]

A similar discrepancy is reported by Ho at al.[42] They studied air and surface interfaces of rr-P3HT films deposited on hydrophobized SiO_2 from different solutions with near-edge X-ray absorption fine-structure spectroscopy (NEXAFS). Considerably more disorder was found on the surface than in the bulk and a significant fraction of in-plane (face on) stacking of the P3HT backbones for low boiling temperature solvents (chloroform, chlorobenzene, toluene,p-xylene) was observed. The morphology at the interfaces is of critical importance, since the accumulation layer is formed in the polymer in the vicinity of SiO_2 and so the major part of charge transport happens there.

P3HT has good conductivity along the $\pi - \pi$ stacking direction [b axis, (010) diffraction] promoted by short inter-chain distances (0.39 nm) and good $\pi - \pi$ overlap. For FETs, the current flows from source to drain, that is parallel to the surface; therefore, it is preferred to have the b axis parallel to the surface (Fig. 8.4). Lamellar packing along the hexyl side chains gives diffraction peaks along the *a* axis [(100) diffraction]. The *a* axis should be perpendicular to the surface for good conductivity, since charge transport is impeded by the insulating alkyl chains.[8]

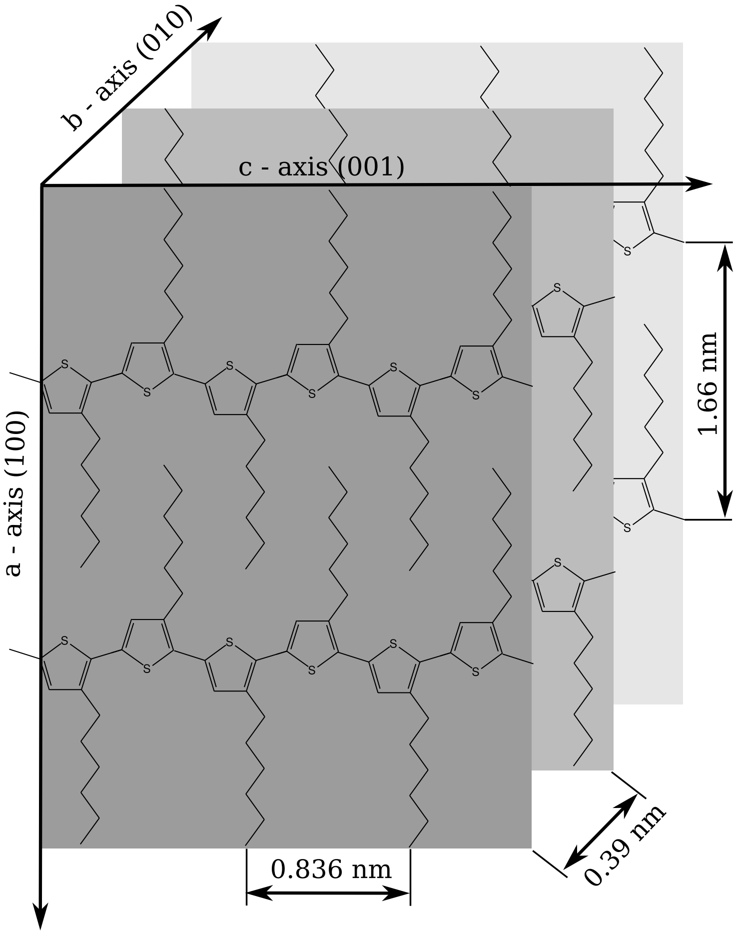

Figure 8.3: Crystal structure of a P3HT single crystal has a orthorhombic unit cell with diffraction peaks corresponding to lattice constants at 0.39 nm, 0.836 nm and 1.66 nm.[13]

8.3 Mesoscale

P3HT crystallize in nanoribbons which can be embedded in an amorphous phase, or overlap and develop boundaries where charge carrier can hop from one nanoribbon to another. The morphology depends on solvent used, polymer molecular weight and deposition technique. In this section the impact of these parameters is discussed.

The mesoscale structure of P3HT films grown on substrates depends critically on molecular weight, regioregularity and solvent evaporation rate (that is on the time it takes the wet film to solidify after deposition). The polymers can

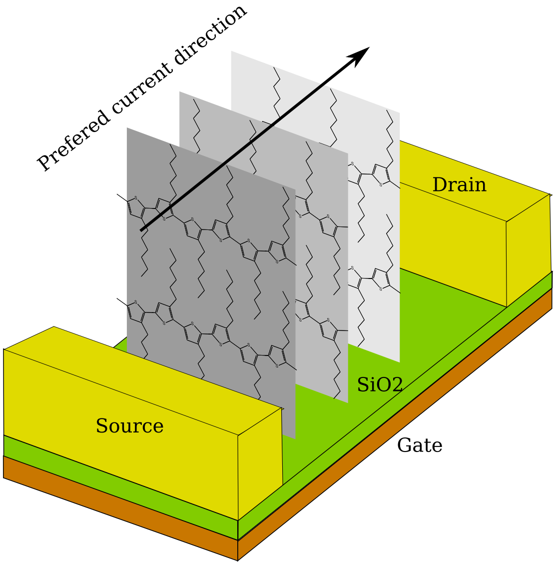

Figure 8.4: P3HT crystals have the best conductivity along the b axis which correspods to the (010) diffraction peak. In this sketch, the alignment for the best conductivity is shown, where the plane of the molecular backbone is perpendicular to the substrate plane (edge-on structure).

be roughly divided into two classes: low molecular weight $M_w < 15 - 20\,{}^{\mathrm{kg}}\!/\!_{\mathrm{mol}}$ and high molecular weight $M_w > 15 - 20\,{}^{\mathrm{kg}}\!/\!_{\mathrm{mol}}$. High $\mathrm{M_W}$ polymer films' charge carrier mobilities benefit from slow solvent evaporation after being drop or spin cast.[9]

Kim et al. succeeded in growing 1D single-crystal P3HT microwires on silicon substrate covered with octadecytrichlorsilane self-assembled monolayers (SAM). After drop casting, the substrate was covered with a jar to prevent fast evaporation through increased solvent vapor pressure. As a result, straight microwires lying flat on the substrate with rectangular cross section and typical heights of $0.7 - 1.3\,\mu\mathrm{m}$, widths of $1 - 3\,\mu\mathrm{m}$ and length of $30 - 500\,\mu\mathrm{m}$ crystallized. The wire axis corresponds to the b-axis, which is a good thing. Electrical characterisation of one such microwire after evaporation of gold contacts on top of it showed high currents $10 \times 10^{-6} - 20 \times 10^{-5}\,\mathrm{A}$ at $V_{DS} = 1\,\mathrm{V}$ and V_{GS} ranging from -1.5 V to 1.5 V.[13]

Chang et al.[8] compared low and high M_W P3HT films deposited from high and low boiling point solvents 1,2,4-trichlorobenzene (TCB) $T_B = 214.4\,^{\circ}\mathrm{C}$ and chloroform $T_B = 61.2\,^{\circ}\mathrm{C}$. Spin cast films from chloroform solution dry rapidly in a few seconds, while films made from TCB need approximately 10 minutes to dry up after the rotation stops. Charge carrier mobility in high M_W P3HT films critically depends on this solvent evaporation time. Transistors made on hexamethyldisilazane (HDMS) treated $\mathrm{SiO_2}$ substrates with $M_W = 270\,{}^{\mathrm{kg}}\!/\!_{\mathrm{mol}}$ P3HT had high mobilities $\mu = 1 \times 10^{-1}\,{}^{\mathrm{cm}^1}\!/\!_{\mathrm{Vs}}$ when TCB was used and lower mobilities $\mu = 1 \times 10^{-2}\,{}^{\mathrm{cm}^2}\!/\!_{\mathrm{Vs}}$ using chloroform as a solvent. Devices made by drop casting did not show this dependency on the solvent, because even in the case of chloroform it takes longer time for the larger volume of solvent to evaporate.

For low $\mathrm{M_W}$ polymers there is no clear dependence on film formation speed. Mobilities for spin and drop-cast chloroform samples of $\mu = 1 \times 10^{-2}\,\mathrm{cm^2/Vs}$ were better than for TCB spin cast samples ($\mu = 1 \times 10^{-3}\,\mathrm{cm^2/Vs}$). This indicates that low $\mathrm{M_W}$ polymer chains had enough time to self assembly in cristallites in all cases, but were affected by the solvent chemistry.

From grazing incidence X-ray diffraction measurements the backbone alignment in relative to the substrate was obtained. All chloroform spin cast films showed (100) and (010) peaks (mixed edge on, face on position), while all TCB spin cast films showed only (010) peaks in the in plane direction (edge on position). It is assumed that the edge on position leads to higher mobilities (Fig. 8.4). The alignment only depended on the solvent but not on the $\mathrm{M_W}$.
Dependence on the $\mathrm{M_W}$ was found in the shape (not in the position) of the diffraction peaks and in the AFM pictures. Low $\mathrm{M_W}$ polymers had higher diffraction peaks and therefore a higher degree of crystallinity. On the other side, shorter nanoribbons were revealed by tapping-mode atomic force microscopy for the same low $\mathrm{M_W}$ polymers. This means, that a drain-source current has to cross more boundaries. High crystallinity should result in higher mobility, but the increased number of grain boundaries between the nanoribbons could countervail the improvement.

From optical absorption and emission measurements the bandwith of neutral excitons could be estimated. It was shown that conjugation length increases when the exciton bandwith decreases. Charge carrier delocalization over the backbone of the polymer is directly connected to the conjugation length; higher conjugation improves the conductivity within the polymer chains. The conjugation length could be qualitatively estimated for different solvents and $\mathrm{M_W}$s. In films spin cast from chloroform the conjugation length decreases with rising $\mathrm{M_W}$. This was explained by the shorter time lower $\mathrm{M_W}$ polymer chains need to arrange to form a crystal. In TCB spin cast films the dependence was more complicated. The shortest conjugation length was measured for $M_W = 15.4\,\mathrm{kg/mol}$, the longest conjugation length for $M_W = 29\,\mathrm{kg/mol}$. An intermidiate conjugation length was observed for $M_W = 270\,\mathrm{kg/mol}$. This was explained by the larger number of chain ends, where chemical impurities can occur for low $\mathrm{M_W}$ on the one side and higher conformational disorder for high $\mathrm{M_W}$ on the other side.

Further analysis by Chang et al.[9] showed charge-transfer (CT) bands in the midinfrared in the charge modulation spectra. Those bands were associated with interchain delocalization of the polaron wave function. Chang's results suggest, that polarons in high $\mathrm{M_W}$ P3HT spin cast from TCB are delocalized over several polymer chains. In contrast low $\mathrm{M_W}$ P3HT spin cast from TCB and all P3HT spin cast from chloroform exhibited localized behavior with activation energies $E_a = 30\,\mathrm{meV}$ and $E_a \approx 4\,\mathrm{meV}$ respectively. Those activation energies account for interchain hopping of the polarons in a single P3HT crystal, but not for structural defects like grain boundaries.

Another reason why high $\mathrm{M_W}$ yielded better mobilities may be that individual high $\mathrm{M_W}$ polymer chains interconnected domains of ordered backbones more effectively, avoiding high potential barriers at the domain boundaries.[8] This idea is supported by the high discrepancy of the average areas of "X-Ray domains" and "conducting domains". Reitzel et al.[46] did grazing incidence X-ray diffraction (GIXD) measurements on amphiphilic polythiophene ($M_W = 24.6\,\mathrm{kg/mol}$, 95 % regioregularity) Langmuir films on water surface (Fig. 8.6). The align-

Table 8.1: Observed trends for different molecular weight P3HT polymers spin cast from chloroform and 1,2,4-trichlorbenzene solution on hexamethyldisilazane treated 200 nm SiO_2 substrate with highly doped Si as common gate. Mobilities were extracted at room temperature in the saturation regime with $V_{DS} = -50\,\mathrm{V}$ by fitting the square root of I_D using equaion (4.13). Diffraction peaks were measured in the plane of the substrate. The topography and the lengths of the nanoribbons were deduced from tapping mode AFM images of P3HT films on bare SiO_2. The conjugation length were calculated from UV-vis emission and absorption spectra. Polaron states were obtained from charge modulation spectra in midinfrared. Activation energies E_a for interchain hopping were given for localized polarons. Overall FET activation energies E_a^{μ} were extracted from temperature dependent mobilities fitted to $\mu \sim \exp(-E_a^{\mu}/kT)$ in the temperature range 100 - 300 K. All data is taken from publications of Chang et al.[8, 9]

	low M_W $CHCl_3$	intermediate M_W $CHCl_3$	high M_W $CHCl_3$	low M_W TCB	intermediate M_W TCB	high M_W TCB
mobility $\mu/\frac{cm^2}{Vs}$	1×10^{-2}	9×10^{-3}	2×10^{-3}	1×10^{-3}	6×10^{-2}	1×10^{-1}
X-ray in plane reflections	(100), (010)	(100), (010)	(100), (010)	(010)	(010)	(010)
topography	granular	granular	granular	nanoribbons	nanoribbons	nanoribbons
nanoribbon lengths / nm	-	-	-	24	-	282
conjugation length	high	intermediate	low	low	high	intermediate
polaron	-	localized	-	localized	delocalized	delocalized
polaron E_a/meV	-	4	-	30	0	0
E_a^{μ}/meV	-	85	-	110	50	45

ment and the 2D crystal structure of the Langmuir films closely resembled the bulk structure (Fig. 8.5). They estimated the coherence length of the scattering domains to be $L \approx 5\,\mathrm{nm}$. This was calculated from the width of the $\pi-$stacking distance reflection. Hassenkam et al.[21] exploited the same polymer film, after transferring it onto a SiO_2 substrate. This monolayer was than doped with $AuCl_3$ prior to measuring the surface potential with the electrostatic force microscopy (EFM) method. From the resulting profiles (Fig. 8.7) the average dimesions of conducting domains were estimated (200 - 800 nm). Those domains were about 100 times larger than those measured by Reitzel et al. Thus it has been proposed that “conducting domains” consist of several smaller “X-Ray domains” which are connected by stuck out polymer chains. This fits into the above picture, where mobility of high M_W polymers was good, in spite of reduced crystallinity.

Studies for low M_W in the range of 2.4 - 18.4 kg/mol by Zhang et al.[64] demonstrate that the width of the nanofibrils corresponds to the weight average contour length of the polymer chains. The nanofibril width was determined from Fourier analysis of taping mode atomic force micrographs (TMAFM) W_{AFM} and from grazing incidence X-ray diffraction (GIXRD) W_{GIXRD}. The polymers were deposited by drop casting from 1 g/l toluene solution onto SiO_2 substrates. The authors found a linear dependence of W_{AFM} and W_{GIXRD} on M_W for $M_W < 10$ kg/mol (Fig. 8.8). Assuming that the nanofibrils were composed by one-molecular-wide stacked sheets with the b-axis parallel to the fibril axis, the nanofibrils width W can be calculated by

$$W = b \times \frac{M_W}{M_{unit\ cell}}, \qquad (8.1)$$

where $b = 0.836\,\mathrm{nm}$ is the lattice vector for two thiophene rings along the conjugated chain and $M_{unit\ cell} = 363.2$ g/mol is the molecular weight of the two thiophene rings including the sidegroups. Indeed this roughly holds up to $M_W < 10$ kg/mol. The charge carrier mobility extracted from the FET character-

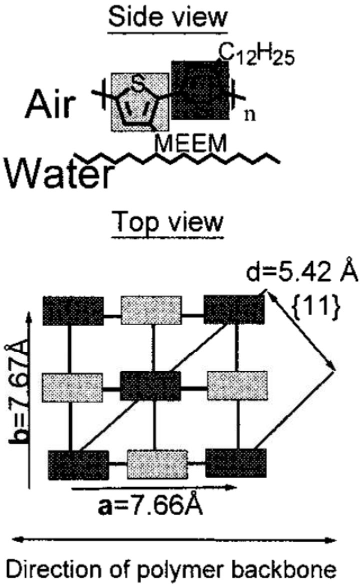

Figure 8.5: 2D structure of a Langmuir polythiophene film as obtained by synchrotron GIXD. This figure is taken from Reitzel et al.[46]

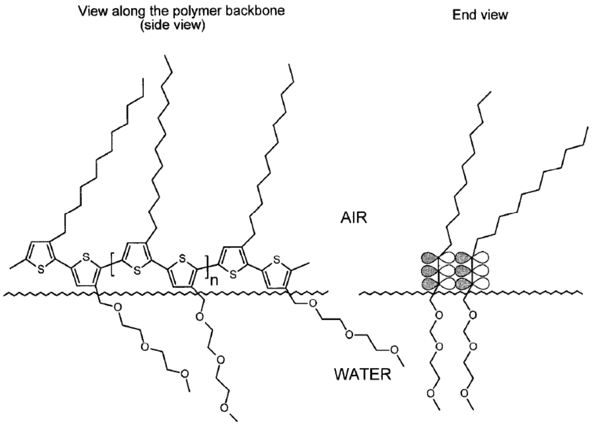

Figure 8.6: (Left) regioregular amphiphilic polythiophene at the air-water interface. (Right) end view of two adjacent π-stacking polymer chains. Figure taken from Reitzel et al.[46]

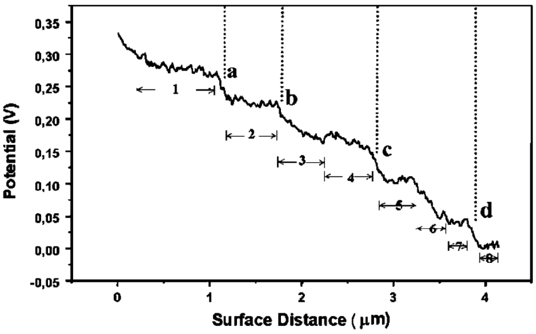

Figure 8.7: Potential profile along the current flow direction of a doped polythiophene (Fig. 8.6) monolayer film. The step-like features are attributed to domain boundaries, the slopes in-between to domains of various conductivity. Figure taken from Hassenkam et al.[21]

istics showed exponential dependence $\mu_f = \mu_0 \exp(W_{AFM}/W_0)$. As Hutchinson et al.[27] pointed out, this could result from geometrical reorganisation energies of the individual polymer chains, which are less constrained at lower $\mathrm{M_W}$. Therefore, low $\mathrm{M_W}$ polymer would have a higher E_a for inter-chain polaron hopping within a fibre giving rise to lower mobilities.

Mobility for low and high molecular weight ($M_N = 3.2 \cdots 36\,{}^{\mathrm{kg}}\!/\!_{\mathrm{mol}}$) rr-P3HT increased ($1.7\times10^{-6} \cdots 9.4\times10^{-3}\,{}^{\mathrm{cm}^2}\!/\!_{\mathrm{Vs}}$) with rising $\mathrm{M_W}$ as was shown by Kline et al.[45] They measured FET mobility of spin cast rr-P3HT from 0.5 wt.-% chloroform solution HDMS treated $\mathrm{SiO_2}$. These findings also match the reports above; the mobility increases until $M_W \approx 20\,{}^{\mathrm{kg}}\!/\!_{\mathrm{mol}}$ and than flattens of at around $6\times10^{-3}\,{}^{\mathrm{Vs}}\!/\!_{\mathrm{cm}^2}$ (Fig. 8.9) as a consequence of short solvent removal times. The mobilities would probably have risen further, if a high boiling temperature solvent was beeing used as described in the publications of Chang et al.[8, 9]

No dependency on the end groups of the polymer chains was found by Kline et al.[45] The authors tested samples with bromine and methylthiophene end groups. Polythiophene with bromine end groups were strong electron acceptors, but did not differ from those with methylthiophene end groups in terms of mobility. The impact of polydispersivity was also analyzed. No significat difference in electric properties was found between polymers with $PDI = 1.3 - 1.9$ and those synthesized by another route resulting in $PDI = 1.1 - 1.5$. The main mobility determining factor seemed to be the molecular weight.[45]

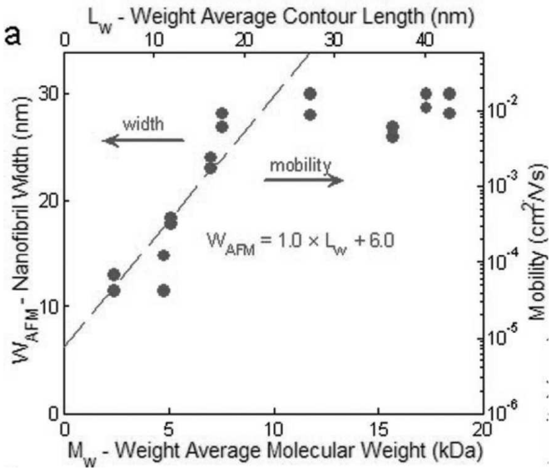

Figure 8.8: Dependence of nanofibril length and charge carrier mobility on weight average molecular weight M_W and weight average contour length L_W of rr-P3HT. Figure taken from Zhang et al.[64]

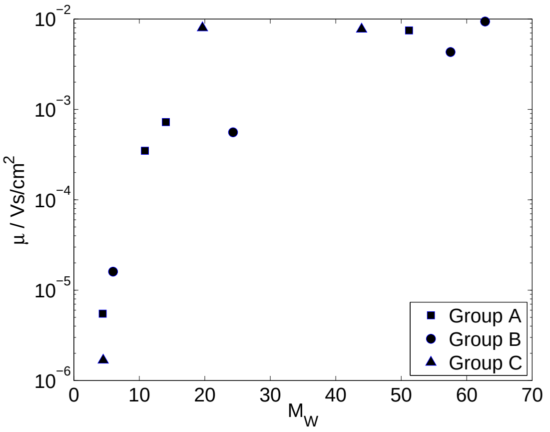

Figure 8.9: Field effect mobility of different molecular weights M_W rr-P3HT polymers. The groups refer to different polymer synthesis routes. Note that the figure is scaled to M_W rather than M_N in order to stay consistent throughout this thesis. Data taken from Kline et al.[45]

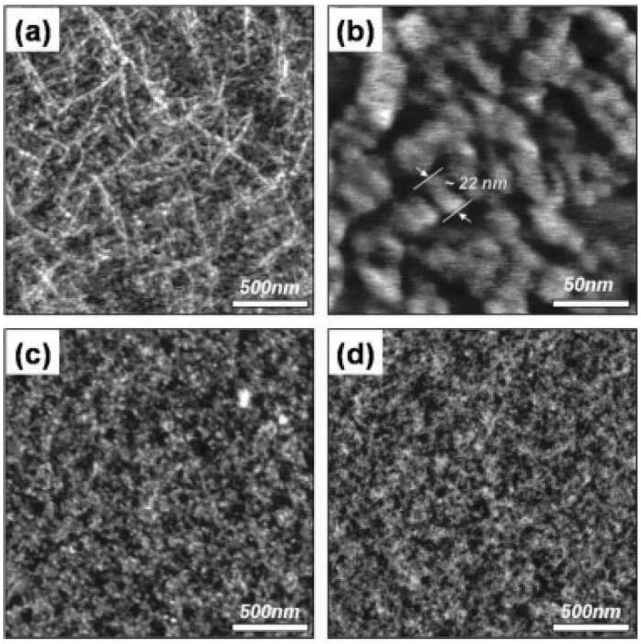

Figure 8.10: Tapping mode AFM. rr-P3HT **spin cast** on **bare** SiO_2 substrates from 7 g/l $\mathbf{CHCl_3}$ solution with different M_W; (a) 4.9 kg/mol, (b) 4.9 kg/mol high magnification, (c) 33.6 kg/mol and (d) 77.4 kg/mol. Figure taken from Yang et al.[23]

8.4 Survey on AFM images of P3HT films

AFM images for various P3HT films cast from $CHCl_3$, TCB and toluene at different concentrations and with M_W ranging from 2.4 - 270 kg/mol have been published.[9, 11, 23, 31, 45, 62, 64] As seen in the images below, there is a transition from fibrilar to nodular structure. This transition depends on M_W and solvent removal time. For fast evaporating solvents and spin coating, the transition lies at $M_W(transition) \approx 5$ g/l (Fig. 8.10 and Fig. 8.11), for slow evaporating solvents as TCB it lies significantly higher $M_W(transition) > 270$ kg/mol (Fig. 8.12 and Fig. 8.13). For low M_W at $M_W \approx 4.4$ g/l the structure is more distinct at longer solvent removal time; the nanofibrills length increases and the nanofibrills agglomerate into bundles (Fig. 8.14). In-between the extremes it is not clear, whether a new structure arises, or if the images are obscured by intersecting flexible nanorods at higher P3HT concentrations in the solvent (Fig. 8.15 and Fig. 8.16). Another structural transition is shown in Fig. 8.17. Here nanofibrils become granular upon annealing at 170 °C.

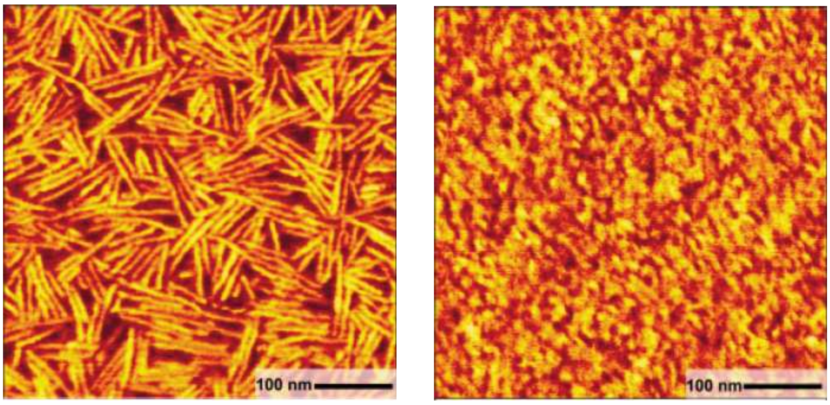

Figure 8.11: Tapping mode AFM (phase image). rr-P3HT **spin cast** on **HMDS treated** SiO_2 substrate from $7\,{}^{g}/_{l}$ $\mathbf{CHCl_3}$ solution for different M_W; (left) $4.4\,{}^{kg}/_{mol}$ and (right) $43.4\,{}^{kg}/_{mol}$. Figure taken from Kline et al.[45]

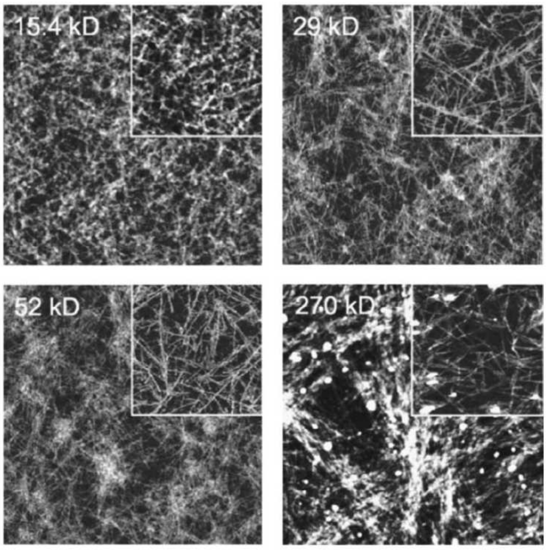

Figure 8.12: Tapping mode AFM. Image size: $5\,\mu m \times 5\,\mu m$. rr-P3HT **spin cast** on **bare** SiO_2 substrate from dilute $\mathbf{1\,{}^{g}/_{l}}$ **TCB** solution. Nanoribbon lengths are increasing between $15.4\,{}^{kg}/_{mol}$ and $29\,{}^{kg}/_{mol}$. Estimated widths of nanoribbons are 15 nm for the lowest and 20 nm for the highest M_W. Figure taken from Chang et al.[9]

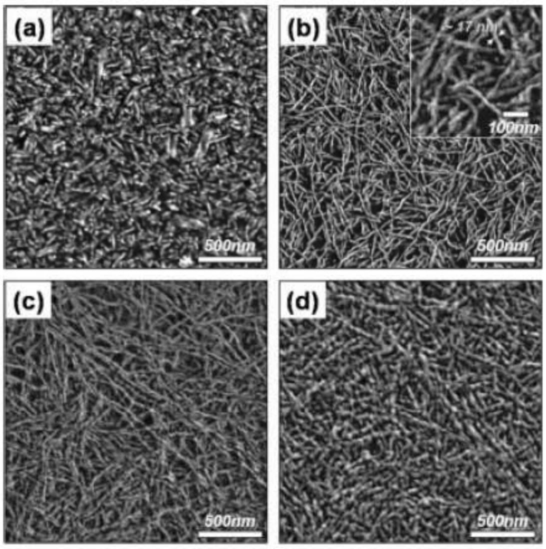

Figure 8.13: Tapping mode AFM. rr-P3HT **drop cast** on **bare** SiO_2 substrate from 1.5 g/l **$CHCl_3$** solution with different M_W; (a) 2 kg/mol, (b) 4.9 kg/mol, (c) 33.6 kg/mol and (d) 77.4 kg/mol. Figure taken from Yang et al.[23]

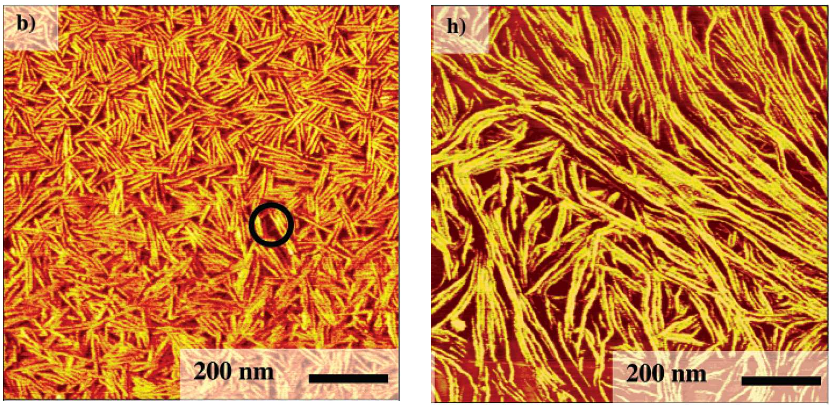

Figure 8.14: Tapping mode AFM (phase image). rr-P3HT (4.4 kg/mol) on **HMDS treated** SiO_2 substrate for different deposition methods; (left) **spin cast** from 2-5 g/l $CHCl_3$ solution, (right) **drop cast** from 0.5 g/l **$CHCl_3$** solution. Figure taken from Kline et al.[31]

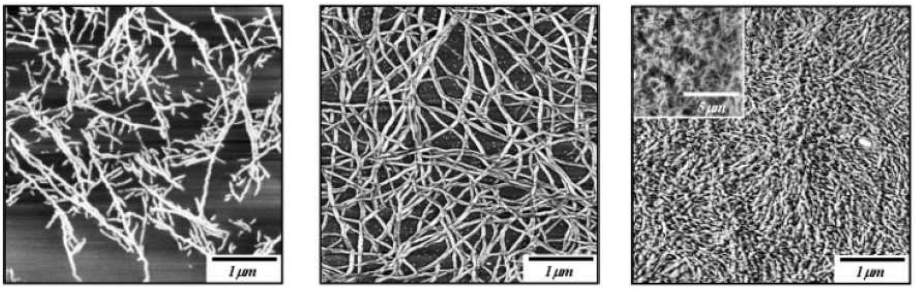

Figure 8.15: Tapping mode AFM. rr-P3HT ($M_W = 25\,{}^{\mathrm{kg}}/_{\mathrm{mol}}$, $PDI = 2.2$) **drop cast** on **bare** SiO_2 substrate from diluted $\mathbf{CHCl_3}$ solution; (left) $0.7\,{}^{\mathrm{g}}/_{\mathrm{l}}$, (center) $1.5\,{}^{\mathrm{g}}/_{\mathrm{l}}$ and (right) $4\,{}^{\mathrm{g}}/_{\mathrm{l}}$. Figure is taken from Yang et al.[62]

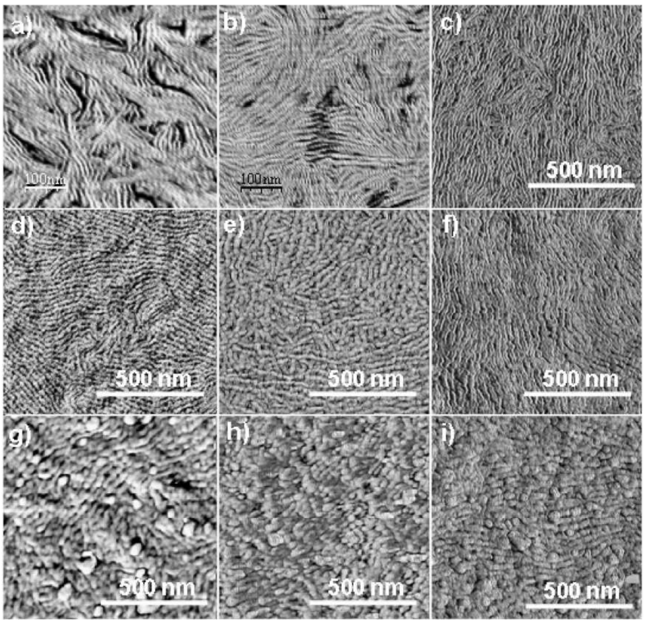

Figure 8.16: Tapping mode AFM. rr-P3HT **drop cast** from $1\,{}^{\mathrm{g}}/_{\mathrm{l}}$ **toluene** solution onto **bare** SiO_2 substrate with different M_W; (a - i) were respectively equal to: 2.4, 4.8, 7.0, 7.5, 11.8, 15.7, 17.3 and $18.4\,{}^{\mathrm{kg}}/_{\mathrm{mol}}$. Figure is taken from Zhang et al.[64]

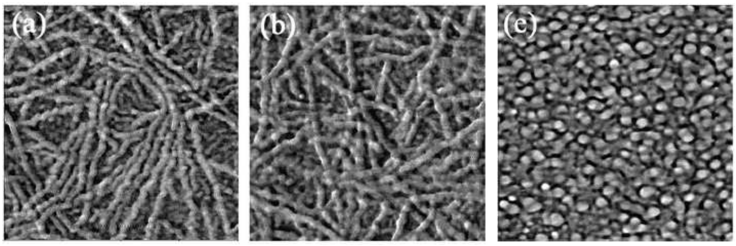

Figure 8.17: Tapping mode AFM (phase images). Image size: 800 nm × 800 nm. rr-P3HT with 39.5 kg/mol **dip coated** at 1 mm/min from 1 g/l **$CHCl_3$** solution onto **HMDS** treated SiO_2 substrate; (a) as prepared, (b) annealed at 150 °C and (e) annealed at 170 °C. Figure is taken from Cho et al.[11]

8.5 Post annealing effects

In this section the effects of post annealing on the performance of the devices are discussed. *Post annealing* stands for annealing as the last step of device fabrication.

It was shown by Cho et al.,[11] that field effect mobilities of rr-P3HT can be increased by post annealing. The authors fabricated FETs by dip coating of HMDS treated SiO_2 substrate in a rr-P3HT ($M_W = 39.5\,\mathrm{kg/mol}$) $1\,\mathrm{l/kg}$ $CHCl_3$ solution. The device was than heated to 150 °C for a duration of 10 min in inert atmosphere. The measured mobilities were roughly two times higher than in untreated devices. This was attributed as increase of the thickness of the fibrils from 20 - 35 nm to 30 - 40 nm as was seen in tapping mode AFM pictures. Above 150 °C a phase transition from fibrillar to granular cristallites occured. The granular phase showed low mobilities, therefore higher temperatures than 150 °C should be avoided.

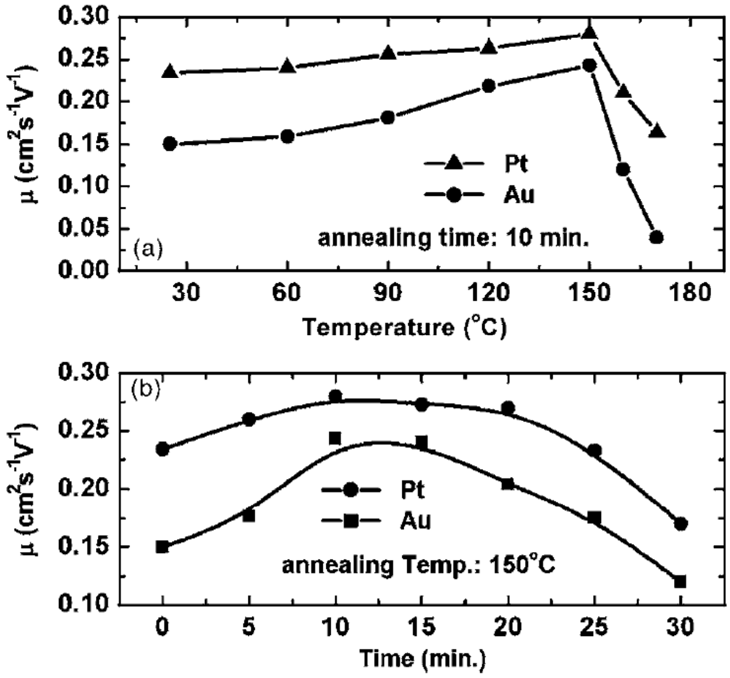

Figure 8.18: (a) FET mobility vs. annealing temperature. (b) FET mobility vs. annealing time at 150 °C. Both for rr-P3HT ($M_W = 39.5\,\mathrm{kg/mol}$), dip coated onto HMDS treated SiO_2 from $1\,\mathrm{l/kg}$ $CHCl_3$ solution. Au and Pt bottom contact electrodes were used. Figure taken from Cho et al.[11]

In another study, Kline et al.[31] showed that annealing of very low molecular weight $M_W \approx 3\,\mathrm{kg/mol}$ rr-P3HT, spin cast onto HDMS treated SiO_2 yield mobility enhancemend by a factor of 1000 from $2 \times 10^{-6}\,\mathrm{Vs/cm^2}$ to $2 \times 10^{-3}\,\mathrm{Vs/cm^2}$ (samples were heated to 125 °C for 1 h in inert atmosphere). Annealing of higher M_W polymers $M_W \geq 10\,\mathrm{kg/mol}$ had no effect. AFM images show that the length of the nanorods increase upon heat treatment for very low M_W P3HT. This results in better connected neighbors and additionally in a reduced number of

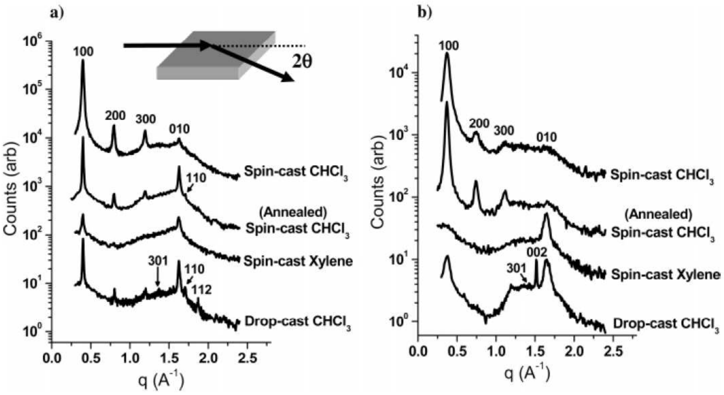

Figure 8.19: In-plane grazing incidence XRD data for P3HT films on HMDS treated SiO_2; (a) $M_W \approx 3\,{}^{\mathrm{kg}}/_{\mathrm{mol}}$; (b) $M_W \approx 30\,{}^{\mathrm{kg}}/_{\mathrm{mol}}$. Annealing was done at 150 °C for 1 h in inert atmosphere. Figure taken from Kline et al.[31]

required inter-rod hops to traverse the film. Thus superior mobility is achieved in post annealed film, than in the untreated film with short randomly oriented nanofibrils. In contrast, little difference in higher M_W films is observed from AFM measurements. They all feature a nodulelike structure. Alignment relative to the substrate differs significantly for very low and high M_W as measured with GIXD. After annealing, in plane (010) diffraction peak arouse for very low M_W but not for higher M_W. It seems that annealing at 150 °C facilitate edge on orientation for very low M_W and face on orientation for higher M_W (Fig. 8.19). Note that edge on orientation favors in plane mobility and therefore results in better performing FETs (p.8.2).

Zen et al.[1] report an increase of the FET mobility for $M_W = 3.1, 6.6, 25\,{}^{\mathrm{kg}}/_{\mathrm{mol}}$ by a factor of two, but interestingly decreased mobility for $M_W = 20\,{}^{\mathrm{kg}}/_{\mathrm{mol}}$ after post annealing. Their transistors were prepared by spin coating from $CHCl_3$ onto HDMS treated SiO_2. Annealing was performed at 150 °C for 5 min in inert atmosphere.

Yang et al.[23] investigated the effects of annealing at higher temperatures than Kline et al.[31] They examined the film morphology by AFM and GIXD. They prepared rr-P3HT ($M_W = 33.6{}^{\mathrm{kg}}/_{\mathrm{mol}}$, $PDI = 1.79$, 96 % regioregularity) films spin cast from 0.1 - 0.5 wt % $CHCl_3$ solution onto piranha cleaned SiO_2 substrates. After deposition, the substrates were examined as prepared, after annealing at 200 °C for 12 h and after melt crystallizing at 240 °C (Fig. 8.20). They were than compared to drop cast films. In agreement with previously mentioned publications, perpendicular to the plane (010) diffraction is observed for rapidly forming spin cast films. This perpendicular to the plane (z-direction) (010) diffraction originated from face on alignment of the backbone relative to the substrate.
Annealing of the spin cast film facilitated crystallinity, gave rise to higher order (100) and mixed edge on / face on (010) peaks. In other words, both edge-on and face-on alignment relative to the substrate was found after annealing. Ultimately diffraction patterns from melt crystallized P3HT showed more pronounced higher order (100) peaks in the z-direction and blurred (010) peaks in

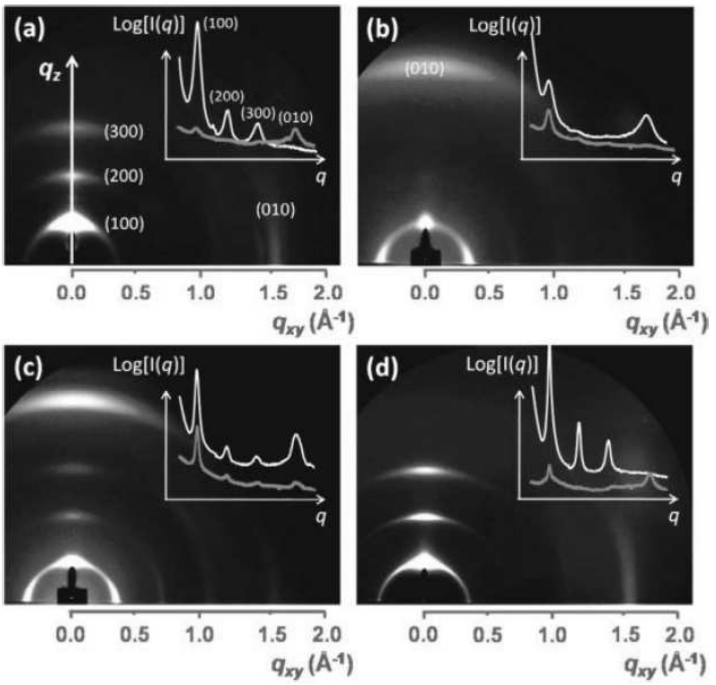

Figure 8.20: Two dimensional GIXD patterns of drop cast (a) and spin cast (b-d) rr-P3HT ($M_W = 33.6\,\mathrm{kg/mol}$) films from $CHCl_3$ solution onto hydrophilic SiO_2 substrate; (b) as prepared; (c) annealed at 200 °C for 12 h; (d) melt-crystallized from 240 °C with a cooling rate of 2 °C/min. The insets show 1D X-ray profiles along the z-axis (above) and in the xy-plane (below). Figure taken from Yang et al.[23]

the xy-plane coming from edge on π-stacking of the oligomer chains. So a complete transition from face-on to edge-on alignment was observed upon annealing spin cast films.

GIXD data for drop cast films had a pattern similar to this melt crystallized spin cast films (Fig. 8.20). Additionally, short nanorods with lengths of 50-80 nm formed in annealed films and well developed crystalline nanofibrils appeared after melt crystallizing as seen in AFM pictures. Yang et al.[23] concluded that crystalline morphology and orientation relative to the (hydrophilic) substrate can be improved by temperature treatment. Still charge mobility as high as for drop cast films could not be achieved. The group suggest that oxide degradation might have occurred (annealing was done at 10^{-2} Torr).

8.6 Combinational Study on morphology

In this section a summary of findings from Kline et al.[31] is given (Tab. 8.2). Apart the from annealing experiments mentioned above, they also investigated deposition from xylene and drop casting from $CHCl_3$. In contrast to Chang et al.[8] they did not observe nanofibril structure for high M_W films; instead they saw nodulelike film topography. This could be caused by the difference in solvent. Chang et al. used TCB but Kline et al. preferred xylene. Both have high boiling temperature, but probably different solubilities for P3HT. Still, longer evaporation times (xylene spin cast and $CHCl_3$ drop cast) seemed to promote longer nanofibrils for low M_W films and edge on alignment for the entire range of M_W. Additionally higher conjugation was observed from absorption spectra for high M_W.

Table 8.2: Summary of parameters found for differently prepared samples. In all cases HMDS treated SiO_2substrates were used. P3HT films with regioregularities $> 98\,\%$ were cast from chloroform $T_M = 60\,°C$ or xylene $T_M = 140\,°C$. Mobilities were extracted from FET measurements. Alignment in respect to the plane was recorded from GIXD. Morphology was depicted by tapping mode AFM. Data is taken from Kline et al.[31]

sample	M_W kg/mol	mobility Vs/cm^2	alignment	morphology	$\pi - \pi^*$ absorption peak nm
Spin cast $CHCL_3$	3.3	2×10^{-6}	face on	≈ 100 nm long nanofibrils	≈ 500
Spin cast $CHCL_3$, annealed	3.3	2×10^{-4}	mixed	≈ 150 nm long nanofibrils	-
Drop cast $CHCL_3$	3.3	4×10^{-5}	mixed	> 200 nm long twisted nanofibrils	-
Spin cast xylene	3.3	7×10^{-5}	mixed	≈ 200 nm long nanofibrils	-
Spin cast $CHCL_3$	34	8×10^{-3}	face on	nodulelike	≈ 520
Spin cast $CHCL_3$, annealed	34	7×10^{-3}	face on	nodulelike	-
Drop cast $CHCL_3$	34	7×10^{-3}	mixed	nodulelike	-
Spin cast xylene	34	3×10^{-2}	edge on	nodulelike	-

8.7 Summary

The alignment and morphological structure of rr-P3HT for spin and drop casted films were investigated by many research groups. These two properties had a big influence on the charge carrier mobility. The conductivity of the films was higher when the backbone of the polymer was in edge-on position relative to the substrate. Face-on alignment yilded a lover conductivity for the prefered FET geometry (Fig. 8.4). Films prepared through deposition methods with slow solvent evaporation tended to have edge-on alignment.

The morphology did depend on the molecular weigth and the solvent evaporation time. AFM pictures showed, that the nanofibrills lengths and widths increased with rising M_W. This was directly associated with a better conductivity for high M_W polymers. Some care had to be taken when choosing the right solvent; polymers with M_W higher than approximately 20kg/mol needed to be depositetd with slow solvent evaporation time in order to achive the full possible conductivity.

Chapter 9

Electical properties

In this chapter various electrical properties of devices based on P3HT, that were measured by other research groups, are discussed. First, the issue of contact resistance is addressed. It is important to know, if it would compromise the mobility measurements. Than the gate voltage dependence of the mobility is analyzed. Finally, all data found on temperature dependence of the charge carrier mobility of P3HT based devices is presented.

9.1 Contact Resistance

Apart from the resistance of the conducting channel between source and drain, also the contact resistances between the electrodes and the accumulation layer needs to be considered. In a field effect transistor, the convention is to keep the source contact at ground level, while a positive voltage is applied to the drain. In this configuration electrons are injected from the source contact and removed at the drain contact. Contact resistances arise from voltage drops on the way from the contacts to the accumulation layer.

Panzer et al.[41] report $R_S = 200\,\mathrm{k\Omega cm}$ and $R_D = 50\,\mathrm{k\Omega cm}$ for source and drain contact resistance respectively acquired by the four probe method for top contact bottom gate FETs. They, however, do not provide further details.

More data can be found in the literature for bottom contact FETs. Bürgi et al.[38] succeeded in measuring the electrostatic potential across the channel of operating transistors. Noncontact scanning-force microscope in scanning Kelvin probe mode based on the frequency modulation technique in ultrahigh vacuum was applied. Potential profiles are shown in Fig. 9.2. Potential drops (ΔV_S and ΔV_D) in the vicinity of the contacts can be assigned to contact resistances. The origin of contact resistance can be (1) Shotky barriers at the electrode-semiconductor interfaces and (2) bulk resistance of the semiconductor between the electrodes and the accumulation region. A simplified TFT (Fig. 9.1) circuit is suggested by

$$R_{S-D} = R_S + R_{ch} + R_D = R_i + 2R_b + R_{ch}, \tag{9.1}$$

where the source contact resistace

$$R_S = R_i + R_b \tag{9.2}$$

is divided into hole injection resistance R_i and bulk resistance R_b and the drain contact resistance

$$R_D = R_b \tag{9.3}$$

consists only of bulk resistance R_b.

Since the contact resistances in Fig. 9.2 were symmetrical $R_S \approx R_D$ the injection barrier was negligible. Both sides were dominated by the bulk resistance. This could be explained by the good matching of P3HT ionization potential $IP = 5.0\,\mathrm{eV}$ and the work functions $W \approx 5.2\,\mathrm{eV}$ and $W \approx 4.89\,\mathrm{eV}$ for Au and Cr-Au respectively. So the Shotky injection barrier $\phi_b = I - W$ is fairly low.

Temperature dependent measurements revealed that the product of contact resistance and field effect mobility $R_S \times \mu_f$ was constant over a range of 300 - 90 K for Cr-Au electrodes (Fig. 9.3). Bürgi et al.[6] concluded, that the contact resistance was dominated by charge carrier mobility of the polymer in this case.

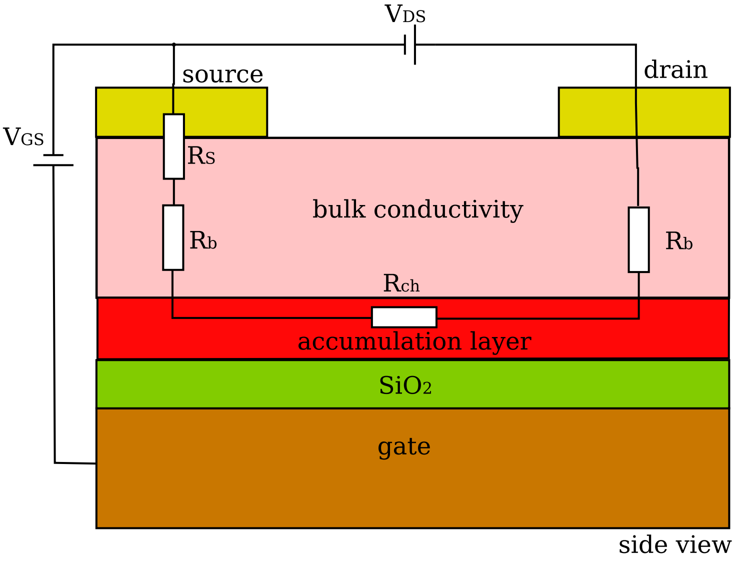

Figure 9.1: A simplified electric circuit of a TFT. The overall source to drain resistance R_{S-D} can be splitted into $R_{S-D} = R_S + R_{ch} + R_D = R_i + 2R_b + R_{ch}$. Note that the picture is not in scale; the thickness of the semiconductor is orders of magnitude smaller than the channel length.

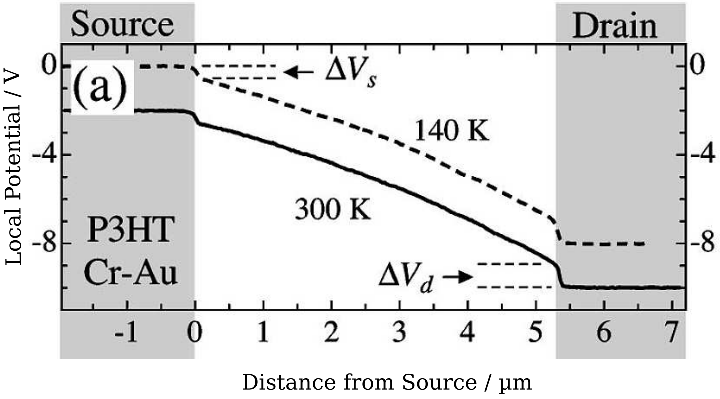

Figure 9.2: Potential profile across the channel of an operating transistor at 300 K and 150 K. The active material is P3HT, spin coat on top of Cr - Au source/drain electrodes. ($L = 5.3\,\mu$m, $V_GS = -20$ V, $V_DS = -8$ V) The profile taken at 300 K is offset by -2 V for clarity. This figure is taken from Bürgi et al.[6]

In other words, there was some narrow zone with probably low charge carrier concentration between the gold contacts and the accumulation region but with the same mobility, which led to $R_S \propto \mu_f^{-1}$. The reported values for the source contact resistance were $< 5\,\mathrm{k\Omega cm}$ and $22\,\mathrm{k\Omega cm}$ ($n = 2 \times 10^{12}\,\mathrm{cm}^{-2}$)for Au and Cr-Au electrodes respectively. Note that this measurements were carried out using bottom contact FETs. They may be still valid for top contact FETs, because the width of the low charge carrier concentration zone which was estimated to be $\approx 100\,\mathrm{nm}$ is comparable to the P3HT film thickness $\approx 40\,\mathrm{nm}$ for devices examined in this diploma thesis. Also Gundlach et al.[19] found, that contact resistance was smaller for top contacts in the case of pentacene based FETs, this was probably because of larger contact areas at a short distance from the accumulation layer. Hill[22] simulated both layouts and came to a similar conclusion. On the other hand, one must keep in mind, that there may be some anisotropy of the mobility in the substrate-in-plane direction and perpendicular to the substrate direction, particularly in the case of high $\mathrm{M_W}$ P3HT spin cast from TCB.

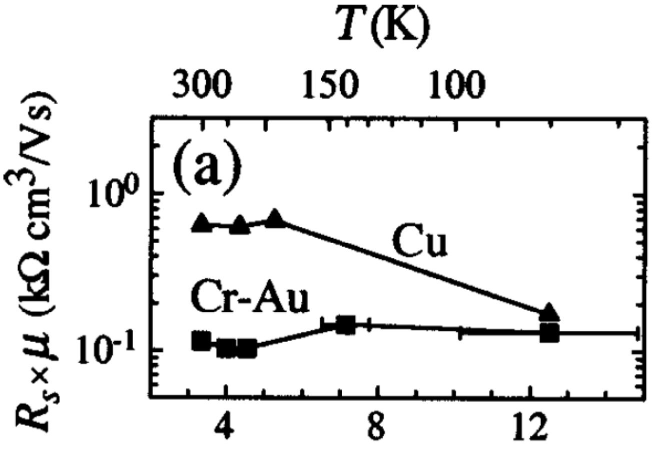

Figure 9.3: Product of the source contact resistance and field effect mobility as a function of inverse temperature of P3HT transistors with Cr-Au and Cu contacts. ($V_{GS} = -30\,\mathrm{V}$) This figure is taken from Bürgi et al.[6]

In order to estimate the significance of contact resistance for FETs build in the course of this diploma thesis, contact resistances R_S, R_D should be compared to channel resistance R_{ch}. In our measurements channel resistances were not accessible, the only known quantity was the overall FET resistance

$$R_{S-D} = \frac{V_{SD} \cdot W}{I_D}. \tag{9.4}$$

Only resistances acquired at the same charge carrier density

$$n = \frac{C_i |V_{GS}|}{e} \tag{9.5}$$

can be compared. We had 150 nm $\mathrm{SiO_2}$ layer thickness, so the charge carrier density ($n = 2 \times 10^{12}\,\mathrm{cm}^{-2}$) was achieved at $V_G \approx -15\,\mathrm{V}$. FET resistances ranged from $R_{S-D} = 200\,\mathrm{k\Omega\,cm}$ to $R_{S-D} = 9\,\mathrm{M\Omega\,cm}$. These values were much higher than abovementioned contact resistances. Also since $R_S \propto \mu_f^{-1}$, contact resistance should not obscure mobility vs. temperature curves. Therefore it was assumed that the FET resistance was equal to the channel resistance $R_{S-D} \approx R_{ch}$ in the rest of this diploma thesis.

9.2 Gate voltage dependence of the mobility

The charge carrier mobility in semiconducting polymers is not constant for different gate voltages. With negative gate bias, the charge carrier density at the insulator/semiconductor interface is increased. These additional charges fill more traps and the overall mobility increases. A n-dependend mobility in P3HT FETs at different temperatures was obtained by Bürgi at al.[7] by means of scanning Kelvin prob microscopy (SKPM). The dependence of V_G on μ was found to be linear at room temperature, but superlinear at low temperatures (Fig. 9.4). The temperature dependend slope in the logarithmic plot can be interpreted with the MTR model. As seen in equation (5.17), the temperature value is in the exponent term of V_G, leading to higher slopes of $\ln \mu$ vs. $\ln V_G$ plots at lower temperatures.

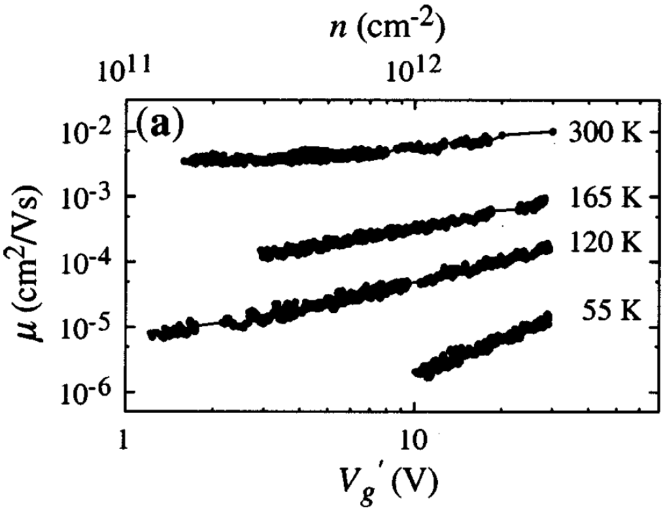

Figure 9.4: Field-effect mobility μ_f of P3HT ($M_W = 19\,\mathrm{kg/mol}$, 98 % regioregularity, spin cast from $CHCl_3$) dependence on charge carrier density n and temperature. Figure taken from.[7]

9.3 Cryogenic measurements

In this section electric measurements of the temperature dependent mobility of P3HT published by different groups are summarized.
Sirringhaus et al.[53] observed a roughly Arrhenius-type temperature dependence for all samples and activation energies and mobilities which increased with rising regioregularity (Fig. 9.5 and Tab. 9.1). Their semiconducting films were spin-coated or drop cast from 11.84 g/l solution in $CHCl_3$ on SiO_2 substrates treated with hexamethyldisilazane. The film thickness was measured to be in the range of 70-100 nm. Top (gold) contact bottom gate layout was used.

The authors conclude that at high gate voltages and temperatures charge carrier enter a regime where the distance to the transport level is sufficiently low that they can be thermally activated. Charge modulated spectra (CMS) showed polaronic energy levels which shifted towards the highest occupied π or lowest unoccupied levels π^* compared to isolated polythiophene radical cations in solution. The shift was attributed to lower reorganisation energies of polarons that were spread over severall chains and not confined to a single polymer chain.

Table 9.1: Activation energy and mobility at 300 K for different P3HT samples cast on **HMDS treated** SiO_2. Data taken from Sirringhaus et al.[53]

deposition method	M_W kg/mol	PDI	rr %	μ_{300K} cm²/Vs	E_a meV
drop cast	175	2.5 - 2.6	81	3×10^{-3}	–
spin cast	175	2.5 - 2.6	81	1×10^{-4}	115
spin cast	28	1.4	95	1×10^{-2}	100
spin cast	28	1.4	96	3×10^{-2}	84

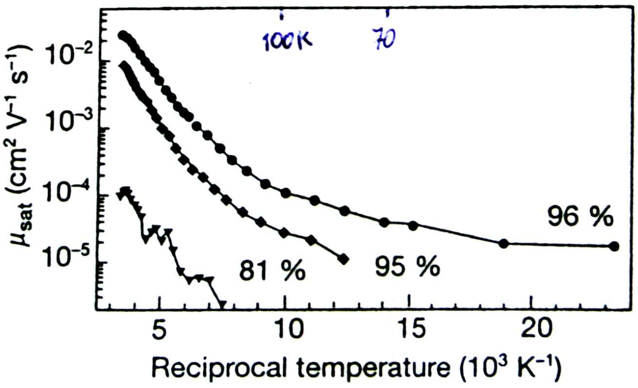

Figure 9.5: Mobility vs. Temperature for three P3HT samples with different degree of regioregularity **spin cast** onto **HMDS treated** SiO_2. More details about the P3HT films can be found in the table 9.1. Figure adopted from Sirringhaus et al.[53]

Aleshin et al.[2] report a mobility dependence of the temperature of the form

$\mu = \mu_0 \exp\left(-\frac{T_0}{T}\right)^{1/3}$ for extremely thin rr-P3HT films (Fig. 9.6). The FETs were build from 0.48 - 2.5 g/l $CHCl_3$ solution, by spincoating at 8000 rpm onto HMDS treated SiO_2 substrate with gold bottom source and drain contacts. P3HT from Aldrich Chemical co was used (M_W and PDI not given). The semiconductor film thickness was measured 5 - 10 nm; mobilities were extracted between 90 K and 300 K. T_0 was found to be 2.64×10^6 K and 2.78×10^6 K. The model supports variable-range hopping (VHR) of charge carriers in an 2D disordered system,[37] in contrast to thicker films that usually follow the Arrhenius dependence.

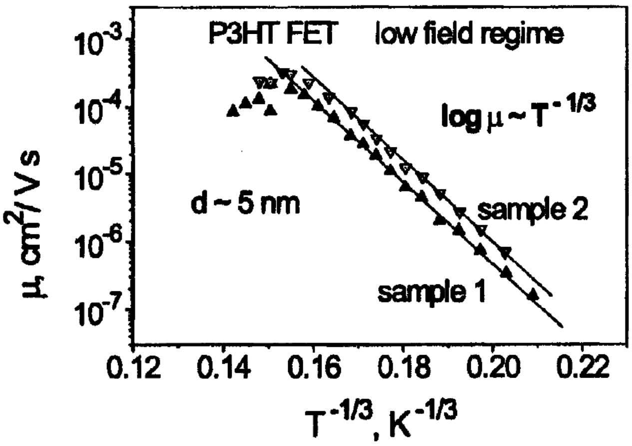

Figure 9.6: Mobility vs. $T^{-1/3}$ for extremely thin 5 - 10 nm rr-P3HT films. Mobility was extracted from characteristics of FETs build by spin casting P3HT from 0.48 - 2.5 g/l $CHCl_3$ onto HMDS treated SiO_2. Figure taken from Aleshin et al.[2]

Bürgi at al.[7] measured the mobility with SKPM down to 55 K for $M_W = 19\,\mathrm{kg/mol}, PDI = 1.35$, 98 % regioregularity P3HT spin cast from 3.7 g/l $CHCl_3$ solution onto HDMS treated SiO_2. Gold bottom contacts were used and rr-P3HT layer thickness was between 20 nm and 30 nm. Reported activation energies for an assumed $\ln(\mu) \propto 1/T$ relation were 100 meV and 90 meV for contact resistance corrected mobilities at $V_G' = -10$ V and $V_G' = -30$ V respectively (Fig. 9.7).

Kline et al.[31] obtained activation energies for three M_Ws ranging from $M_n = 3\,\mathrm{kg/mol}$ to $M_n = 33\,\mathrm{kg/mol}$. They measured FET mobilities for P3HT films spin cast from THF (tetrahydrofuran, boiling point $T_B = 64$ C) solution. The P3HT film thickness was in the range of 20 - 50 nm. Bottom contacts FET geometry with gold contacts was used. The mobilities of all polymers followed the Arrhenius temperature dependence in the 120 - 300 K range with E_a increasing slightly with decreasing M_W from 54 meV to 69 meV (Fig. 9.8 and Tab. 9.2).

Chang and coworkers[8,9] measured rr-P3HT mobilities for a wide range of M_W down to 90 K. The experimental setup was HMDS treated SiO_2 with bottom gold contacts with P3HT spin cast from 10 g/l $CHCl_3$ or 1,2,4-trichlorobenzene (TCB) solutions. Apart from the mobility also the overall activation energy E_a^μ dependence on temperature is given (Tab. 9.3 and Fig. 9.9). The authors claim,

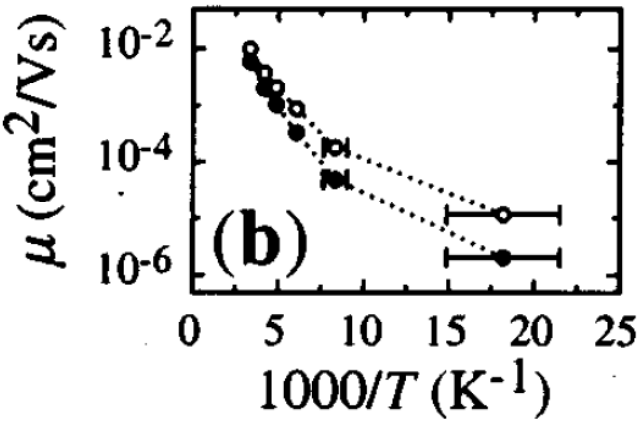

Figure 9.7: Temperature dependence of the field-effect mobility $\mu_f(T, V_G')$ for $V_G' = -10\,\mathrm{V}$ (closed symbols) and $V_G' = -30\,\mathrm{V}$ (open symbols). The molecular weigth of the rr-P3HT was $M_W = 19\,\mathrm{kg/mol}$ and it had 98 % regioregularity. The FETs were produced by **spin casting** from **$\mathbf{CHCl_3}$** onto **HMDS treated** SiO_2. Figure taken from Bürgi at al.[7]

Table 9.2: Activation energy and mobility at 300 K for different P3HT samples **spin cast** onto **HMDS treated** SiO_2. Data taken from Kline et al.[31]

M_n kg/mol	rr %	μ_{300K} cm²/Vs	E_a meV
< 4	98	4×10^{-6}	69
10	98	2×10^{-4}	62
> 30	98	6×10^{-3}	54

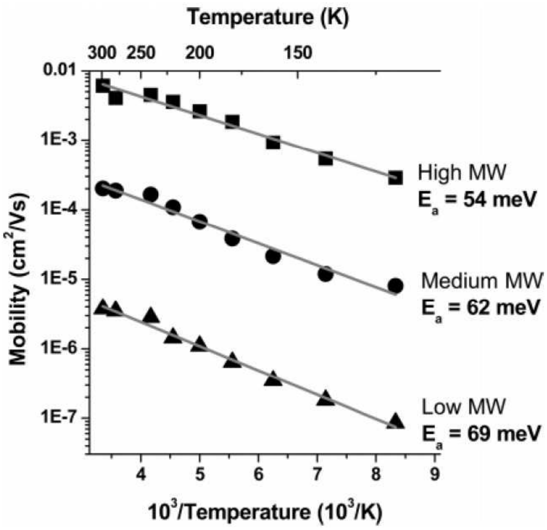

Figure 9.8: FET mobility as a function of temperature for three different M_Ws in the range of 3 - 35 kg/mol. Devices were prepared by **spin casting** P3HT from **THF** onto **HMDS treated** SiO_2 substrate. Figure taken from Kline et al.[31]

that fitting their transfer curves with the mobility equation of Vissenberg and Matter gave poor results. Instead they used a modified ME model with double exponential tail state density and included a relatively small additional polaronic activation as extracted from their CMS spectra (Tab. 8.1).

Table 9.3: Mobility and activation energies for rr-P3HT with different M_W and different solvents used for **spin casting** onto **HMDS treated** SiO_2. The activation energies were extracted in the temperature range of 300 - 90 K using bottom gold contact FETs for different gate voltages. Data taken from Chang et al.[8,9]

solvent	M_W kg/mol	PDI %	μ_{300K} cm²/Vs	$E_a(VG = -80\,\mathrm{V})$ *meV*	$E_a(VG = -30\,\mathrm{V})$ *meV*
TCB	270	2.3	1×10^{-1}	45	75
TCB	37	–	5×10^{-2}	50	75
TCB	15	1.5	3×10^{-3}	110	140
$CHCl_3$	270	2.3	2×10^{-2}	–	–
$CHCl_3$	37	–	1×10^{-2}	–	–
$CHCl_3$	15	1.5	3×10^{-2}	85	120

Kažukauskas et al.[59] report comparable mobilities for rr-P3HT from Sigma Aldrich. In their research they used a stacked geometry similar to that used for OLEDs. They did spin coating on ITO with polymer thicknesses from 620 nm up to more than 1 *μm*; then, an aluminum layer was evaporated on top. Subsequently, the bulk mobility was recorded by the *charge extraction in a linearly increasing voltage* (CELIV) method.[29] Note that most other groups

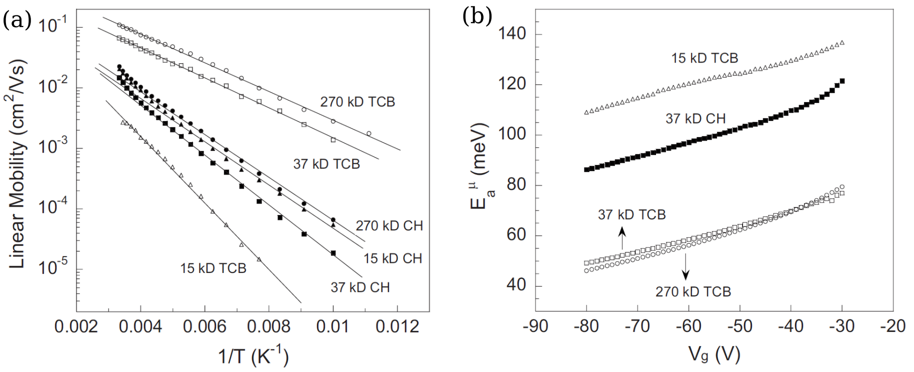

Figure 9.9: (a) Mobility and (b) overall activation energies for rr-P3HT with different M_W and different solvents used for spin casting onto **HMDS treated** SiO_2; chloroform (CH) and 1,2,4-trichlorobenzene (TCB). Figure taken from Chang et al.[9]

measure mobility from FET transfer curves where the interface to the oxide plays a significant role. Kažukauskas et al. found the activation energy to be in the range of 140 meV to 170 meV when using the empirical Poole-Frenkel model:

$$\mu = \mu_0 \exp\left\{-\frac{E_0 - \alpha\sqrt{F}}{kT_{eff}}\right\} \qquad \text{with} \qquad \frac{1}{T_{eff}} = \frac{1}{T} - \frac{1}{T_R}, \tag{9.6}$$

where F is the electric field, E_0 is the activation energy for the charge carriers at zero electric field, T_R is the empirical reference temperature at which the mobility is supposed to be known. Due to the limited investigated temperature range, they could not distinguish between $\ln(\mu) \propto 1/T$ and $\ln(\mu) \propto 1/T^2$ thermal activation.

In addition, field dependence of mobility at different temperatures was studied. Spin cast films had the expected positive slope in $\sqrt{\vec{E}}$ vs. $\ln(\mu)$ plots, while drop cast films had negative slope at low fields (Fig. 9.10). In terms of Bässlers model this means that drop cast films have higher spatial disorder. This probably makes sense, if assuming that the film morphologies of Kažukauskas et al. are similar to the morphologies of films prepared by drop casting onto HMDS treated SiO_2, the polymer backbones should adopt edge-on alignment relative to the substrate. For TFTs the edge-on orientation increases mobility in the direction parallel to the substrate. For stacked devices (as used in this case), where current flows perpendicular to the substrate, face-on orientation is more favorable. Spin cast films tend to have face on alignment of the backbones and a higher mobility perpendicular to the ITO substrate and to the Al electrode. In other words, spin cast films have a more desirable alignment for stacked structures, while drop cast films are more suitable for TFT geometries in terms of mobility. A speculative explanation for the data showed in (Fig. 9.10) is to relate higher mobility to lower spatial disorder resulting in negative slope of $\sqrt{\vec{E}}$ vs. $\ln(\mu)$.

To conclude, carrier transport is always temperature assisted and shows Arrhenius dependence down to about 100 K in most cases. Chang and coworkers[9]

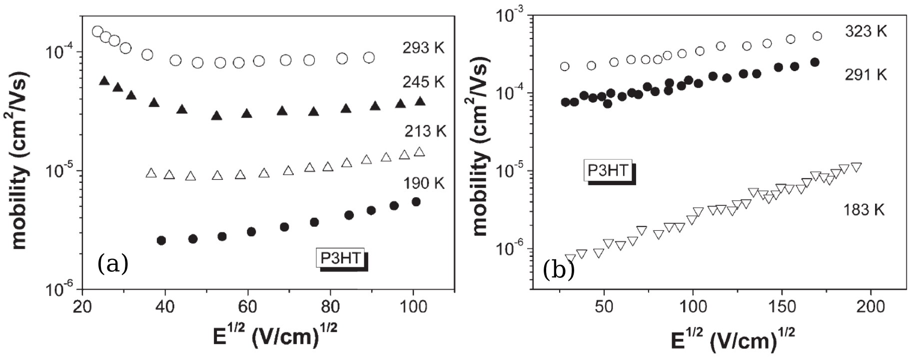

Figure 9.10: Bulk mobility vs. electric field for P3HT deposited on ITO. (a) drop cast, (b) spin cast. Only in drop cast films negative mobility slope is observed at low electric field. Figures taken from Kažukauskas et al.[59]

pointed out that at temperatures below 100 - 150 K, the mobility shows a weaker temperature dependence (Fig. 9.5 and Fig. 9.7). They attributed this to hopping (tunneling) in the tail of the localized states or hopping in the presence of Coulomb interactions.

9.4 Mobility at elevated temperatures

Above room temperature an increase of the temperature activated mobility can be compensated by a disturbed P3HT structure. Measurements at elevated temperatures were done by Zen et al.[1] and Aleshin et al.[2] As seen in Fig. 9.11 and Fig. 9.6 the reported mobilities decrease ar elevated temperatures. High M_W materials are less affected, probably because there the chains are geometrically more constrained.

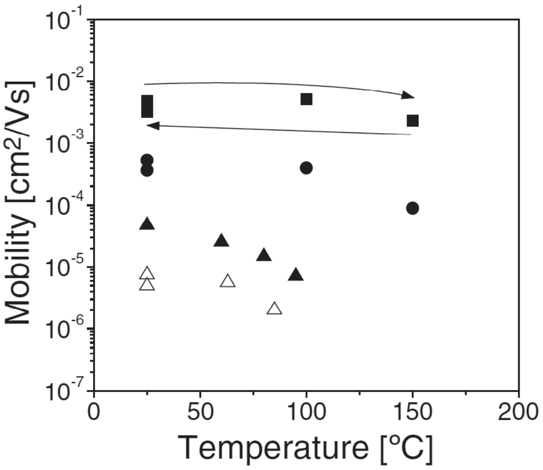

Figure 9.11: FET mobility at elevated temperatures for rr-P3HT with different M_W **spin cast** from $\mathbf{CHCl_3}$ onto **HDMS treated** SiO_2 substrate. (△, ▲) $M_W = 6.6\,{}^{kg}/_{mol}$, (●) $M_W = 20\,{}^{kg}/_{mol}$, (■) $M_W = 25\,{}^{kg}/_{mol}$. Substrates were annealed at 150 °C for 5 min prior to this temperature dependent electrical characterisation. Figure taken from Zen et al.[1]

Part IV

Experimental

Chapter 10

Experimental methods

In the course of the diploma thesis OTFTs with rr-P3HT as active semiconductor were produced. Transfer curves were recorded at temperatures in the range between 300 K and 70 K in the cryostatic setup. Various other electrical measurements were done at room temperature and above room temperature inside a glovebox. In this chapter the fabrication of the devices and the setup for electrical measurements is described.

10.1 Sample preparation

In all our measurements, the same device setup was used. The first layer is a highly doped silicon that acts a common gate. Next is a thermally grown silicon oxide SiO_2 that insulates the gate from the rest of the transistor. On top of the oxide, the organic semiconductor is deposited by spin coating. In the last step, source and drain contacts are added by evaporating gold onto the semiconductor through a shadow mask. The device dimensions are shown in Fig. 10.1

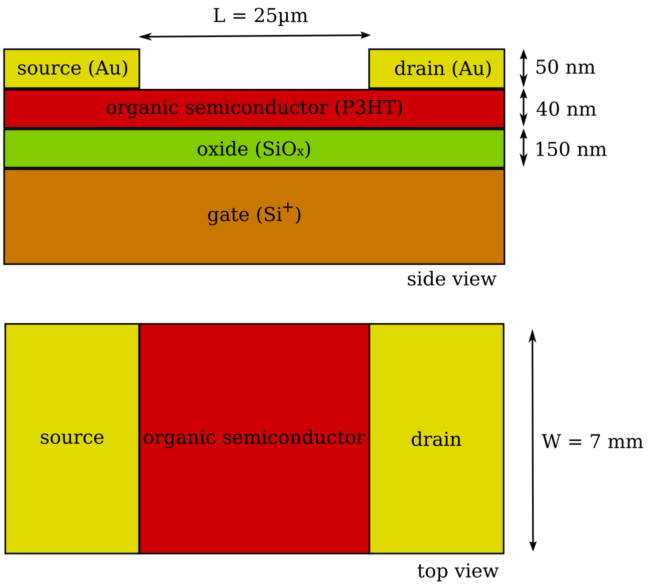

Figure 10.1: Layout of transistor devices as used in this work.

In the following the fabrication is discussed in more detail:

10.1.1 Substrate

The Si substrate was purchased from Siegert Consulting e.K. and was originally manufactured by Siltronics. It is highly doped with a resistivity $< 10\,\Omega\text{cm}$, which corresponds to a doping concentration of more than $3 \times 10^{14}\,\text{cm}^{-3}$. Both sides have thermally grown SiO_2 layers with a thickness of 154 nm and a roughness of $\sigma = 0.52\,\text{nm}$ as measured by Heinz-Georg Flesch using X-ray Reflectometry (XRR). One such SiO_2-layer has a capacity of $C_i = 20 \times 10^{-9}\,{}^{\text{C}}\!/\!{}_{\text{cm}^2}$. The wafer were pre-cut into pieces of $2 \times 2\,\text{cm}$. More details can be found in Fig. 10.2.

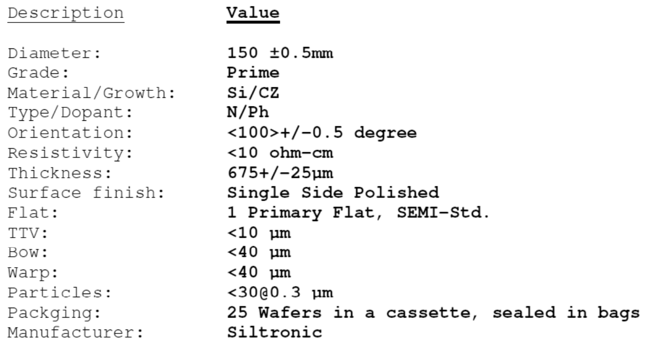

Description	Value
Diameter:	150 ±0.5mm
Grade:	Prime
Material/Growth:	Si/CZ
Type/Dopant:	N/Ph
Orientation:	<100>+/-0.5 degree
Resistivity:	<10 ohm-cm
Thickness:	675+/-25µm
Surface finish:	Single Side Polished
Flat:	1 Primary Flat, SEMI-Std.
TTV:	<10 µm
Bow:	<40 µm
Warp:	<40 µm
Particles:	<30@0.3 µm
Packging:	25 Wafers in a cassette, sealed in bags
Manufacturer:	Siltronic

Figure 10.2: Specifications of the substrates used in this work. The picture is copied from the data sheet provided by Siegert Consulting e.K.

10.1.2 Semiconductor deposition

All work with the semiconducting polymer was done in a glove box under argon atmosphere. To avoid irradiation damage the pure polymer and it's solutions were protected from continuous illumination by wrapping them in aluminum foil. The P3HT samples were dissolved in 1,2,4-trichlorobenzene (TCB) with a concentration of 2 g/l before deposition. TCB (anhydrous grade) was purchased from Sigma Aldrich. It has a boiling temperature of $T_B = 214\,^\circ\mathrm{C}$ and a density of $\rho = 1.454$ g/mL at $25\,^\circ\mathrm{C}$.

Spin coating was done by sticking the substrate to the rotary disk than dripping roughly $100\,\mu$l of the solution onto the substrate until the whole surface was covered. In the next step, the disk was spinned at 1500 rpm for 40 sec allowing excessive solvent to flow off. In former experiments[1] where the same spin coating parameters were used, with the exception that the solvent was not TCB but $CHCl_3$, the resulting film thickness as measured by XRR was $d \approx 15$ nm and the roughness was $\sigma = 0.56$ nm. Film thickness was not measured for films that were spin cast from TCB.

Since TCB has a high boiling temperature, the sample was kept on the rotary disk for approximately 10 min until all solvent that remained after spinning had evaporated. Than the substrate was dried on a hot plate at $70\,^\circ\mathrm{C}$ for up to one hour. A review covering the physics behind the spin coating process is given by Schubert and Dunkel.[51]

10.1.3 Electrode fabrication

Gold Electrodes were evaporated onto the semiconductor layer. The vacuum chamber used for the electrode fabrication was located inside a glovebox. The sample could be kept in argon atmospehere or vacuum in all production steps, starting from solvent preparation. Electrode evaporation was done by placing the substrates with the P3HT layer face down on a shadow mask, which was then inserted into a vacuum chamber with the gold evaporator below.

The shadow mask was designed so that 4 transistor devices with 2 common gate contacts could be build on one substrate. The source and drain contacts of

---

[1] Sample preparation was done by Marco Marchl and XRR measurements were done by Heinz-Georg Flesch

each transistors were realized by one big gold pad that was split into two sides by a tungsten wire with a diameter of $d = 25\,\mu$m. The tungsten wires were attached to the shadow mask. Consequently, the channel width was $25\,\mu$m and the channel length was 7 mm. The gate contacts were realized by scratching through the oxide at the zones where gate pads would be evaporated (The scratching was done before placing the substrate onto the shadow mask). Fig. 10.3 shows a shadow mask for one substrate. The sample-holder in the vapor deposition chamber held four such masks; so up to four substrates could be processed simultaneously.

After putting the substrate into the chamber, it was evacuated to at least 3×10^{-5} mbar (usually overnight) than gold was thermally evaporated by electric heating. The gold vapor particles flew in ballistical regime through the openings in the shadow mask and condensated on the P3HT layer. Electrode thickness was monitored by a micro balance. Usually 50 nm thick gold layer were evaporated.

A picture of the final sample consisting of the substrate with semiconductor film and electrodes on top of it is shown in Fig. 10.4.

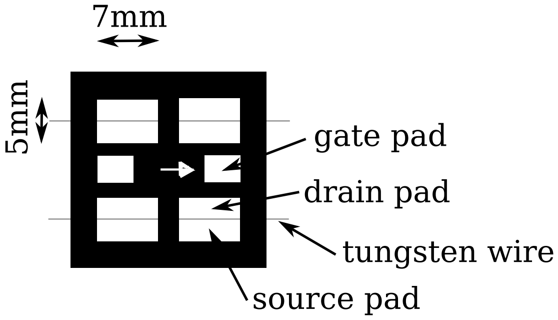

Figure 10.3: Shadow mask through which gold contacts were evaporated on top of the semiconductor. Four devices with two common gate contacts were realized in this setup. The channels of the devices were created by fixing a thin tungsten wires with a diameter of $25\,\mu$m to the shadow mask.

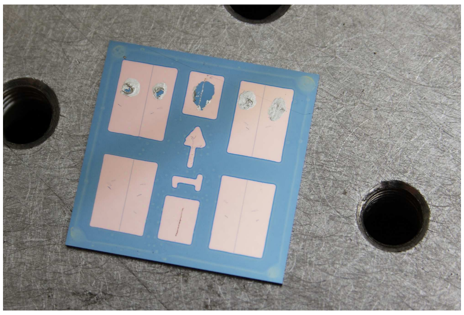

Figure 10.4: Used substrate after removal from the cryostat. Four transistors with source and drain electrodes as well as two gate pads can be seen. The upper devices were connected with small drops of conductive silver which skinned the gold pads after removal of the substrate from the sample holder.

10.2 Measurement setup

After device fabrication, the devices were electrically characterized for the first time, while still in argon atmosphere. Source, drain and gate pads were contacted using needles with MDL positioners from Cascade Microtech. The needles were connected to an Agilent E5262A parametric analyser via coaxial cables. Electric shielding was not that important because only DC voltages and currents were measured. Drain and gate voltages in the range of -100 V to +100 V could be applied and the respective current could be measured. The source contact was kept at ground level and source current could not be measured because the parametric analyzer had only two source measure units.

10.2.1 Cryostatic setup

For measurements below room temperature, the sample had to be transferred to the cryostat (Continuous Flow Cryostat CF 1204 from Oxford instruments). To do that, it was unavoidable to expose the samples to ambient air because the cryostat did not fit into the locks of the glovebox. To avoid damage to the semiconductor, it was kept in darkness or soft light when handled outside argon atmosphere. Effects of exposure to air are discussed later.

The device connection in the cryostat is different from those in the glovebox. In the original version of the sample holder, four leaf springs with small tips at their ends were used to contact two devices and two simple lacquer isolated wires were attached with conductive silver to the two gate pads (Fig. 10.5). Inserting a substrate between the ground plate of the holder and the tips was difficult because the attachment of the springs was permanent. They had to be pressed up while the substrate was slid into the gap between the ground plate and the tips without scratching the devices. Due to frequent use, the tention of the leaf springs decreased with time and reliable connecting became even more complicated. In our first experiments contacts failed at temperatures around 160 K probably because of mechanical stress and insufficient pressure of the tips.

We decided to redesign the sample holder to solve these problems. The new design is shown in Fig. 10.6 and Fig. 10.7. Five connecting spring leaves were removed from a relays purchased from RS-components(product name: V23154, RS-identification number: 268-4468). They were glued to plastic platelet which could be screwed to a plastic distance holder below. Four springs were used to contact two devices and the fifth spring in the middle to contact one common gate pad. In this configuration, 2 devices (consisting of two times source and drain and one common gate) could be examined without removing the sample holder from the cryostat. All springs were soldered to wires which were fed through to the parametric analyser. By detaching the platelet it is far more convenient to install the sample into the holder and the springs retain their tension for a longer time.

Conducting silver was used to further enhance the connection between the ends of the springs and the gold pads. With the conducting silver electrical contact could be maintained, ewen if the gold pads were scratched of directly underneath the tips. Together with the higher contact pressure between the tips and the gold pads achieved with the new sample holder, electric measurements could be done in the whole accessible temperature range of the cryostat.

Figure 10.5: Photo of the original sampleholder with installed sample.

After attaching and connecting the devices to the sample rod, it was inserted into the cryostat chamber. Subsequently, the cryostat sample space was evacuated and than helium gas was let in, in order to have good thermal connection to the heat exchanger, without exposing the sample to gasses that could condensate at low temperatures. The overall setup is shown in Fig. 10.8.

To cool the device, nitrogen was pumped from a dewar through a transfer tube into the cryostat by a membrane pump controlled by the VC 30 flow control meter. In the beginning the nitrogen was in liquid state. At some point depending on the flow rate, usually in the transfer tube, it evaporated and reached the heat exchanger at some temperature above 77 K. The nitrogen cooled the heat exchanger inside the cryostat which was thermally connected with helium gas to the sample and also mechanically connected to the sample holder. In order to get lower temperatures, the flow rate had to be increased. Even temperatures below 77 K are feasible: at very high flow rates liquid nitrogen is massed in the vicinity of the heat exchanger and than it is allowed to evaporate and to withdraw heat of vaporization from the surroundings.

For good thermal insulation between the nitrogen and the environment in the lab, the inner parts of the cryostat and the transfer tube were separated by evacuated space from the ambient warm air. Two turbopumps were used, one evacuated the transfer tube and one evacuated the cryostat vessel.

Instead of nitrogen, liquid helium could be used in the same setup. For our devices, cooling with nitrogen seemed sufficient, because currents became hard to measure even at 80 K, where they had a value of few nA. Cooling to lower temperatures would make sense, if the channel width would be increased from 7 mm to much higher values by using an interdigitated geometry, but this is not

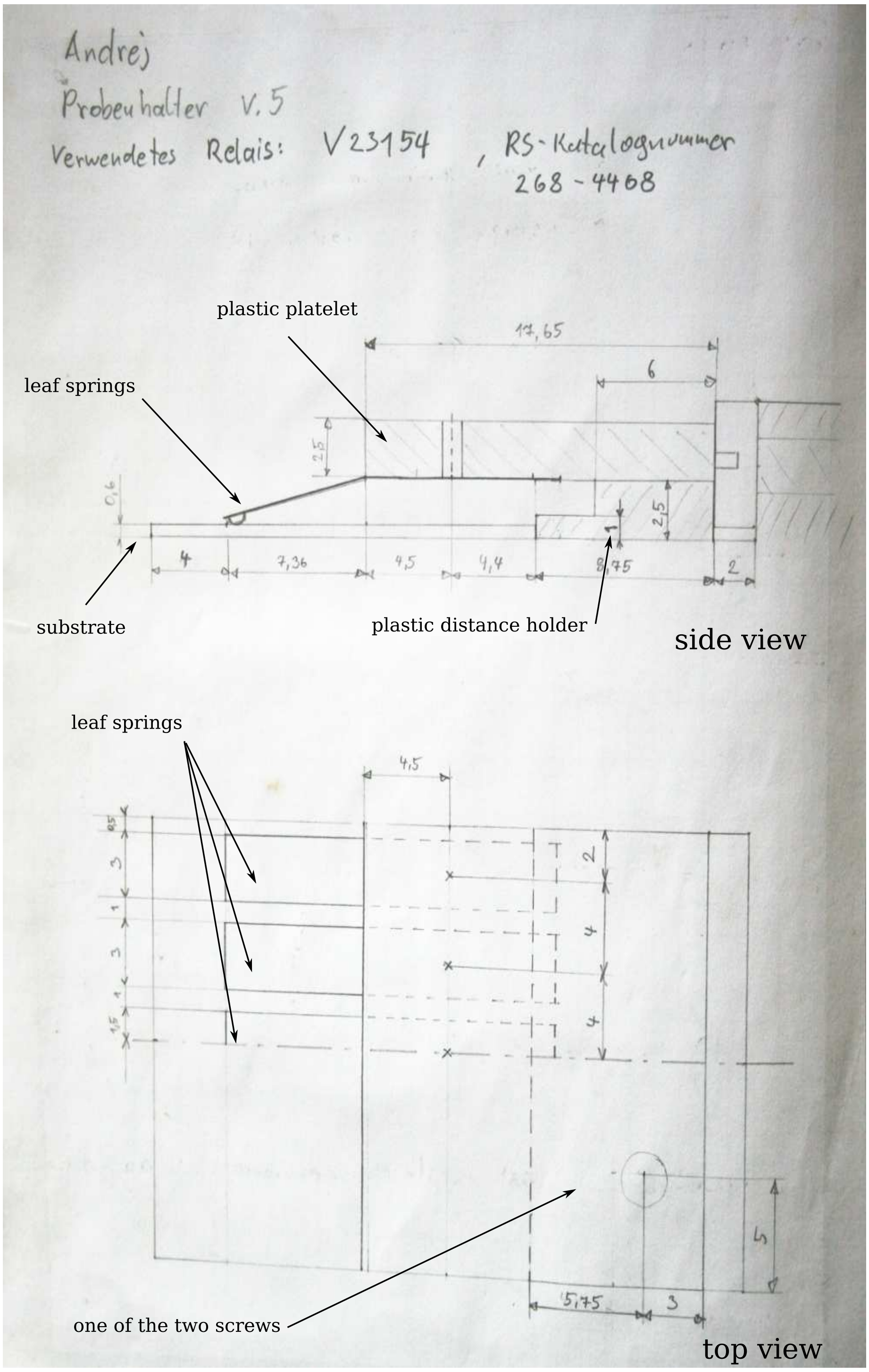

Figure 10.6: The new sampleholder used in our experiments.

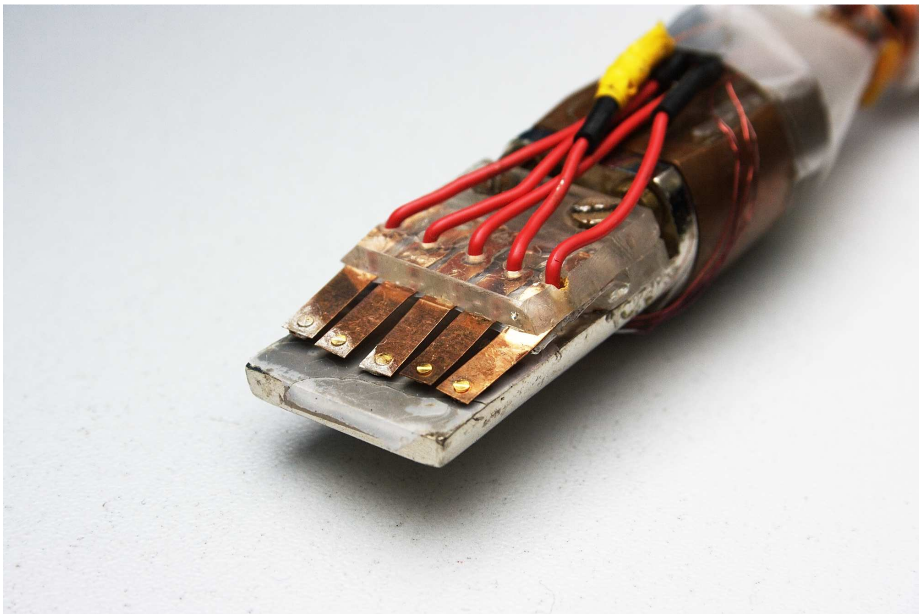

Figure 10.7: Photo of the new sampleholder used in our experiments (without a sample).

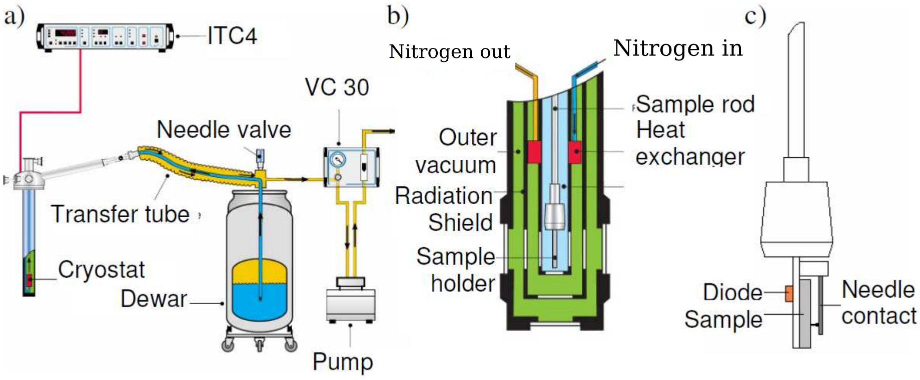

Figure 10.8: (a) overview of the cryostatic setup. (b) Cross section of the sample space in the cryostat. (c) Sample holder. Drawing made by G. Slanitsch.[55]

possible with simple shadow masks.

The temperature of the ground plate (to which the lower side of the substrate is attached) was measured with a Lakeshore Cryotronics Inc. DT-670-SD diode which was operated with a constant current of 10 mA. The resulting voltage drop on the diode corresponded to the temperature and was measured with a multimeter. Additionally, the ITC4 temperature controller was used to monitor the heat exchanger temperature and to regulate electric heating for more stability while electric curves were recorded at some constant temperature.

In our measurements we were able to cool down to 80 K and to do electrical characterisation at discrete temperature steps. It is also possible to heat the sample to above room temperature, but care must be taken not to damage the sealings of the cryostat windows, which were made from indium that has a low melting temperature of 156 °C. Heating after cryostatic experiments was not done in our case, because the electric contact was lost while the samples were warmed-up to room temperature.

10.2.2 Heat stage

Independent of the cryostat setup, a separate heat stage was used in the experiments. The DHS 900 from Anton Paar company (Fig. 10.9) was originally designed for use in X-ray diffractometers. It can heat precisely to a selected temperature up to 900 °C. The heat stage was used inside a glove box with feed through lines to the control unit which was located outside the chamber. It has a compact design and is accessible to our MDL positioners. The sample could be heated up to 200 °C and electrical characterisation could be made in situ.

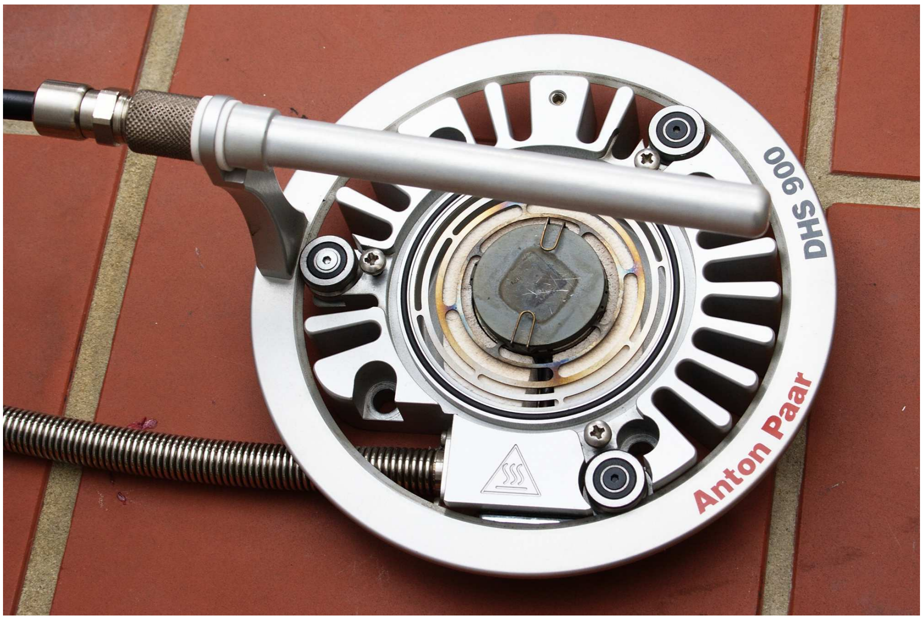

Figure 10.9: DHS 900 heat stage from Anton Paar company used for heating experiments in the glovebox.

10.2.3 Mobility extraction

P3HT charge carrier mobilities were extracted from the transfer curves of the devices. Transfer curves were recorded by applying constant drain source voltage, and sweeping the gate voltage. In our case V_{DS} was usually held at $V_{DS} = -20\,\mathrm{V}$ and V_G was sweeped from $60\,\mathrm{V}$ to $-80\,\mathrm{V}$ (down sweep) and then back to $60\,\mathrm{V}$ (up sweep). Simultaneously, I_D was recorded as a function of V_G. The mobility μ and zero voltage V_0 were extracted in linear and saturation regime for both sweeps.

In linear regime equation (4.6) was employed with fitting parameters μ and V_0 taking data points measured at low gate voltages $V_G < -2V_{DS}$. In saturation regime using equation (4.13) the fit is done in the region between $V_G = V_0$ and $V_G = V_0 - |V_{DS}|$. In our measurements, V_0 was not necessarilly at zero volt, so finding the best saturation range $V_G = [V_0, V_0 - |V_{DS}|]$ was not trivial. To solve this problem we wrote a algorithm, which should be presented here: In every possible saturation range a *fitting window* is defined by

$$V_{range}(n) = [V_0(n) \cdots V_0(n) - |V_{DS}|]. \tag{10.1}$$

For every fitting window n the mobility $\mu(n)$ is calculated from fitting the measured I_D by

$$\sqrt{I_D(V_G)} = a_1 V_G + a_2 \qquad V_0(n) - |V_{DS}| < V_G < V_0(n), \tag{10.2}$$

where $a_1^2(n) \propto \mu(n)$ and $a_2(n)$ is the zero voltage extracted from the fit. Fits, where the “right side” of the parabola approximates the measured curve are discarded, since they are obviously incorrect[2]. The highest $\mu(n)$ and the associated zero voltage $a_2(n)$ are then selected as the true mobility in saturation regime μ and the true zero voltage in saturation regime V_0. The process is ilustrated in Fig. 10.10.

In both, the linear and saturation case, fitting was done in Matlab using the so called *polynomial fitting* with polynoms of degree 1 ($p(x) = a_0 + a_1 x$). Mobility was not calculated for every gate voltage point, since this would include the local derivatives of the transfer curve. The shapes of the curves varied from batch to batch and significant hysteresis were observed at room temperature. Thus calculating the gate voltage dependence of mobility would not be very meaningfull. Instead, the mobility was fitted at low (saturation regime) and high gate bias (linear regime) thus averaging local effects. From comparing these two mobilities, still some conclusions regarding the gate voltage dependence of μ can be drawn. An example for fitting the transfer curve is shown in Fig. 10.11.

The zero voltage can be deduced from the transfer curve by many methods. A review on zero voltage extraction is given by Ortiz-Code et al.[40] In our analyses we stuck to equations (4.6) and (4.13) in order to stay consistent.

---

[2] In the cases, where the “right side” of the parabola approximates the measured curve the extracted zero voltage a_2 lies in the left half of the fitting window. By comparing a_2 to the limits of the fitting window, these cases can be identified.

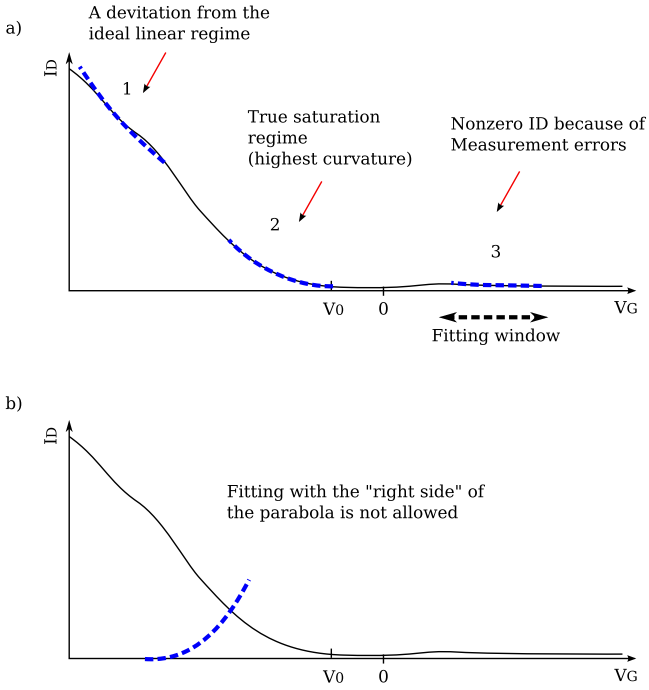

Figure 10.10: **a)** Here a hypothetical transfer curve is shown in order to illustrate the fitting process in the saturation regime. As an example three possible *fitting windows* are drawn. Every fit window has the width equal to $|V_{DS}|$, but is located at a different position on the V_G-axis. In every such window a fit according to equation (10.2) is done. The curvatures (which increase with the mobility) of the fits in the window 1 and in the window 3 are lower than in fit within the window 2. Therefore the fit in window 2 has the highest mobility. **b)** In some cases the fitting yields a result, where the “right side” of the parabola approximates the measured curve within a fitting window. Those cases are discarded.

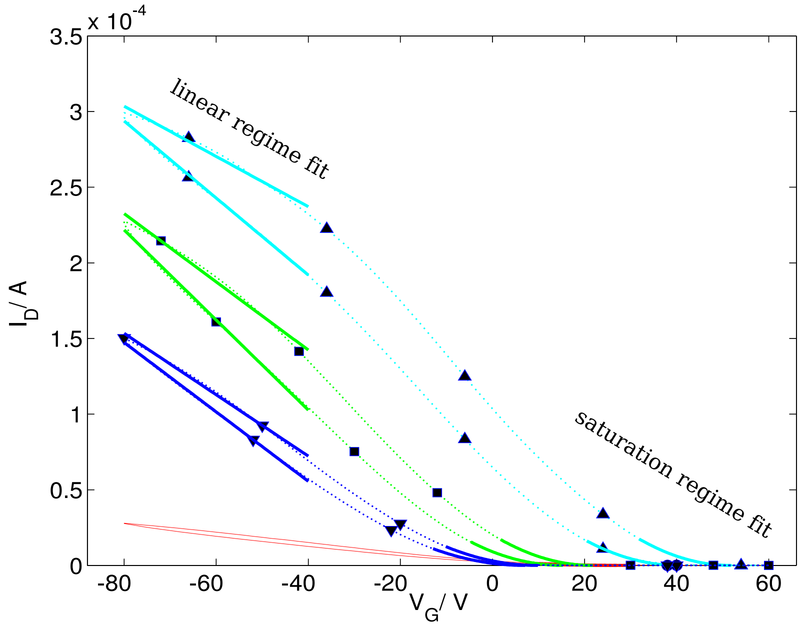

Figure 10.11: Example of fitting the transfer curve in linear and saturation regime. Thicker lines denote the fits. Fits in the linear regime are calculated for $V_G < 40\,\mathrm{V}$ and in the saturation regime for $V_0 - 20\,\mathrm{V} < V_G < V_0$.

10.2.4 Fits of mobilities to different charge transport models

To describe the temperature dependence of the mobility, the following fitting functions were used.

$$\mu = P_1 \exp\left(-P_2/T\right), \tag{10.3}$$

$$\mu = P_1 \exp\left(-P_2/T^2\right), \tag{10.4}$$

$$\mu = P_1 \exp\left(-P_2/T^{P_3}\right), \tag{10.5}$$

The P_x-values are the fitting parameters and μ and T were measured data. These non-linear fits were done with the Levenberg Marquard algorithm programmed in Matlab and with a standard deviations for μ of 10%. This value was an educated guess, estimated from the spread of μ values for some fixed temperature. The standard devitations of the fit parameters P_x depended on this value and should not be taken as a hard fact. From P_2 in equation (10.3) the activation energy is calculated, from P_2 in (10.4) the width of the site-DOS σ. Equation (10.3) corresponds to low charge carrier density models such as those from Bässler et al. and (10.4) relates to high n models like multiple trapping and thermal release.

The last equation (10.5) is unique, since it does not correspond to a special theoretical charge transport model, but includes both (10.3) and (10.4). For $P_3 = 1$, equation (10.5) would be equal to (10.3) and in the case of $P_3 = 2$, the equation (10.5) would be equal to (10.4). Other values of P_3 simply show the deviation from the usual models.

For every cryostatic measurement series with a device (where mobilities were measured for different temperatures), all three fits were calculated and compared to each other. The temperature dependence of μ in (10.3) is different from (10.4). From the quality of the fits the appropriate class of charge transport models could be selected.

Chapter 11

Temperature dependend measurements

In the following, tree different P3HT-type materials are used in cryostatic experiments. The first P3HT sample is a co-polymer, the others were pure P3HT with different $\mathrm{M_W}$. Unfortunately, we had no information available on the synthesize routes of the two commercially produced pure P3HT polymers.

From the mobilities extracted at cryostatic temperatures conclusions can be made on transport models and on the activation energies. Furthermore, the dependence of the zero voltages and the hysteresis in the transfer plots on the temperature will be shown. The question is, if the different $\mathrm{M_W}$s will have an impact on these electric properties.

All devices were fabricated in argon atmosphere, initial electrical characterisations were also done in argon. After that, cryostatic examinations were performed, as explained in the previous chapter (page 85). Non-cryostatic experiments for specific P3HT species are also presented below. Extracted data is fitted to different models as explained before (page 90 and page 93).

11.1 Sigma Aldrich P3HT

11.1.1 Polymer properties

This P3HT sample (Fig. 11.1) was purchased from Sigma Aldrich Co. Weight average molecular weight is given as $M_w \approx 87000\,{}^{\mathrm{g}}\!/\!_{\mathrm{mol}}$, head to tail regioregularity is $\geq 98.5\%$. These values are published by Slanitsch.[55] Unfortunally we had no data sheet for this material and no information was available on the internet site of Sigma Aldrich Co. Polydispersivity was also not reported, but might have a high value as stated by Kline et al.[45]

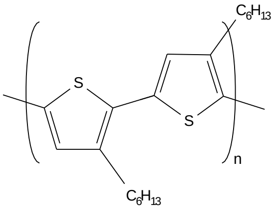

Figure 11.1: Chemical structure of head to tail regioregular P3HT.

11.1.2 Fabrication

Two substrates were oxygen etched and two were untreated before spincoating. Devices were prepared as usual (page 82). TCB was used as solvent. No significant differences in transistor characteristics were observed between etched substrates and those where the etching step omitted. The following analysis deals with devices (build on oxygen-etched substrates) whose fabrication is summarized in Tab. 11.1.

11.1.3 Mobilities

Mobilities were low when initially measured inside the glove box ($\mu \approx 2 \times 10^{-3}\,{}^{\mathrm{cm}^2}\!/\!_{\mathrm{Vs}}$), but rose by an order of magnitude ($\mu \approx 1.5 \times 10^{-2}\,{}^{\mathrm{cm}^2}\!/\!_{\mathrm{Vs}}$) after

Table 11.1: Production specifications for the device f240.

Fet 240	
Polymer	Sigma Aldrich P3HT, (discontinued)
Solvent	1,2,4-Trichlorobenzene, Aldrich, anhydrous, $\geq 99\%$
Substrate	Prime grade, $< 10\,\Omega/\mathrm{cm}$, 150 nmSiO_2
Plasma etching	100%, O_2 flow rate $8\,\mathrm{l/h}$, pressure: 0.2 mbar, duration: 30 s
Spincoating	1500 rpm, 40 s
Drying	2 h, 76 °C
Evacuation	duration 8 h, final pressure 8×10^{-6} mbar
Contact evaporation	Au, thickness: 50 nm, duration 600 s

exposing the devices to air for 30 min and than again measuring inside the glovebox (Fig. 11.2). No degradation occurred probably because the devices were kept in darkness or soft light when exposed to air.

In contrast to other investigated semiconducting polymers presented in the following sections, the zero voltage was far on the positive side ($V_0 \approx 50\,\mathrm{V}$) and the mobility was one order of magnitude higher. This could be attributed to doping and improved charge transport due to increased $\mathrm{M_W}$ respectively. After the measurements in the glove-box, the device was characterized inside the vacuum chamber of the cryostat. The chamber with the device was evacuated to 1.5×10^{-4} mbar and than flooded with helium. The mobility stayed at the same value ($\mu \approx 1.5 \times 10^{-2}\,\mathrm{cm^2/Vs}$) but the zero voltage shifted to lower values ($V_0 \approx 20\,\mathrm{V}$). The differences between transfer curves in the glovebox after air exposure and in helium (Fig. 11.2) could be explained by different amount of doping. Still the device performance was very good, the off-current stayed low ($I_D(V_G) \approx 1 \times 10^{-6}\,\mathrm{V}$) and the on-off-ratio was higher than 1000 as seen in Fig. 11.3.

Low temperature measurements were done down to temperatures $T = 85\,\mathrm{K}$. In figure 11.4 the mobilities μ_{lin} extracted in the *linear* regime of the transfer curves are plotted against $1/T$. There were some deviations from the Arrhenius fit (10.3) at temperatures above 250 K and below 100 K. From this fit, the mobility activation energy was found to be 78 meV. Using the mobilities extracted in the *saturation* regime μ_{sat} of the transfer curves a similar picture (Fig. 11.5) emerged; again there were some deviations from Arrhenius behaviour at high and low temperatures, but the activation energy was the same $E_a = 78\,\mathrm{meV}$.

The fit for low n models (like Bässler's model) showed a higher discrepancy. When plotting $log(\mu)$ over $1/T^2$ the data points should arrange in a line. This was clearly not the case for both, the mobility extracted from *linear* regime (Fig. 11.6) and the mobility extracted from *saturation* regime (Fig. 11.7). At least mathematically it would make more sense to partition the datapoints into 3 classes where 3 separate fits would be made, but this is beyond simple low n models. It also would be required to record far more datapoints to justify such a analysis.

The (mathematically) best fit was found when using equation (10.5) with an exponent $P_3 = 0.55$ for mobilities extracted in *linear* regime and $P_3 = 0.35$ for mobilities extracted in *saturation* regime. As can be seen in Fig. 11.8 and Fig. 11.9, even there were still some deviations at the outer parts of the curves.

Of the three types of temperature dependencies of the mobility, the most meaningfull fit was obtained using (10.3), which supported high n-models like multiple trapping and thermal release. As stated before (page 93) the fitting equation (10.5) was not derived from any model and is purely empirical. The results of the different fits are summarized in Tab. 11.2.

Table 11.2: Model Parameters up to their significant digit for the device fabricated as described in Tab. 11.1. Standard deviation of the mobilities is assumed to be 10%. Standard deviation of parameters for an arbitrary exponent could not be found in the saturation regime because of numerical difficulties. Standard deviations (which are calculated by the Levenberg Marquard algorithm) of the parameters for low and high n models were in the 0.01 meV and 0.05 meV range.

Model	T dependency	parameter in linear regime	parameter in saturation regime
high n models	$\mu \propto \exp\left(-\frac{E_a}{k_b T}\right)$	$E_a = 78.3\,\mathrm{meV}$	$E_a = 77.9\,\mathrm{meV}$
low n models	$\mu \propto \exp\left(-\frac{2}{3}\frac{\sigma}{k_b T}\right)^2$	$\sigma = 32.5\,\mathrm{meV}$	$\sigma = 31.6\,\mathrm{meV}$
Arbitrary exponent	$\mu \propto \exp\left(-\frac{E_a}{k_b T}\right)^n$	$E_a = 0.9 \pm 0.6\,\mathrm{eV},\ m = 0.55 \pm 0.05$	$E_a = 0.4\,\mathrm{eV},\ m = 0.34$

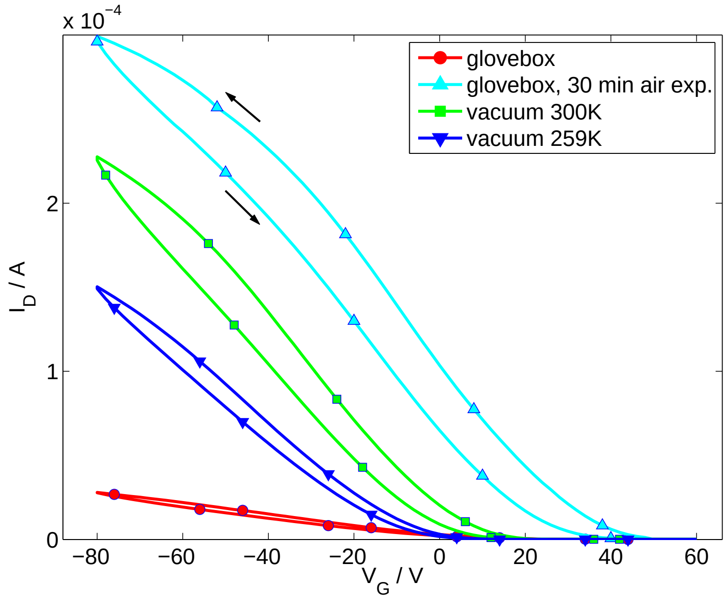

Figure 11.2: Linear plot of the transfer characteristics at different stages with $V_{DS} = -20\,\mathrm{V}$. The measurements were done **a)** in the glove box, directly after device fabrication, **b)** in the glovebox, after the device was exposed to ambient air for 30 min, **c)** inside the cryostat in helium at 300 K and **d)** at 259 K. Device fabrication Tab. 11.1.

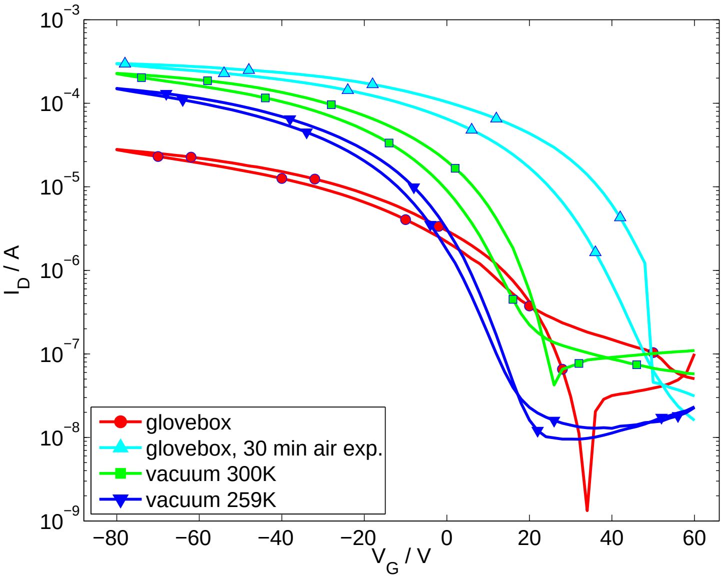

Figure 11.3: Logarithmic plot of the transfer characteristics at different stages with $V_{DS} = -20\,\mathrm{V}$. The measurements were done **a)** in the glove box, directly after device fabrication, **b)** in the glovebox, after the device was exposed to ambient air for 30 min, **c)** inside the cryostat in helium at 300 K and **d)** at 259 K. Device fabrication Tab. 11.1.

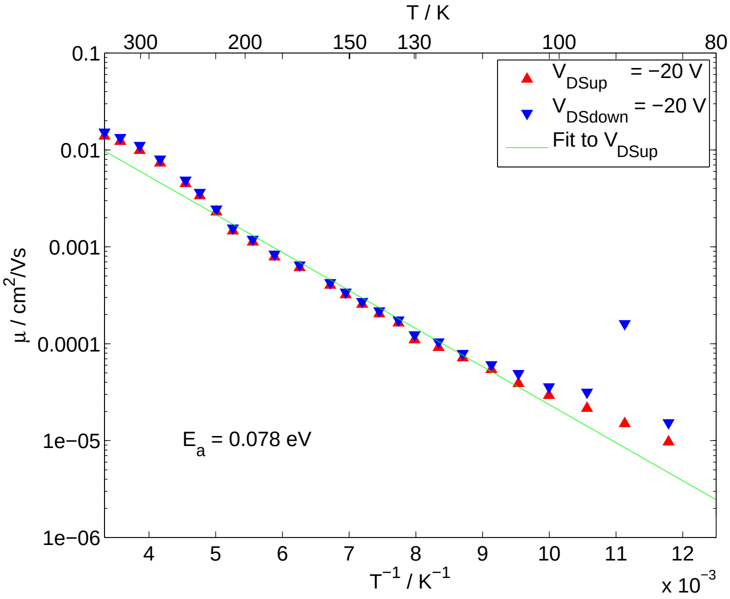

Figure 11.4: Mobility vs. Temperature in *saturation* regime for $\mu \propto \exp\left(-\frac{E_a}{k_b T}\right)$. Both, mobilities extracted at the down sweep (▼-symbols) and the up-sweep (▲-symbols) of the transfer curves are shown. The equation is fitted to up slope mobilities at $V_{DS} = -20\,\mathrm{V}$. Device fabrication Tab. 11.1.

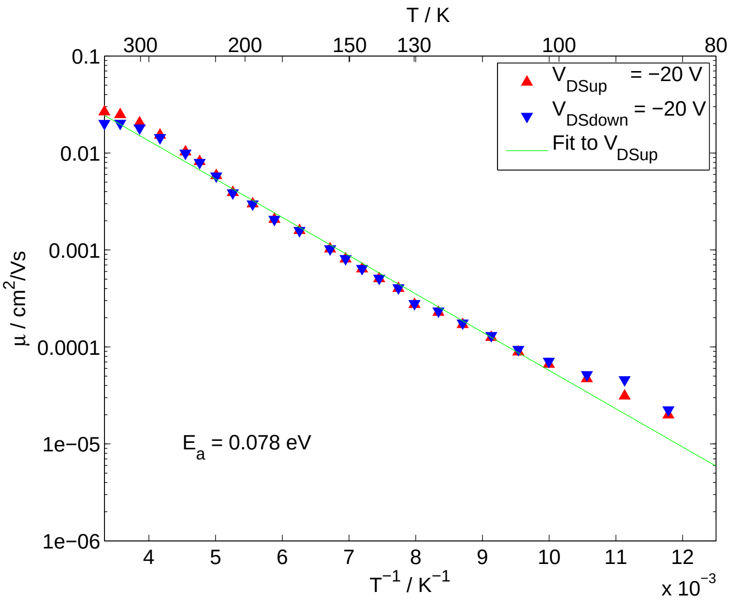

Figure 11.5: Mobility vs. Temperature in *linear* regime for $\mu \propto \exp\left(-\frac{E_a}{k_b T}\right)$. Both, mobilities extracted at the down sweep (▼-symbols) and the up-sweep (▲-symbols) of the transfer curves are shown. The equation is fitted to up slope mobilities at $V_{DS} = -20\,\mathrm{V}$. Device fabrication Tab. 11.1.

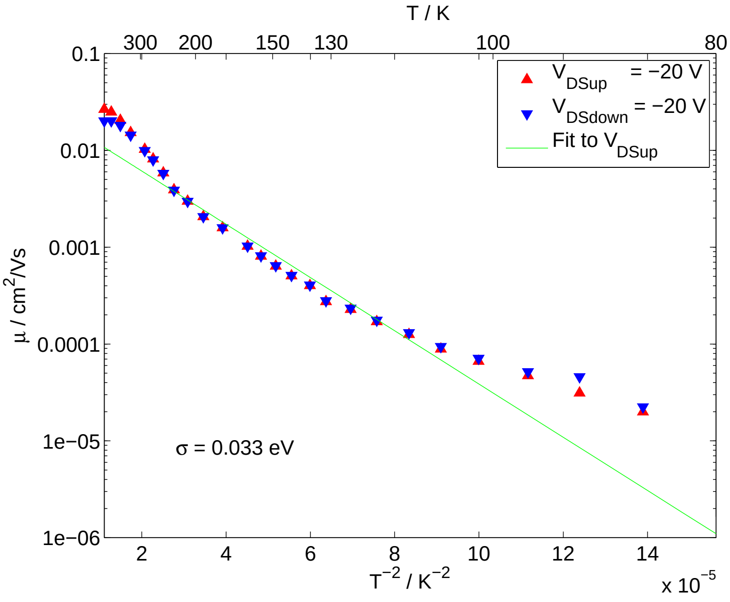

Figure 11.6: Mobility vs. Temperature in *linear* regime for $\mu \propto \exp\left(-\frac{2}{3}\frac{\sigma}{k_b T}\right)^2$. Both, mobilities extracted at the down sweep (▼-symbols) and the up-sweep (▲-symbols) of the transfer curves are shown. The equation is fitted to up slope mobilities at $V_{DS} = -20\,\mathrm{V}$. Device fabrication Tab. 11.1.

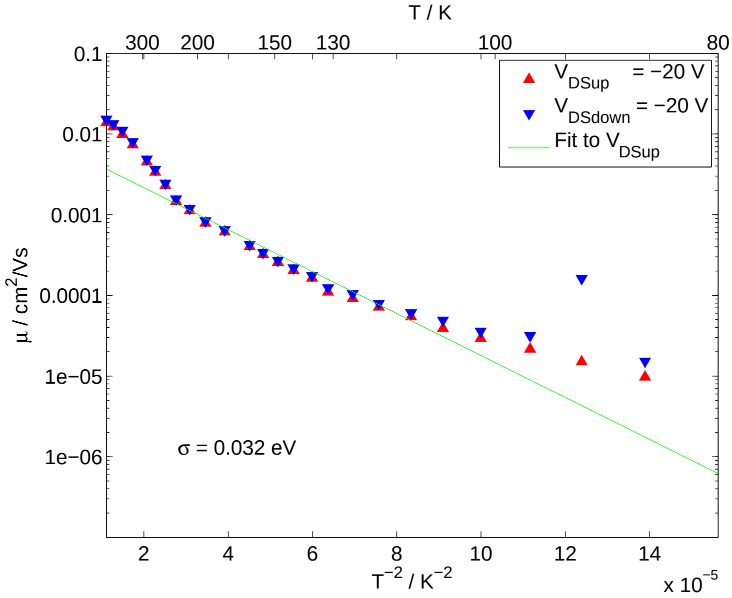

Figure 11.7: Mobility vs. Temperature in *saturation* regime for $\mu \propto \exp\left(-\frac{2}{3}\frac{\sigma}{k_b T}\right)^2$. Both, mobilities extracted at the down sweep (▼-symbols) and the up-sweep (▲-symbols) of the transfer curves are shown. The equation is fitted to up slope mobilities at $V_{DS} = -20\,\mathrm{V}$. Device fabrication Tab. 11.1.

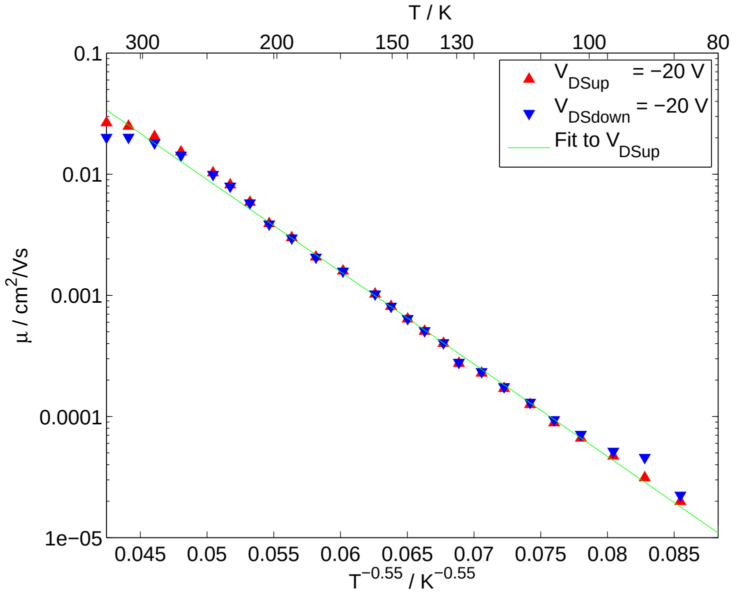

Figure 11.8: Mobility vs. Temperature for $\mu \propto \exp\left(-\frac{E_a}{k_b T}\right)^n$. The best fit was found with the exponent $n = 0.55$. Both, mobilities extracted at the down sweep (▼-symbols) and the up-sweep (▲-symbols) of the transfer curves are shown. The equation is fitted to up slope mobilities in *linear* regime at $V_{DS} = -20\,\mathrm{V}$. Device fabrication Tab. 11.1.

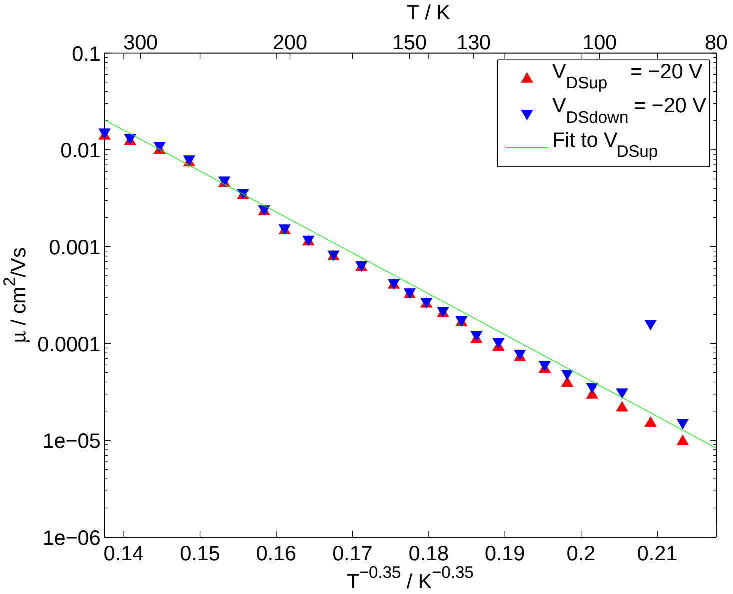

Figure 11.9: Mobility vs. Temperature for $\mu \propto \exp\left(-\frac{E_a}{k_b T}\right)^n$. The best fit was found with the exponent $n = 0.35$. Both, mobilities extracted at the down sweep (▼-symbols) and the up-sweep (▲-symbols) of the transfer curves are shown. The equation is fitted to up slope mobilities in *saturation* regime at $V_{DS} = -20\,\mathrm{V}$. Device fabrication Tab. 11.1.

11.1.4 Zero voltage and hysteresis

The zero voltages become negative at lower temperatures. At room temperature their value $V_0 \approx 20\,\mathrm{V}$ was significantly higher than at ($T = 200\,\mathrm{K}$), where $V_0 \approx 0\,\mathrm{V}$. With further decreasing temperature they became even more negative reaching $V_0 \approx -20\,\mathrm{V}$ at $T = 100\,\mathrm{K}$. This effect is best seen in the plot of the zero voltage extracted in *saturation* regime (Fig. 11.10). The observed temperature dependence could be an effect of deep charge carrier traps, that have to be filled up by charge carriers and whose energies are so low, that at low temperatures thermally activated release becomes unlikely.

Note that both zero voltages, extracted from the up-slope and from the down-slope of the transfer curve, were taken into account. Because of the hysteresis effects, they did not match exactly. As seen in Fig. 11.10 the down-slope zero voltages $V_0 \Downarrow$ were higher than the up-slope zero voltages $V_0 \Uparrow$ at room temperature. With decreasing temperature, the voltage difference decreased and at $T = 200\,\mathrm{K}$ there was hardly any distinction between the two zero voltages. At temperatures lower than $T = 150\,\mathrm{K}$ the situation changed; now $V_0 \Downarrow$ became lower than $V_0 \Uparrow$. This was also seen in zero voltages extracted in the *linear* regime, but the plot (Fig. 11.11) should be taken cum grano salis: since the data points used for fitting in linear regime ($V_G = -80\,\mathrm{V} \cdots - 40\,\mathrm{V}$) were far away from the zero voltage, they were of less reliability.

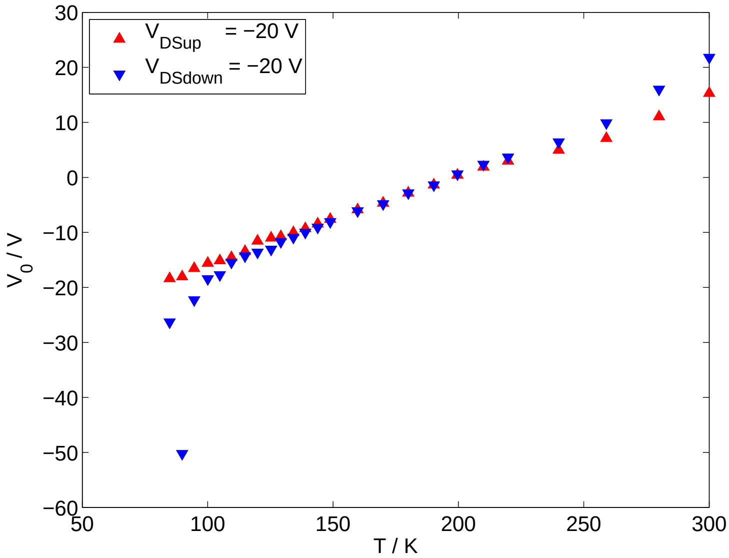

Figure 11.10: Zero voltage (for down and up-slope of V_G) vs. Temperature, extracted in saturation regime. Device fabrication Tab. 11.1.

Three selected transfer curves for different temperatures are compared in Fig. 11.12 (with normalyzed scale) and in Fig. 11.13 (in logarithmic scale). As discussed abobe, an overall shift towards more negative gate voltages and a reduction of the hysteresis upon cooling is clearly seen there.

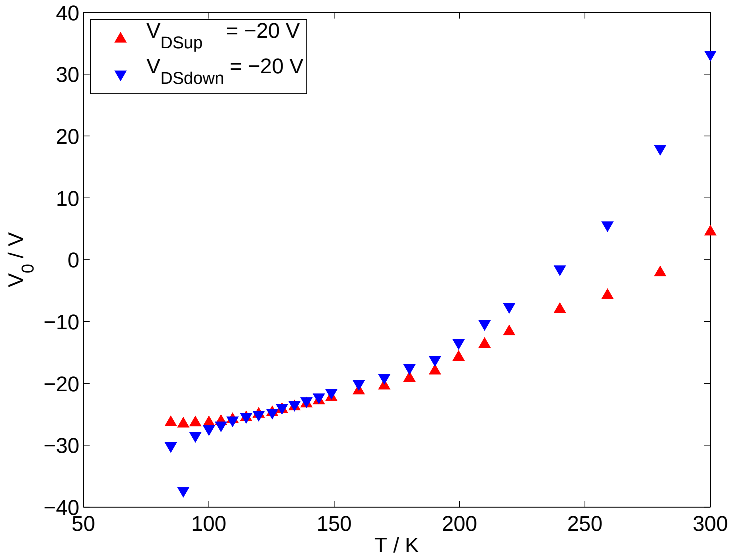

Figure 11.11: Zero voltage (for down and up-slope of V_G) vs. Temperature, extracted in linear regime. These values are not as accurate as those from saturation regime (Fig. 11.10). Device fabrication Tab. 11.1.

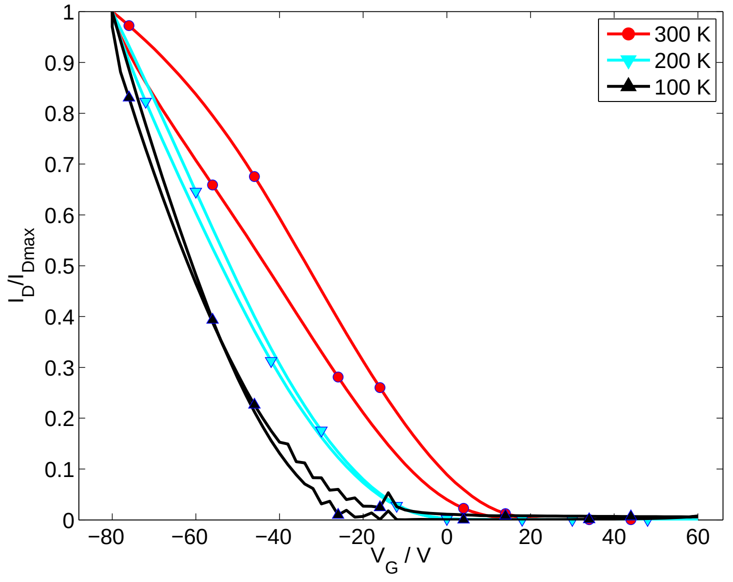

Figure 11.12: Transfer characteristics at different temperatures (300 K, 200 K and 100 K), in the cryostat in helium atmosphere. The three measurement data-series are normalized to one, in order to be comparable. Device fabrication Tab. 11.1.

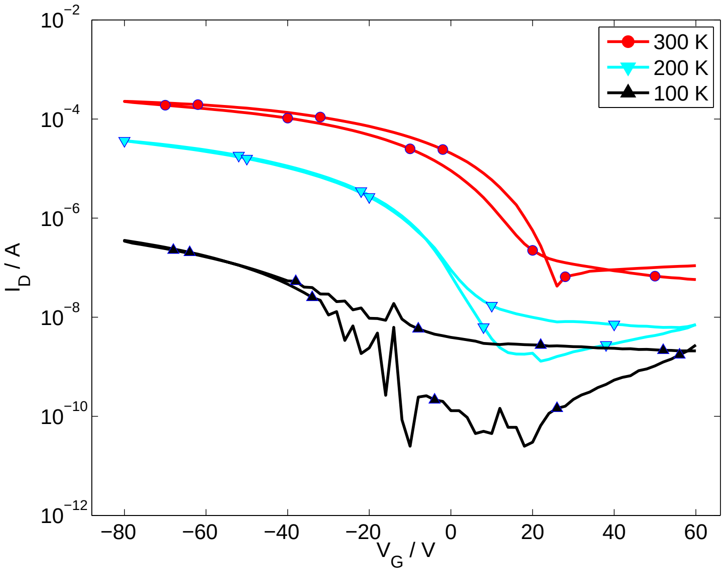

Figure 11.13: Transfer characteristics at different temperatures(300 K, 200 K and 100 K), in the cryostat in helium atmosphere. Device fabrication Tab. 11.1.

Interestingly, the transfer curve hysteresis also followed the empirical

$$A^{hysteresis} \propto \exp\left(-\frac{E_a^{hysteresis}}{k_b T}\right) \tag{11.1}$$

law where $A^{hysteresis}$ is the area between the down-slope and the up-slope transfer curves. The hysteresis activation energy was fitted in an Arrhenius plot $E_a^{hysteresis} = 170\,\text{meV}$ (Fig. 11.14). The origin of the hysteresis could be quasi-immobile charges (possibly ionic impurities) that slowly accumulated at the insulator-semiconductor interface and did not contribute to the conductivity. At low temperatures, the speed of their accumulation was reduced, so we conclude that their drift is thermally activated. This idea is supported by Mathijsen et al.[33] From their data they saw a zero voltage shift in the direction of applied gate bias stress. With SKPM they also measured additional charge in the channel that did not contribute to the I_D current, but which nevertheless had to be be included in the electrostatic calculations (with no doping, and therefore with $V_0 \approx 0$):

$$Q_{tot}(V_G) = Q_{mobile}(V_G) + Q_{immobile}(V_G) \propto -C_i V_G \tag{11.2}$$

where Q_{tot} is the total charge in the accumulation layer, which can be divided into (1) fast mobile Q_{mobile} charge and (2) slow quasi-immobile $Q_{immobile}$ charge. When applying a negative V_G to a device with an accumulation layer that was previously in equilibrium, at first fast mobile charge is accumulated in the channel leading to high current $I_D \propto Q_{mobile} V_{DS}$. Then slow quasi-immobile ionic impurities accumulate at the insulator-semiconductor interface and compensate for some V_G and thus reduce Q_{mobile} and, subsequently, decrease I_D. This model can be translated to a model with a change in the zero voltage:

$$Q_{mobile}(V_G) \propto -C_i(V_G - V_{0ions}(V_G)), \tag{11.3}$$

with

$$V_{0ions}(V_G) = \frac{Q_{immobile}(V_G)}{C_i}. \tag{11.4}$$

When a positive V_G is applied, V_{0ions} increases with time, as the slow impurities drift toward the insulator-semiconductor interface. On the other hand, a negative V_G decreases V_{0ions}.

In our measurements, we started with positive V_G so the initial zero voltage V_0 was more positive. Further on V_G was decreased down into negative range and the transfer curve in the down slope was recorded. Immediately after that, the up-slope curve was obtained, where V_G started at negative voltage and increased to the positive side. The V_0 was therefore shifted to the negative direction. This shifts can be seen in Fig. 11.10 where both, the up-slope V_0 and down-slope V_0 are plotted against temperature.

Alltogether this effect could lead to a hysteresis in the transfer curve, at least at temperatures higher than $T = 150\,\mathrm{K}$. As stated above, at temperatures lower than $T = 150\,\mathrm{K}$ the situation changed: $V_0 \Downarrow$ become lower than $V_0 \Uparrow$ and the hysteresis become "inverted". This can not be explained by the ionic impurities model.

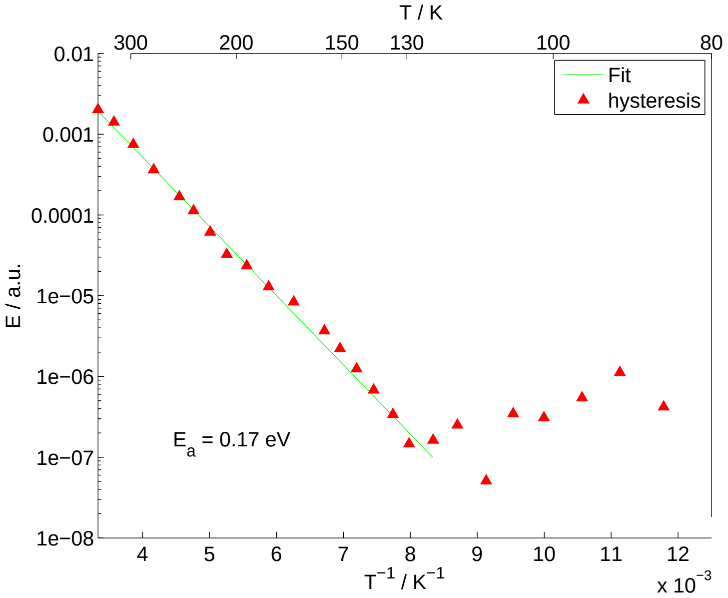

Figure 11.14: Hysteresis of the transfer curves vs. Temperature. Fit was done according to $A^{hysteresis} \propto \exp\left(-\frac{E_a^{hysteresis}}{k_b T}\right)$. The hysteresis was obtained from transfer curves at $V_{DS} = -20\,\mathrm{V}$. Device fabrication Tab. 11.1.

11.2 Plexcore OS 1100 P3HT

11.2.1 Polymer properties

Plexcore OS 1100 is a brand name for commercially available P3HT manufactured by the Plextronics company (CAS: 104934-50-1). The data sheet, which was sent together with the material, gives the following information: number average molecular weight $M_n = 25000\,{}^{\mathrm{g}}/_{\mathrm{mol}}$, Polydiversity $PDI = 2.0$, regioregularity is 95 % head to tail and a metal content of < 50 ppm.

11.2.2 Fabrication

The devices were fabricated the usual way in argon atmosphere. The substrate was handled with plastic tweezers in this case. A 10 day old Plextronix P3HT 2 $^{\mathrm{g}}/_{\mathrm{l}}$ solution in TCB was used for spincoating. After spin coating the substrate was left on the spin coater to dry up for approximately 15 minutes. In the next step, it was annealed at 75 °C for 150 minutes. The evaporating vessel with the substrate inside was evacuated for 21 hours. Then 5×10^{-6} mbar pressure were reached and the gold contacts were deposited. The gold evaporation duration time was 7 minutes, the thickness of the gold layer was 50 nm so the deposition rate was 0.12 $^{\mathrm{nm}}/_{\mathrm{s}}$. A summery is given in Tab. 11.3. Two devices, designated as *1R* and *1L*, were made on the same substrate. So the fabrication steps of 1R and 1L were exactly the same. Both devices were than investigated simultaniously.

Table 11.3: Production specifications for the device f228.

Fet 228	
Polymer	Plexcore OS 1100
Solvent	1,2,4-Trichlorobenzene, Aldrich, anhydrous, $\geq$ 99%
Substrate	Prime grade, $< 10\,{}^{\Omega}/_{\mathrm{cm}}$, 150 nm$SiO_2$
Plasma etching	no plasma etching
Spincoating	1500 rpm, 40 s
Drying	220 min, 75 °C
Evacuation	overnight, final pressure 5×10^{-6} mbar
Contact evaporation	Au, thickness: 50 nm, duration 420 sec

11.2.3 Mobilities

Transfer characteristics in argon and in ambient air and darkness were obtained. As in the case of Sigma Aldrich P3HT, mobilities were low when directly after fabrication measured inside the glovebox ($\mu \approx 1 \times 10^{-4}\,{}^{\mathrm{cm}^2}/_{\mathrm{Vs}}$), but rose after air exposure; $\mu \approx 1 \times 10^{-3}\,{}^{\mathrm{cm}^2}/_{\mathrm{Vs}}$ was measured in ambient atmosphere. Inside the cryostat, at vacuum conditions (2.5×10^{-4} mbar), mobilities did not significantly differ from those measured in air, but the zero voltage shifted in negative direction (from 10 V to 0 V). After the whole cryogenic measurement series, the substrate was again characterised inside the glovebox. The devices showed the same relatively high mobility, as in ambient air and vacuum. These trends can be seen from transfer curves measured at the different device conditions in Fig. 11.15.

The off-currents were of the same order of magnitude ($I_D(V_G = 40\,\text{V}) \approx 5 \times 10^{-8}\,\text{A}$) as those of the Sigma Aldrich device. The on-off ratio was 200, as seen in the logarithmic plot of the transfer curves (Fig. 11.16). This value is lower than the on-off ratio of the Sigma Aldrich device.

Cryogenic measurements were made down to 100K. Below that temperature, the drain current was to low for meaningfull transfer curves. Three transfer curves at cryostatic temperatures are shown in Fig.11.17. As can be seen here, the shape of the curves does not change much in the logarithmic plot, but the accuracy of measurement decreases drastically below 130 K.

In the following, plots are presented according to different charge transport models:
Arrhenius type fits are done, to extract the activation energies for the high n models. Arrhenius plots for mobilities extracted in *saturation* regime are shown in Fig. 11.18 for the 1R device and in Fig. 11.19 for the 1L device. In both cases, the measured data points followed the Arrhenius behaviour, with the exception of mobilities measured at temperatures lower than 130 K. Those data points at low temperatures show a deviations to slightly higher values. Since the currents are very low at this temperatures ($max(I_D) < 10\,\text{nA}$), the deviations could simply be caused by measurement inaccuracies.

There are less deviations in Arrhenius temperature dependence of the mobilities extracted from the *linear* regime, as shown in Fig. 11.20 for the 1R device and in Fig. 11.21 for the 1L device. This can be expected, since the currents are higher in the linear regime, than in the saturation regime part of the transfer curves, thus causing less measurement inaccuracies. The activation energies extracted from these fits were between $E_a = 120\,\text{eV} \cdots 134\,\text{eV}$.

For low charge carrier density n models, the mobilities were plotted against $1/T^2$ in logarithmic scale. All these fits in these plots show a high deviation from the $1/T^2$ dependence of the mobilities. In all cases, for both devices and for mobilities extracted from the linear regime and from the saturation regime, the fits had bad quality. Mobilities extracted from *saturation* regime are plotted in Fig. 11.22 and Fig. 11.23; mobilities extracted from *linear* regime are plotted in Fig. 11.24 and Fig. 11.25.

Fits with arbitrary exponent according to equation (10.5) were also done for all four mobility data series. With the additional degree of freedom in the exponent, the best fits could be obtained. In three cases (Fig. 11.26, Fig. 11.27 and Fig. 11.28) the exponent n was close to zero ($n = 0.8 \cdots 0.94$). So the mobilities had almost Arrhenius temperature dependence. The mobilities in saturation regime of device 1L yielded an exponent $n = 0.51$ (Fig.11.19). In the associated Arrhenius plot (Fig. 11.19) the mobilities had also the highest deviation from the fit.

In conclusion, the mobilities can apparently be described by Arrhenius-type fits. As in the case of Sigma Aldrich P3HT, the charge carrier transport models are therefore of the high charge carrier density n type. Note, that the interpretation must be taken with care, because the temperature range in which useful currents could be measured for the Plexcore material was limited. With fewer data points measured at low temperatures (in comparison to measurements with the device made from Sigma Aldrich P3HT), there are fewer proofs to validate the choosing of a model. A summery of all fit parameters is given in Tab. 11.4.

Table 11.4: Model Parameters up to their significant digit for device fabricated as described in Tab. 11.5. Standard deviation (which are calculated by the Levenberg Marquard algorithm) of the mobilities is assumed to be 10%. Standard deviation of parameters for low and high n models were in the 0.01 meV and 0.05 meV respectively.

		Device 1R	
Model	T dependency	parameter in linear regime	parameter in saturation regime
high n models	$\mu \propto \exp\left(-\frac{E_a}{k_b T}\right)$	$E_a = 131\,\text{meV}$	$E_a = 134\,\text{meV}$
low n models	$\mu \propto \exp\left(-\frac{2}{3}\frac{\sigma}{k_b T}\right)^2$	$\sigma = 45\,\text{meV}$	$\sigma = 49\,\text{meV}$
Arbitrary exponent	$\mu \propto \exp\left(-\frac{E_a}{k_b T}\right)^n$	$E_a = 0.14 \pm 0.03\,\text{eV}$, $n = 0.94. \pm 0.07$	$E_a = 0.2 \pm 0.1\,\text{eV}$, $n = 0.8 \pm 0.1$
		Device 1L	
Model	T dependency	parameter in linear regime	parameter in saturation regime
high n models	$\mu \propto \exp\left(-\frac{E_a}{k_b T}\right)$	$E_a = 120\,\text{meV}$	$E_a = 132\,\text{meV}$
low n models	$\mu \propto \exp\left(-\frac{2}{3}\frac{\sigma}{k_b T}\right)^2$	$\sigma = 45\,\text{meV}$	$\sigma = 48\,\text{meV}$
Arbitrary exponent	$\mu \propto \exp\left(-\frac{E_a}{k_b T}\right)^n$	$E_a = 0.17 \pm 0.06\,\text{eV}$, $n = 0.89. \pm 0.08$	$E_a = 4 \pm 5\,\text{eV}$, $n = 0.51 \pm 0.08$

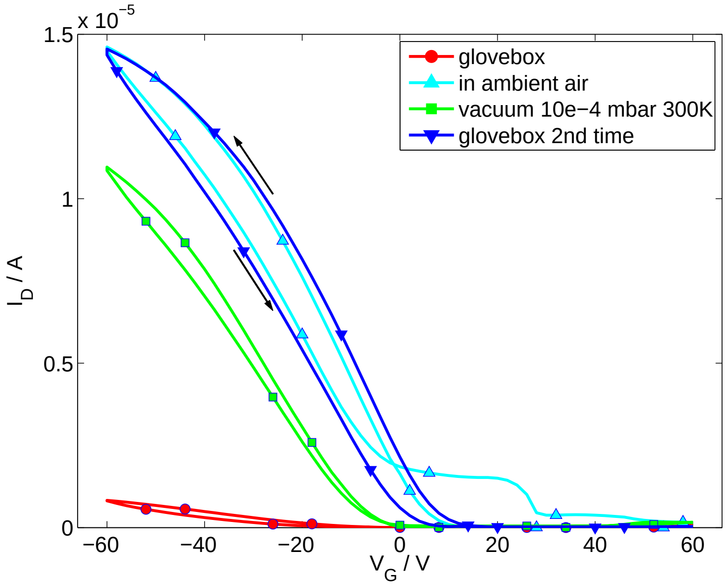

Figure 11.15: Plot of the transfer Curves of the 1L device acquired in different enviroments: **a)** in the glove box, directly after device fabrication, **b)** in ambient atmosphere in darkness (The origin of the plateau between $V_G = 0\,\text{V} \cdots 20\,\text{V}$ is unknown. It was not reproducable.), **c)** inside the cryostat chamber in vacuum conditions and **d)** in the glovebox, after all cryostatic measurements were done. All transfer curves were recorded with $V_{DS} = -20\,\text{V}$. Device fabrication: Tab. 11.3.

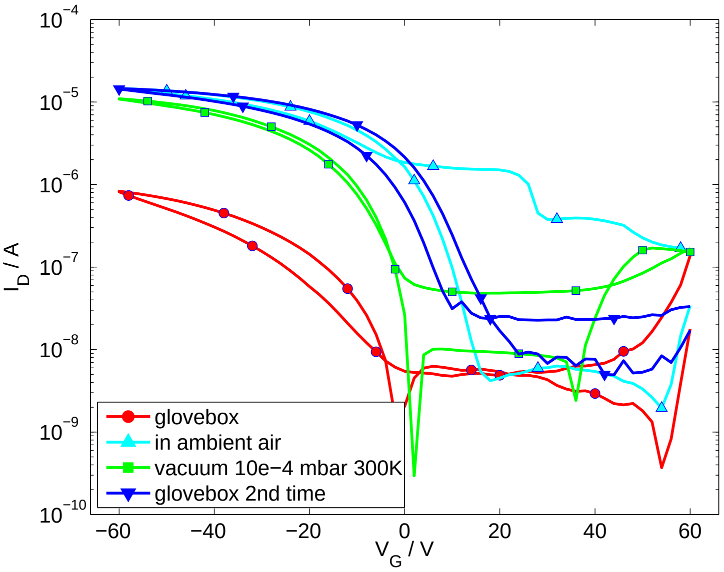

Figure 11.16: Logarithmic plot of the transfer Curves of the 1L device acquired in different enviroments: **a)** in the glove box, directly after device fabrication, **b)** in ambient atmosphere in darkness (The origin of the plateau between $V_G = 0\,\mathrm{V} \cdots 20\,\mathrm{V}$ is unknown. It was not reproducable.), **c)** inside the cryostat chamber in vacuum conditions and **d)** in the glovebox, after all cryostatic measurements were done. All transfer curves were recorded with $V_{DS} = -20\,\mathrm{V}$. Device fabrication: Tab. 11.3.

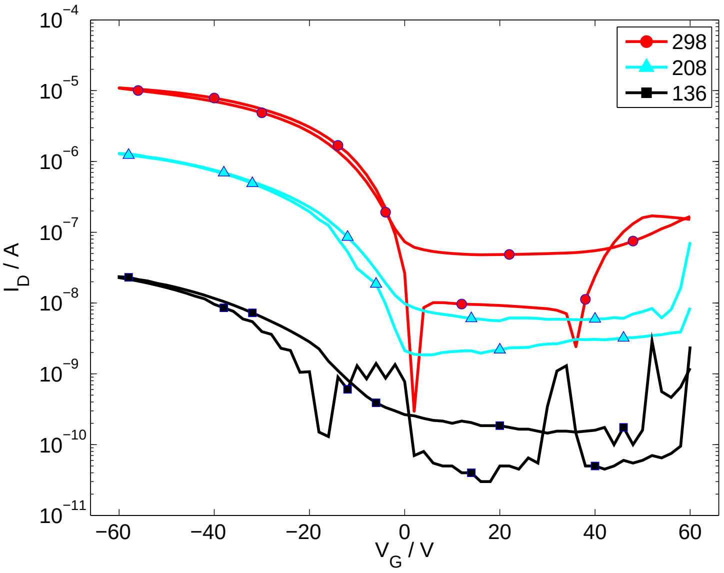

Figure 11.17: Logarithmic plot of the transfer curves of the 1L device at different temperatures (298 K, 208 K and 136 K) with $V_{DS} = -20\,\mathrm{V}$. Device fabrication: Tab. 11.3.

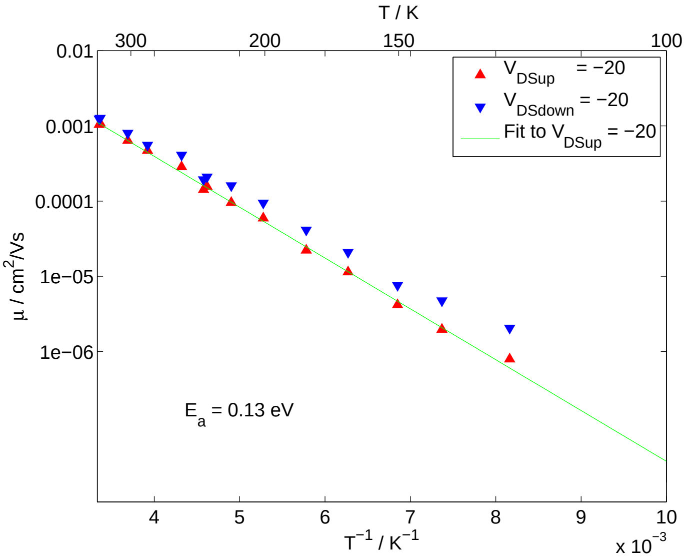

Figure 11.18: Plot of the mobility vs. Temperature in *saturation* regime for $\mu \propto \exp\left(-\frac{E_a}{k_b T}\right)$ for the device 1R. Both, mobilities extracted at the down sweep (▼-symbols) and the up-sweep (▲-symbols) of the transfer curves are shown. The equation is fitted to up slope mobilities at $V_{DS} = -20\,\mathrm{V}$. Device fabrication: Tab. 11.3.

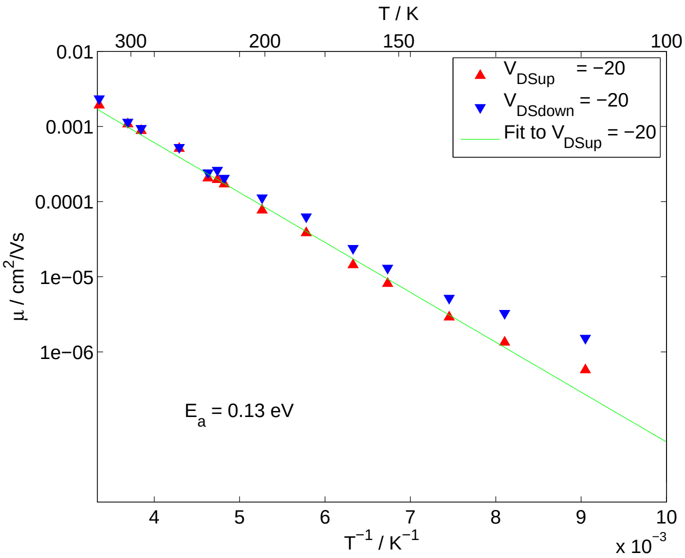

Figure 11.19: Plot of the mobility vs. Temperature in *saturation* regime for $\mu \propto \exp\left(-\frac{E_a}{k_b T}\right)$ for the device 1L. Both, mobilities extracted at the down sweep (▼-symbols) and the up-sweep (▲-symbols) of the transfer curves are shown. The equation is fitted to up slope mobilities at $V_{DS} = -20\,\mathrm{V}$. Device fabrication: Tab. 11.3.

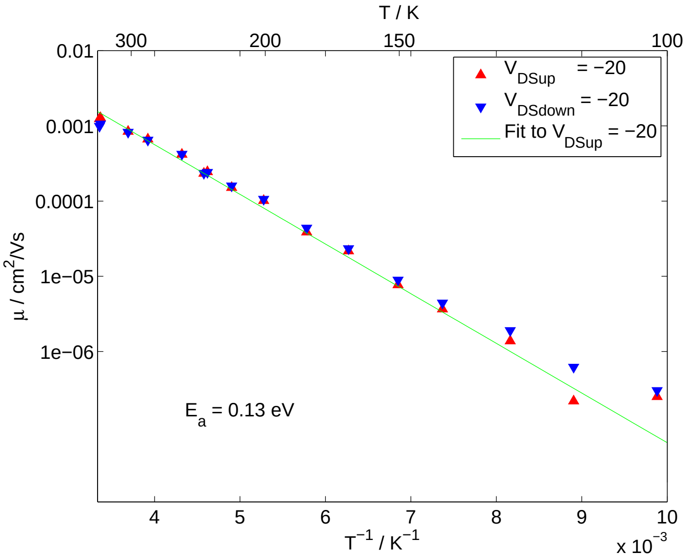

Figure 11.20: Plot of the mobility vs. Temperature in *linear* regime for $\mu \propto \exp\left(-\frac{E_a}{k_b T}\right)$ for the device 1R. Both, mobilities extracted at the down sweep (▼-symbols) and the up-sweep (▲-symbols) of the transfer curves are shown. The equation is fitted to up slope mobilities at $V_{DS} = -20\,\mathrm{V}$. Device fabrication: Tab. 11.3.

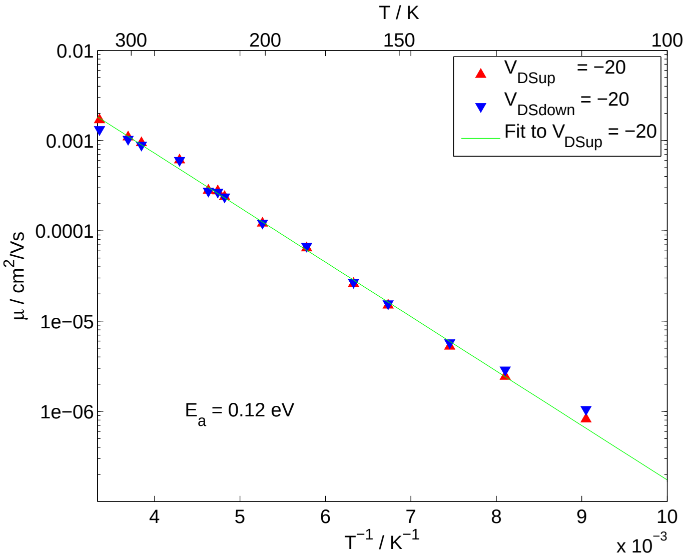

Figure 11.21: Plot of the mobility vs. Temperature in *linear* regime for $\mu \propto \exp\left(-\frac{E_a}{k_b T}\right)$ for the device 1L. Both, mobilities extracted at the down sweep (▼-symbols) and the up-sweep (▲-symbols) of the transfer curves are shown. The equation is fitted to up slope mobilities at $V_{DS} = -20\,\mathrm{V}$. Device fabrication: Tab. 11.3.

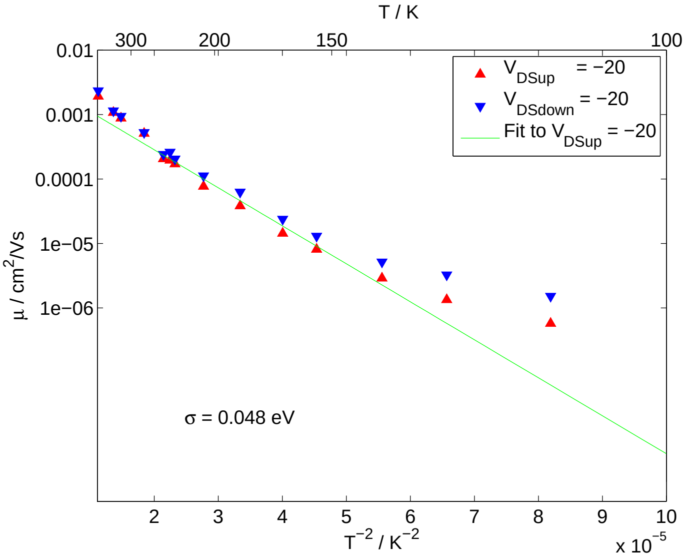

Figure 11.22: Plot of the mobility vs. Temperature in *saturation* regime for $\mu \propto \exp\left(-\frac{2}{3}\frac{\sigma}{k_b T}\right)^2$ for the device 1L. Both, mobilities extracted at the down sweep (▼-symbols) and the up-sweep (▲-symbols) of the transfer curves are shown. The equation is fitted to up slope mobilities at $V_{DS} = -20\,\mathrm{V}$. Device fabrication: Tab. 11.3.

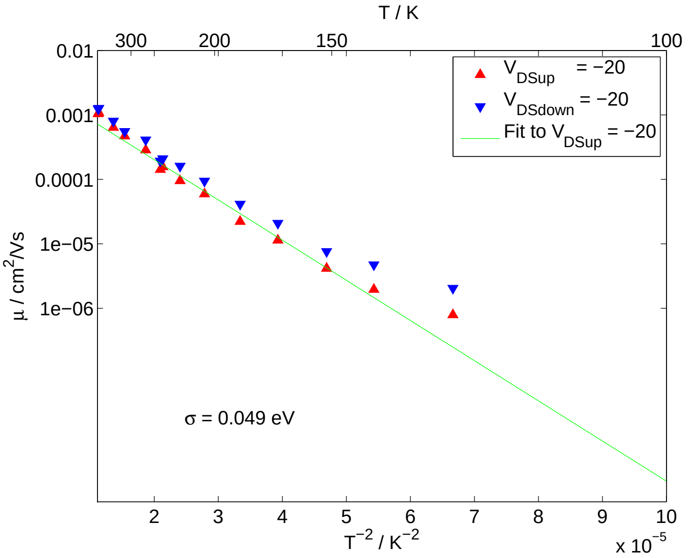

Figure 11.23: Plot of the mobility vs. Temperature in *saturation* regime for $\mu \propto \exp\left(-\frac{2}{3}\frac{\sigma}{k_b T}\right)^2$ for the device 1R. Both, mobilities extracted at the down sweep (▼-symbols) and the up-sweep (▲-symbols) of the transfer curves are shown. The equation is fitted to up slope mobilities at $V_{DS} = -20\,\mathrm{V}$. Device fabrication: Tab. 11.3.

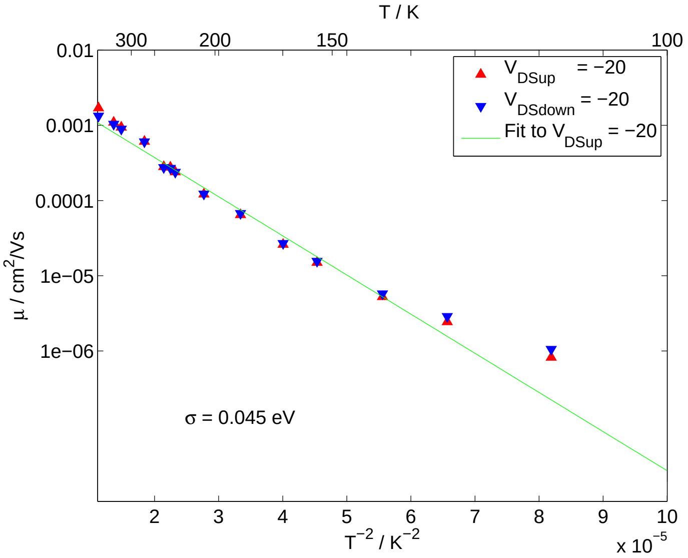

Figure 11.24: Plot of the mobility vs. Temperature in *linear* regime for $\mu \propto \exp\left(-\frac{2}{3}\frac{\sigma}{k_b T}\right)^2$ for the device 1L. Both, mobilities extracted at the down sweep (▼-symbols) and the up-sweep (▲-symbols) of the transfer curves are shown. The equation is fitted to up slope mobilities at $V_{DS} = -20\,\text{V}$. Device fabrication: Tab. 11.3.

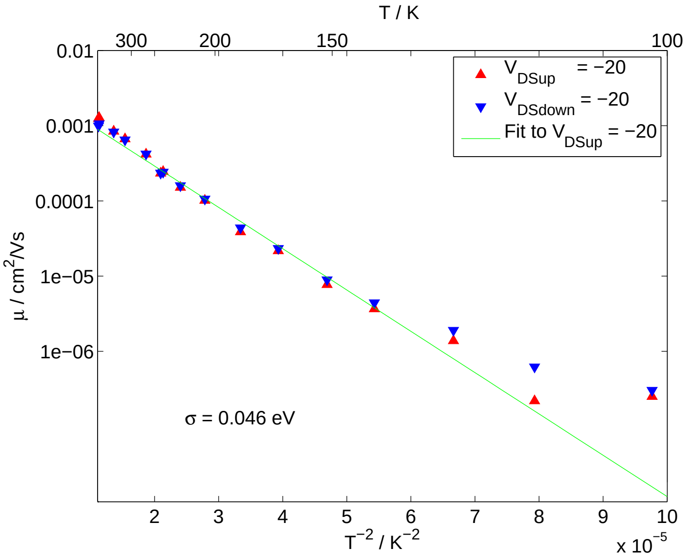

Figure 11.25: Plot of the mobility vs. Temperature in *linear* regime for $\mu \propto \exp\left(-\frac{2}{3}\frac{\sigma}{k_b T}\right)^2$ for the device 1R. Both, mobilities extracted at the down sweep (▼-symbols) and the up-sweep (▲-symbols) of the transfer curves are shown. The equation is fitted to up slope mobilities at $V_{DS} = -20\,\text{V}$. Device fabrication: Tab. 11.3.

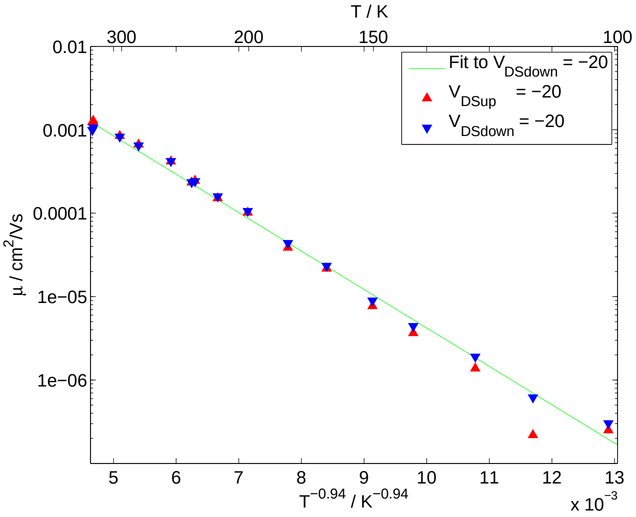

Figure 11.26: Plot of the mobility vs. Temperature in *linear* regime for $\mu \propto \exp\left(-\frac{E_a}{k_b T}\right)^n$ for the device 1R. Both, mobilities extracted at the down sweep (▼-symbols) and the up-sweep (▲-symbols) of the transfer curves are shown. The equation is fitted to up slope mobilities at $V_{DS} = -20\,\mathrm{V}$. Device fabrication: Tab. 11.3.

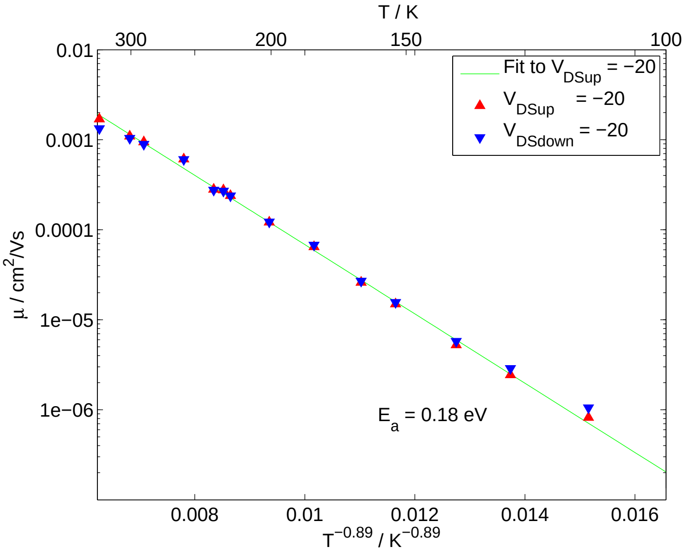

Figure 11.27: Plot of the mobility vs. Temperature in *linear* regime for $\mu \propto \exp\left(-\frac{E_a}{k_b T}\right)^n$ for the device 1L. Both, mobilities extracted at the down sweep (▼-symbols) and the up-sweep (▲-symbols) of the transfer curves are shown. The equation is fitted to up slope mobilities at $V_{DS} = -20\,\mathrm{V}$. Device fabrication: Tab. 11.3.

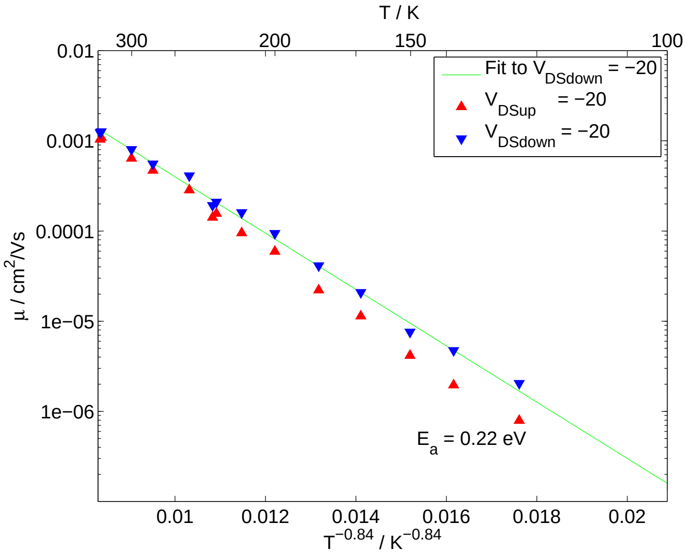

Figure 11.28: Plot of the mobility vs. Temperature in *saturation* regime for $\mu \propto \exp\left(-\frac{E_a}{k_b T}\right)^n$ for the device 1R. Both, mobilities extracted at the down sweep (▼-symbols) and the up-sweep (▲-symbols) of the transfer curves are shown. The equation is fitted to up slope mobilities at $V_{DS} = -20\,\mathrm{V}$. Device fabrication: Tab. 11.3.

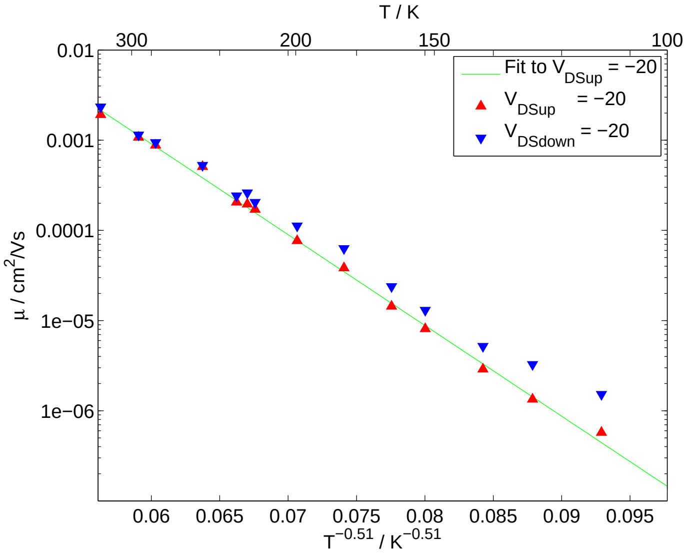

Figure 11.29: Plot of the mobility vs. Temperature in *saturation* regime for $\mu \propto \exp\left(-\frac{E_a}{k_b T}\right)^n$ for the device 1L. Both, mobilities extracted at the down sweep (▼-symbols) and the up-sweep (▲-symbols) of the transfer curves are shown. The equation is fitted to up slope mobilities at $V_{DS} = -20\,\mathrm{V}$. Device fabrication: Tab. 11.3.

11.2.4 Hysteresis

The devices had a generally low hysteresis troughout the cryostatic measurements, as can be seen in Fig. 11.30. Hystereses were higher, when measured inside the glovebox, or in ambient atmosphere (Fig. 11.15). Overall, at room temperature, the relative area of the hystereses was lower, than in the case of Sigma Aldrich P3HT device. At lower temperatures the relative hystereses increased slightly (Fig. 11.30). An significant decrease of the hystereses with the falling temperature, as in the Sigma Aldrich device, was not observed.

The zero voltages stayed constant at all measurements in the cryostat ($V_0 = 0 \pm 2\,\mathrm{V}$), this is seen from the transfer curves in Fig. 11.30 and in quantitative plots of extracted zero voltage vs. temperature (Fig. 11.31 for the 1R device and Fig. 11.32 for the 1L device). Some care must be taken when interpreting these graphs: the down slope zero voltage extracted in the saturation regime $V_0 \Downarrow$ could be compromised by measurement errors. At low temperatures I_D had the *opposite sign* of V_D near the zero voltage in the down-slope. This could be caused by gate leakage current. In the transistor model this is not allowed, so the zero voltage finding algorithm failed here. The up-slope zero voltages extracted in the saturation regime $V_0 \Uparrow$ were not affected by this measurement artifacts.

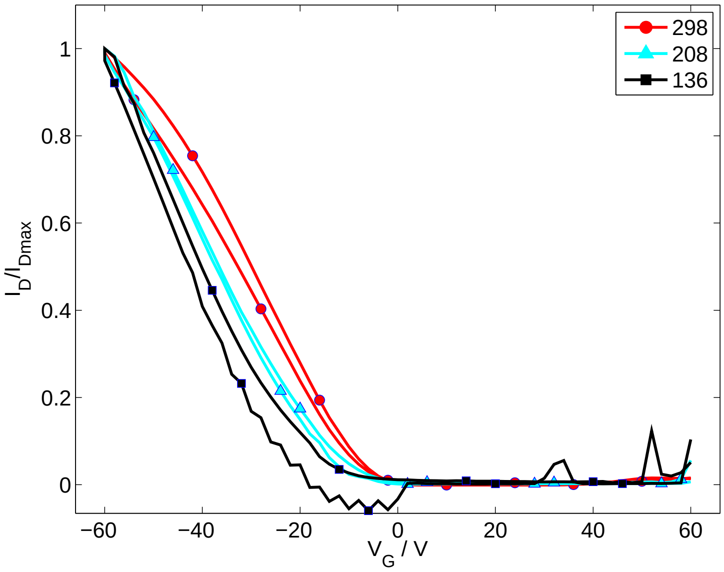

Figure 11.30: Plot of the transfer curves of the 1L device at different temperatures (298 K, 208 K and 136 K) with $V_{DS} = -20\,\mathrm{V}$. Note that parts of the up-slope transfer curve taken at 136 K are negative. Device fabrication: Tab. 11.3.

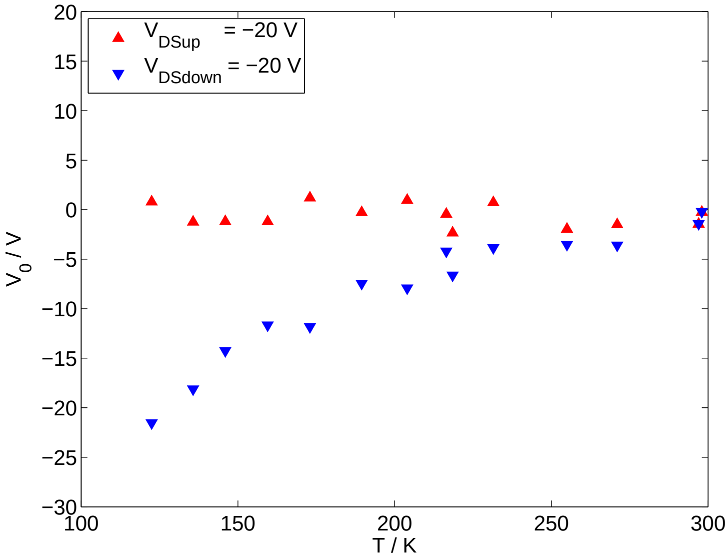

Figure 11.31: Zero voltages vs. Temperature in *saturation* regime for the device 1R, $V_{DS} = -20\,\mathrm{V}$. Both, zero voltages extracted at the down sweep (▼-symbols) and the up-sweep (▲-symbols) of the transfer curves are shown. Down-sweep zero voltages may be incorrect, as explaied in the text. Device fabrication: Tab. 11.3.

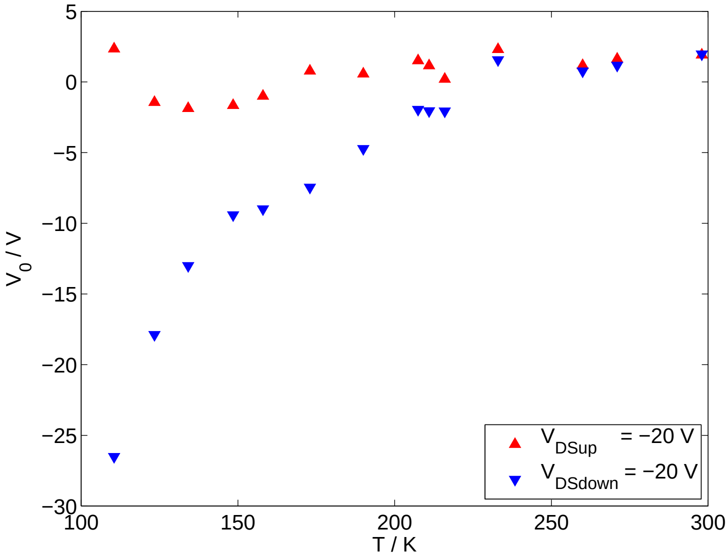

Figure 11.32: Zero voltage vs. Temperature in *saturation* regime for the device 1L, $V_{DS} = -20\,\mathrm{V}$. Both, zero voltages extracted at the down sweep (▼-symbols) and the up-sweep (▲-symbols) of the transfer curves are shown. Down-sweep zero voltages may be incorrect, as explaied in the text. Device fabrication: Tab. 11.3.

11.3 P3HTTFT10

11.3.1 Polymer properties

P3HTTFT10 is a co-polymer synthesized and characterized by Sainova et al.[48] It consists of the main chain hexylthiophene units and 10 mol% electron accepting units (Fig. 11.33). The later, 1,4-Diethienyl-2,3,5,6-tetrafluoro-benzene (TFT) improve the air stability by increasing the polymer's ionisation energy. The number average molecular weight is reported to be $M_n = 14500\,{}^{\mathrm{g}}\!/\!_{\mathrm{mol}}$, the weight average molecular weight is $M_w = 21100\,{}^{\mathrm{g}}\!/\!_{\mathrm{mol}}$, with a polydiversity $PDI = 1.5$. Melting and recrystallisation temperatures are 193 °C and 175 °C respectively. Pure P3HT melts at 230 °C and recrystallize at 198 °C. X-ray diffraction measurements show that higher order peaks from interlamellar spacing disappear in the co-polymer so it has a lower ordering in this (a-axis) direction. The interlamellar distance is 1.6 nm in the co-polymer and 1.7 nm in P3HT. This is in agreement with diffraction data presented in the Morphology part of this thesis.

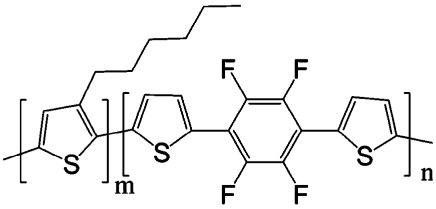

Figure 11.33: Chemical structure of the co-polymer P3HTTFT10. Figure taken from Sainova et al.[48]

11.3.2 Fabrication

The substrate stayed untreated until spincoating. P3HTTFT10 $2\,{}^{\mathrm{g}}\!/\!_{\mathrm{l}}$ solution in TCB was used. It was stirred for 15 min at 50 °C before spincoating. The spincoated substrate was annealed for 60 min at 75 °C. Before evaporating the contacts the substrate stayed in vacuum over the night, where the pressure reached 2.1×10^{-5} mbar. Evaporation rate was $0.2\,{}^{\mathrm{nm}}\!/\!_{\mathrm{s}}$, 50 nm gold were evaporated. Two devices 1L and 1R that were build simultaniously on the same substrate were charactarized.

A summery is given in (Tab. 11.5).

11.3.3 Transfer characteristics

Transfer curves were measured (1) immediately after the device production inside the glovebox, and (2) inside the glovebox after exposure of the device to ambient atmosphere for a duration of 30 min (Fig. 11.34). In the first measurement the drain current was extremely low and hardly any transfer characteristic was visible, but after air exposure a mobility $\mu \approx 5 \times 10^{-4}\,{}^{\mathrm{cm}^2}\!/\!_{\mathrm{Vs}}$ and a zero voltage of $V_0 \approx 15\,\mathrm{V}$ were extracted.

In the next step, the sample was attached to the sampleholder and the device characteristics were measured in ambient atmosphere. The mobility rose further

Table 11.5: Production specifications for the device f231.

Fet 231	
Polymer	Co-polymer P3HTTFT10
Solvent	1,2,4-Trichlorobenzene, Aldrich, anhydrous, $\geq 99\%$
Substrate	Prime grade, $< 10\,\Omega/\mathrm{cm}$, $150\,\mathrm{nm} SiO_2$
Plasma etching	no plasma etching
Spincoating	1500 rpm, 40 s
Drying	1 h, 75 °C
Evacuation	overnight, final pressure 2.1×10^{-5} mbar
Contact evaporation	Au, thickness: 50 nm, duration 210 s

to $\mu \approx 8 \times 10^{-4}\,\mathrm{cm}^2/\mathrm{Vs}$ and zero voltages shifted slightly in negative direction to $V_0 \approx 10\,\mathrm{V}$. Interestingly, the hysteresis area (in Fig. 11.34) decreased in comparison to the one measured in the glovebox before (from 7.5 au. to 5.5 au.). The off-current was higher ($\approx 3 \times 10^{-7}\,\mathrm{A}$), than in the glovebox ($\approx 2 \times 10^{-8}\,\mathrm{A}$) as seen in the logarithmic plot Fig. 11.35.

The transfer characteristics did not change significantly in the further measurements with the device inside the cryostat chamber in helium (at room temperature) and in the glovebox after the cryostatic experiments.

11.3.4 Mobility at cryostatic temperatures

Cryostatic measurements were done down to 130 K. Only the device 1R was characterized, because of an early failure of the electrical contacts to the device 1L.

Fits for models with different temperature dependence of the mobility were done as in the cases before. Fits in Arrhenius-type plots are shown in Fig. 11.36 for mobilities extracted in the saturation regime and in Fig. 11.37 for mobilities extracted in the linear regime of the transfer curves. The activation energy was found to be in the range of $160\,\mathrm{meV} \cdots 176\,\mathrm{meV}$. In the cases, where mobilities were extracted in the saturation regime of the transfer curves, only data measured above 150 K was considered. This was done, because noise obscured the low drain current in the saturation part of the transfer curves (As seen in Fig. 11.38). Good Arrhenius-type fits could be found within the temperature range down to 150 K and 130 K in saturation regime and linear regime respectively.

Strong deviations of the mobilities from non Arrhenius fits using equation (10.4) were found. This is seen in Fig. 11.39 for mobilities extracted in the saturation regime and in Fig. 11.40 for mobilities extracted in the linear regime of the transfer curves. As in the case of devices made with Plextronix P3HT, the mobilities at low temperature are higher then the regression-curve in both cases.

Fits with a variable exponent n (10.5) were also done for both data-sets (Fig. 11.41 and Fig. 11.42). This yielded a value of $n = 0.97$ for mobilities extracted from the linear part of the transfer curves, thus strongly supporting the Arrhenius-type fit. On the other hand, for mobilities extracted from the saturated part of the transfer curves the fit yielded $n = 0.75$.

As with other samples (Sigma Aldrich P3HT and Plextronix P3HT), the data seems to favor high carrier concentration models. A summary of the model fit parameters is found in Tab. 11.6.

Table 11.6: Model Parameters up to their significant digit for device fabricated as described in Tab. 11.5. Standard deviation (which are calculated by the Levenberg Marquard algorithm) of the mobilities is assumed to be 10%. Standard deviation of parameters for low and high n models were in the 0.01 meV and 0.05 meV respectively.

Model	T dependency	parameter in linear regime	parameter in saturation regime
high n models	$\mu \propto \exp\left(-\frac{E_a}{k_b T}\right)$	$E_a = 160\,\mathrm{meV}$	$E_a = 170\,\mathrm{meV}$
low n models	$\mu \propto \exp\left(-\frac{2}{3}\frac{\sigma}{k_b T}\right)^2$	$\sigma = 53\,\mathrm{meV}$	$\sigma = 56\,\mathrm{meV}$
Arbitrary exponent	$\mu \propto \exp\left(-\frac{E_a}{k_b T}\right)^n$	$E_a = 170 \pm 50\,\mathrm{meV},\ n = 0.97. \pm 0.09$	$E_a = 500 \pm 300\,\mathrm{meV},\ n = 0.75 \pm 0.09$

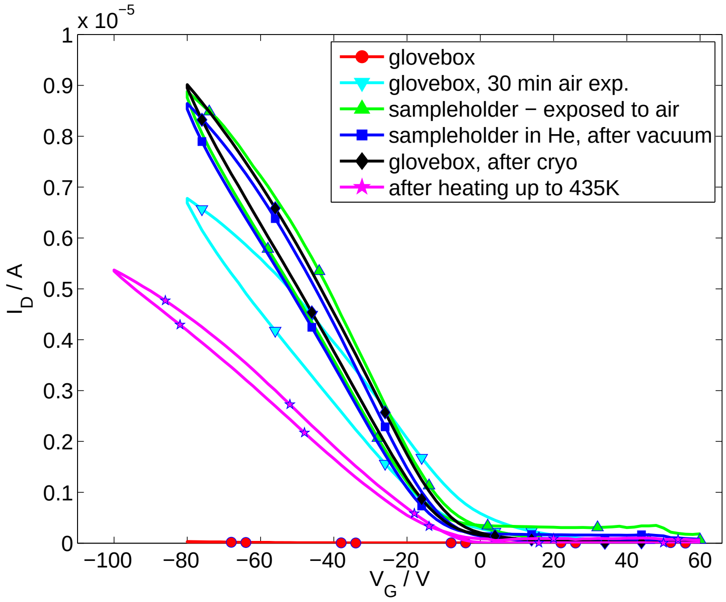

Figure 11.34: Plot of the transfer characteristics of the device 1L at different stages: **a)** inside the glove-box, immediately after fabrication, **b)** inside the glove-box, after exposure to ambient air for a duration of 30 min, **c)** attached to the cryostatic sample holder in ambient atmosphere, **d)** inside the cryostat chamber in vacuum conditions, **e)** inside the glovebox, after all cryostatic experiments were done and **f)** inside the glove-box, after the device was annealed at 435 K. Device fabrication: Tab. 11.5.

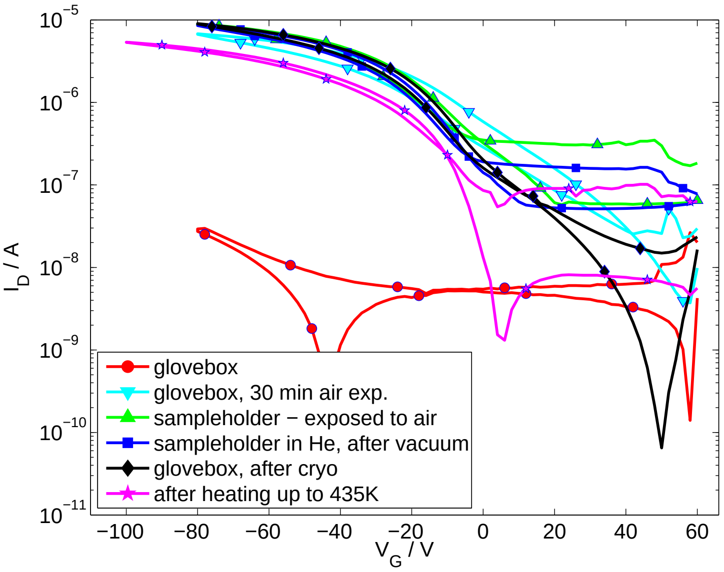

Figure 11.35: Logarithmic plot of the transfer characteristics of the device 1L at different stages: **a)** inside the glove-box, immediately after fabrication, **b)** inside the glove-box, after exposure to ambient air for a duration of 30 min, **c)** attached to the cryostatic sample holder in ambient atmosphere, **d)** inside the cryostat chamber in vacuum conditions, **e)** inside the glovebox, after all cryostatic experiments were done and **f)** inside the glove-box, after the device was annealed at 435 K. Device fabrication: Tab. 11.5.

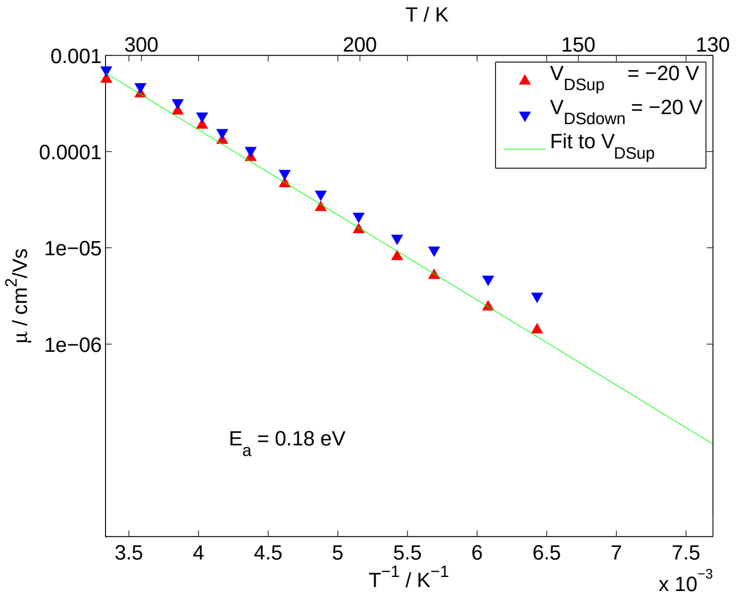

Figure 11.36: Mobility vs. Temperature for $\mu \propto \exp\left(-\frac{E_a}{k_b T}\right)$ for the device 1R. The equation is fitted to up slope mobilities in *saturation* regime at $V_{DS} = -20\,\mathrm{V}$. Both, mobilities extracted at the down sweep (▼-symbols) and the up-sweep (▲-symbols) of the transfer curves are shown. Device fabrication details are summarized in Tab. 11.5.

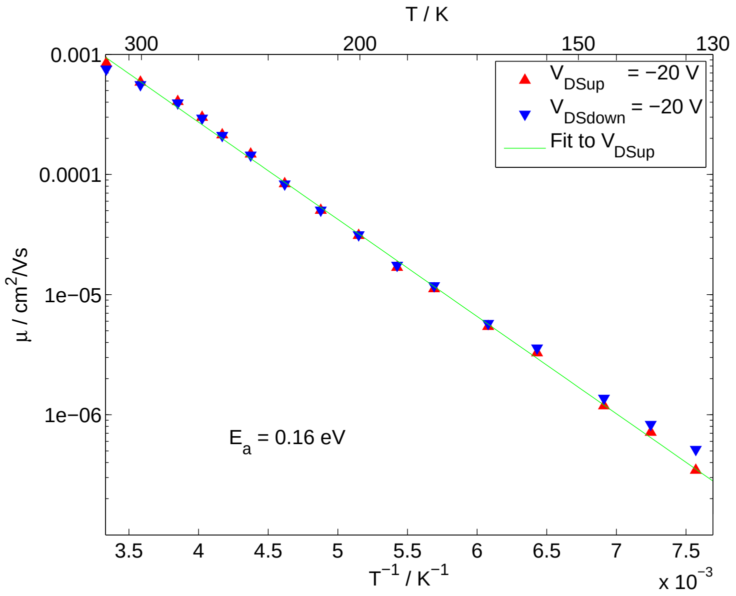

Figure 11.37: Mobility vs. Temperature for $\mu \propto \exp\left(-\frac{E_a}{k_b T}\right)$ for the device 1R. The equation is fitted to up slope mobilities in *linear* regime at $V_{DS} = -20\,\mathrm{V}$. Both, mobilities extracted at the down sweep (▼-symbols) and the up-sweep (▲-symbols) of the transfer curves are shown. Device fabrication details are summarized in Tab. 11.5.

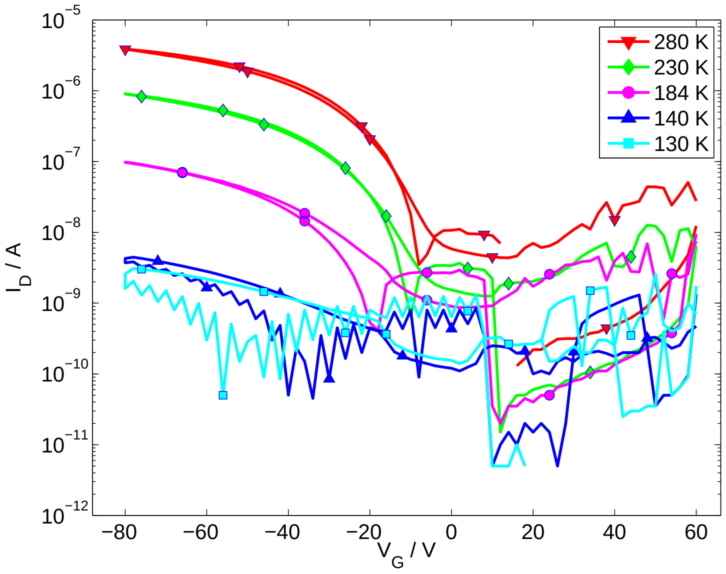

Figure 11.38: Transfer curves measured at different temperatures for the device 1R with $V_{DS} = -20\,\mathrm{V}$. Device fabrication details are summarized in Tab. 11.5.

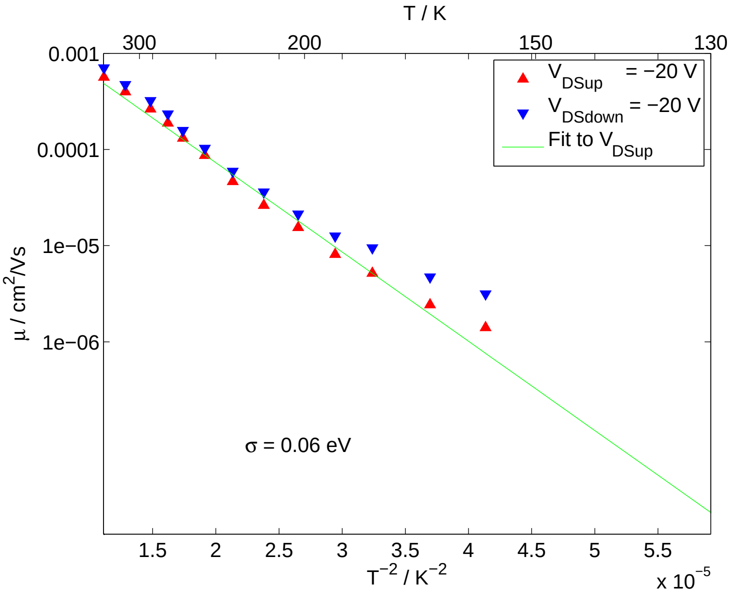

Figure 11.39: Mobility vs. Temperature for $\mu \propto \exp\left(-\frac{2}{3}\frac{\sigma}{k_b T}\right)^2$ for the device 1R. The equation is fitted to up slope mobilities in *saturation* regime at $V_{DS} = -20\,\mathrm{V}$. Both, mobilities extracted at the down sweep (▼-symbols) and the up-sweep (▲-symbols) of the transfer curves are shown. Device fabrication details are summarized in Tab. 11.5.

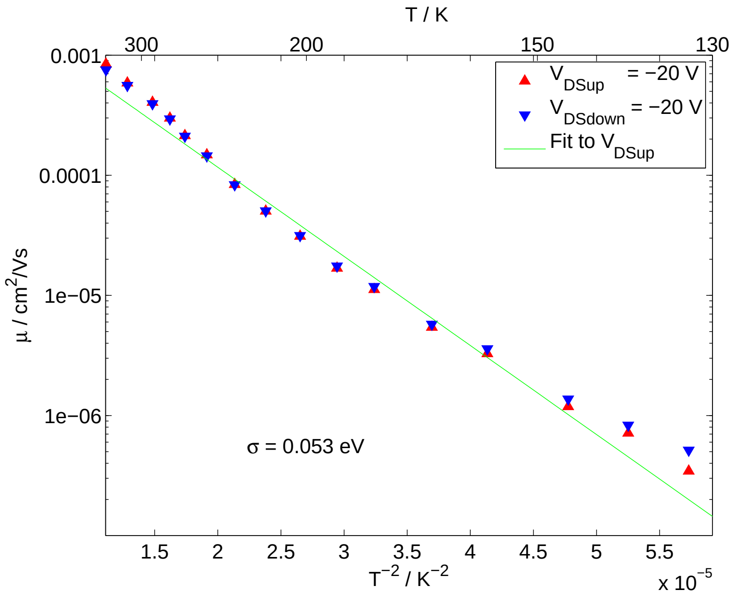

Figure 11.40: Mobility vs. Temperature for $\mu \propto \exp\left(-\frac{2}{3}\frac{\sigma}{k_b T}\right)^2$ for the device 1R. The equation is fitted to up slope mobilities in *linear* regime at $V_{DS} = -20\,\text{V}$. Both, mobilities extracted at the down sweep (▼-symbols) and the up-sweep (▲-symbols) of the transfer curves are shown. Device fabrication details are summarized in Tab. 11.5.

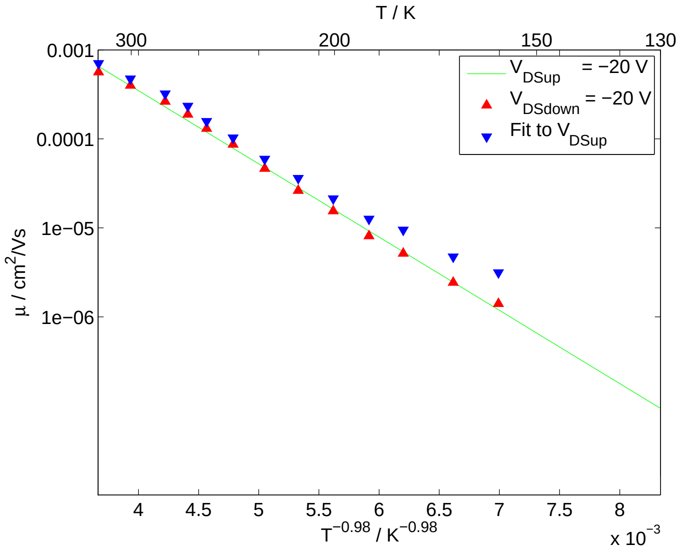

Figure 11.41: Mobility vs. Temperature for $\mu \propto \exp\left(-\frac{E_a}{k_b T}\right)^n$ for the device 1R. The equation is fitted to up slope mobilities in *saturation* regime at $V_{DS} = -20\,\text{V}$. Both, mobilities extracted at the down sweep (▼-symbols) and the up-sweep (▲-symbols) of the transfer curves are shown. Device fabrication details are summarized in Tab. 11.5.

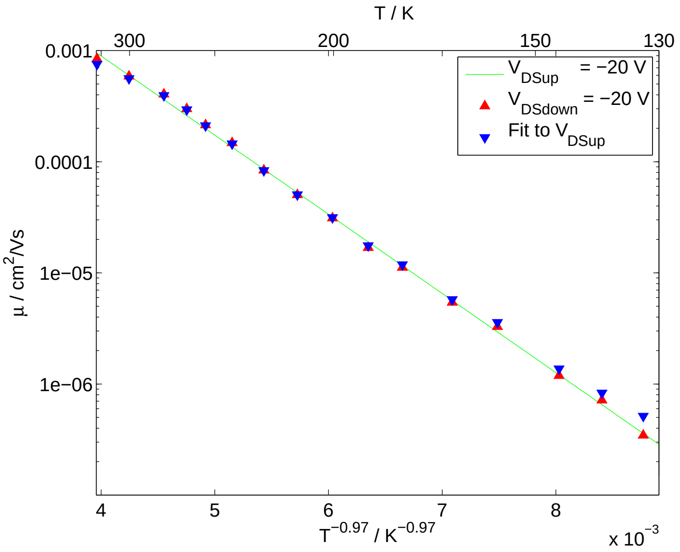

Figure 11.42: Mobility vs. Temperature for $\mu \propto \exp\left(-\frac{E_a}{k_b T}\right)^n$ for the device 1R. The equation is fitted to up slope mobilities in *linear* regime at $V_{DS} = -20\,\mathrm{V}$. Both, mobilities extracted at the down sweep (▼-symbols) and the up-sweep (▲-symbols) of the transfer curves are shown. Device fabrication details are summarized in Tab. 11.5.

11.3.5 Zero voltages and hystereses at cryostatic temperatures

Linear plots of transfer curves for different temperatures are showed in Fig. 11.43. As can be seen from the figure, the relative hysteresis area increased with decreasing temperature but stayed at reasonable low values. Note, that some parts of the transfer curve (up-slope in the range between $V_G = -20\,\mathrm{V} \cdots {+20}\,\mathrm{V}$) were negative at low temperatures. As explained in the previous section, because of this effect, extracted down-slope zero voltages were not correct. Data for up-slope zero voltages seemed to be valid. The temperature dependence of the zero voltages is shown in Fig 11.44. The values of $V_0 \Uparrow = -5\,\mathrm{V}$ were constant for all temperatures within fitting errors.

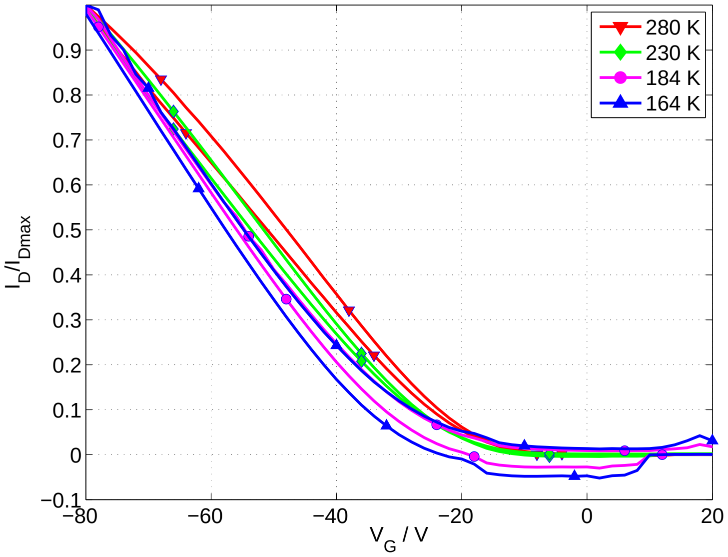

Figure 11.43: Transfer curves recorded at different temperatures inside the cryostat, with normalized y- axis for the device 1R, $V_{DS} = -20\,\mathrm{V}$. Device fabrication details are summarized in Tab. 11.5.

11.3.6 In situ heating experiments

In situ measurements, using the heat stage inside the glovebox, were done up to temperatures of 450 K. The experiments showed a conductivity that rose at increasing temperature, but unfortunately also very high hystereses at elevated temperatures (Fig. 11.45) Nevertheless mobility increase was observed as shown for mobilities extracted in linear regime (Fig. 11.46) and in the saturation regime (Fig. 11.47) of the transfer curves . It was convenient, not to use the Arrhenius-type plots to show the temperature dependence of the mobilities for temperatures above 300 K.

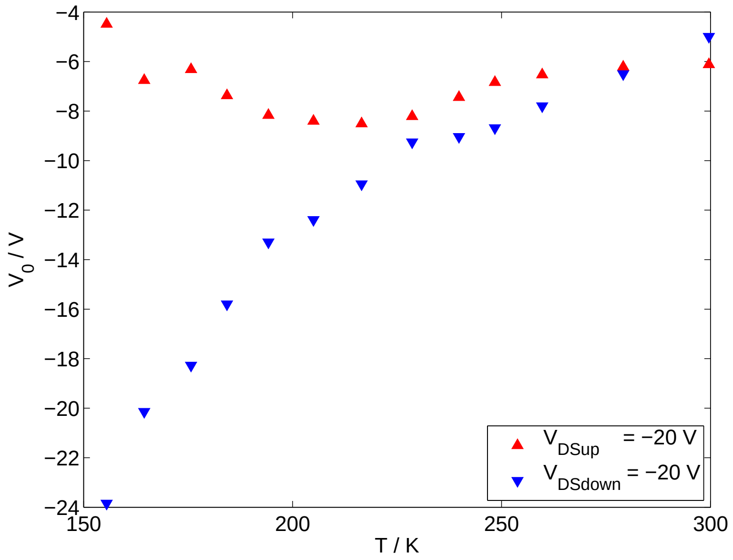

Figure 11.44: Zero voltage vs. Temperature in *saturation* regime for the device 1R. Both, zero voltages extracted at the down sweep (▼-symbols) and the up-sweep (▲-symbols) of the transfer curves are shown. Note, that the down-sweep zero voltages may be incorrect, as explained in the text. Device fabrication details are summarized in Tab. 11.5.

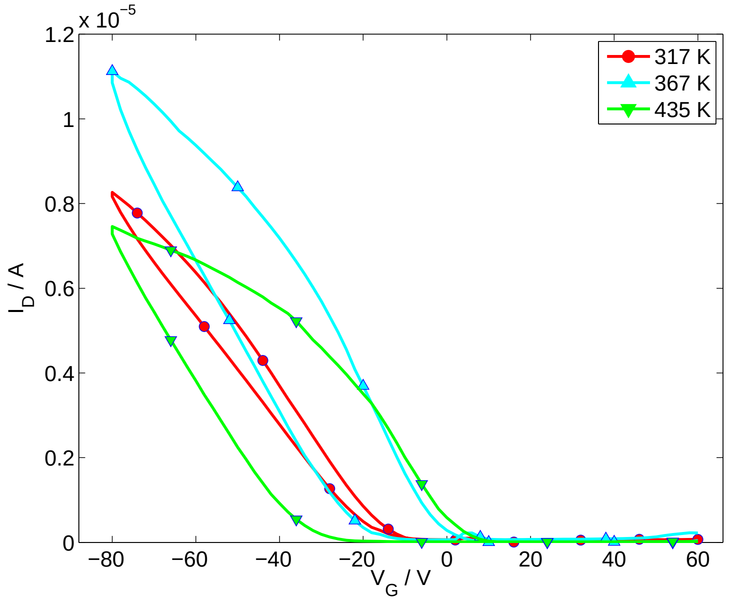

Figure 11.45: Transfer characteristics of the device 1R recorded at above room temperatures, in Argon environment and in darkness. Device fabrication details are summarized in Tab. 11.5.

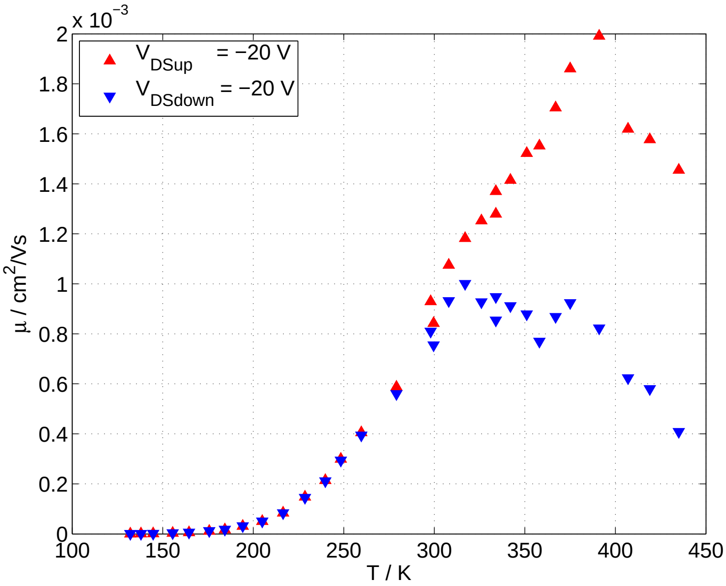

Figure 11.46: Mobility vs. Temperature extracted in *linear* regime of the transfer curves of the device 1R. Some data was recorded at above room temperatures, in Argon environment and in darkness. Device fabrication details are summarized in Tab. 11.5.

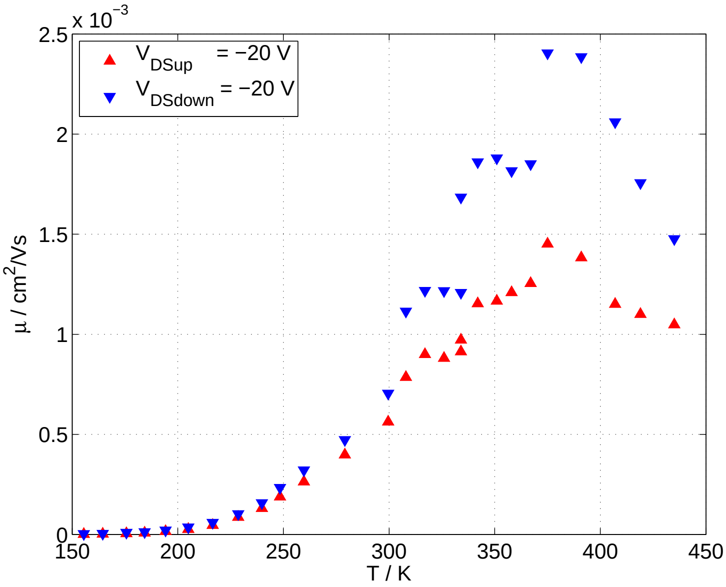

Figure 11.47: Mobility vs. Temperature extracted in *saturation* regime of the transfer curves of the device 1R. Some data was recorded at above room temperatures, in Argon environment and in darkness. Device fabrication details are summarized in Tab. 11.5.

11.3.7 Annealing

After having annealed the device at 250 °C (which is higher than the melting temperature) for 24 hours in vacuum no usefull transfer curve could be measured. Conductivity was very low (Fig. 11.48). Explanation for this could be some residual oxygen that reacted with the semiconductor, or a damaged SiO_2 layer due to thermal stress.

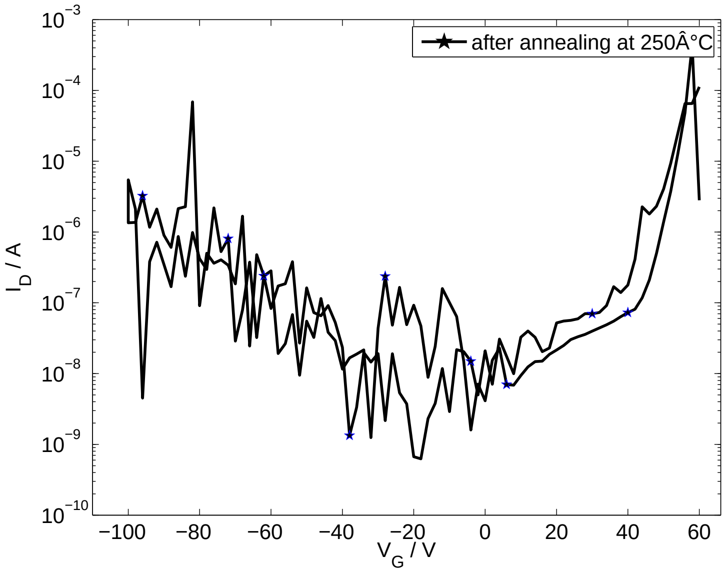

Figure 11.48: Transfer characteristics of the device 1L after annealing at 250 °C in vacuum. Device fabrication details are summarized in Tab. 11.5.

11.3.8 Comparison to initial cryogenic measurements

In the first experiments P3HTTFT5 in chloroform solvent (2 g/l) was used. This is a polymer similar to P3HTTFT10, it differs in the percentage of electron accepting units: 5 mol% compared to 10 mol% in P3HTTFT10. Spincoating was done at 1500 rpm, 22 °C. The substrate was annealed at 50 °C for 5 min, then it stayed in vacuum over the night, before 50 nm gold contacts were evaporated. Mobilities for these two devices on the substrate were extracted for temperatures down to 150 K; the activation energies E_a are 161 meV and 144 meV (Fig. 11.49 and Fig. 11.50). That is a slightly lower value than for P3HTTFT10 in TCB solvent.

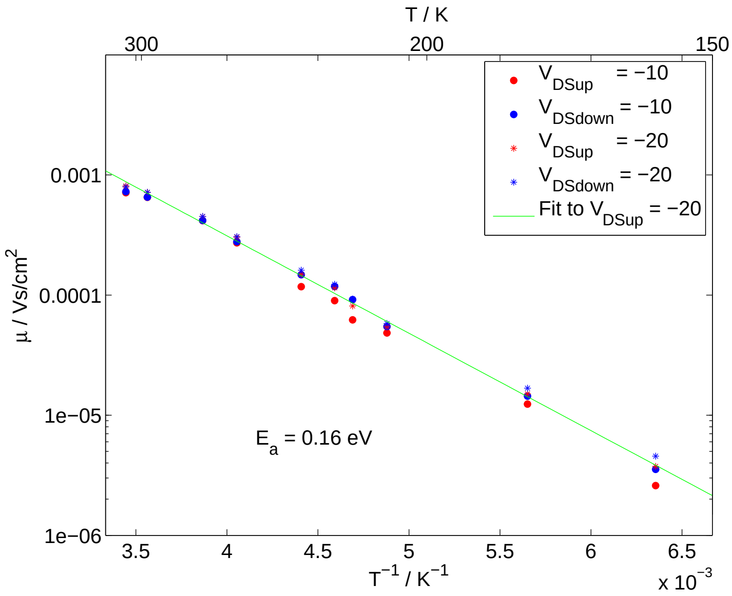

Figure 11.49: Plot of Mobility vs. Temperature of device 1L (produced by P3HTTFT5 spin casting from CHCL3 solution) for $\mu \propto \exp\left(-\frac{E_a}{k_b T}\right)^n$. The equation was fitted to up slope mobilities at $V_{DS} = -20\,\mathrm{V}$ extracted in *linear* regime.

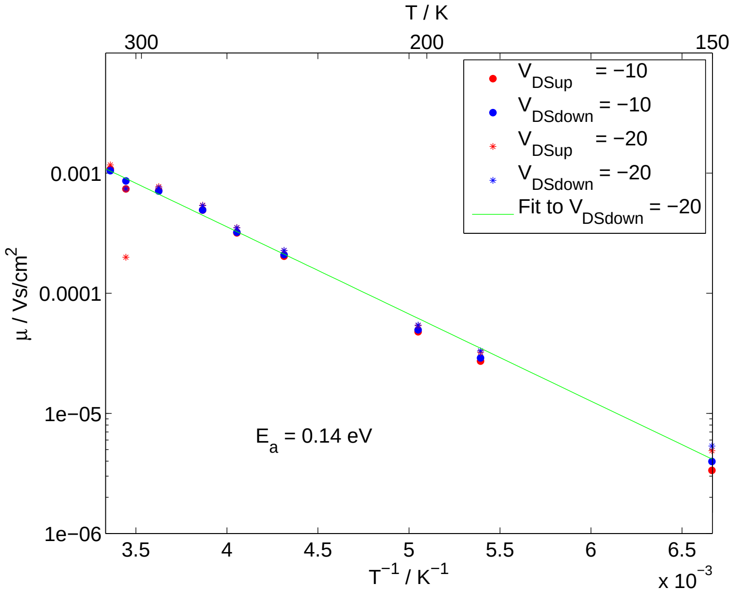

Figure 11.50: Plot of Mobility vs. Temperature of device 1R (produced by P3HTTFT5 spin casting from CHCL3 solution) for $\mu \propto \exp\left(-\frac{E_a}{k_b T}\right)^n$. The equation was fitted to up slope mobilities at $V_{DS} = -20\,\mathrm{V}$ extracted in *linear* regime.

11.4 Summary of cryostatic measurements

All three samples of P3HT show thermally activated field-effect mobilities μ_f in the accessible temperature range (Fig. 11.51). In all cases, the best fit to the mobility could be obtained with $ln(\mu_f) \propto 1/T^m$ with $m < 1$. Reasonabel fit results were also found for $ln(\mu_f) \propto 1/T$ but significant deviations from $ln(\mu_f) \propto 1/T^2$ were seen. The experiments supported charge transport models, where high charge carrier concentrations n were taken into account and which lead to an Arrhenius dependence of μ_f on temperature $ln(\mu_f) \propto 1/T$. The reason for $m < 1$ could be the onset of less temperature dependent tunneling[1] at temperatures around 100 K giving rise to a flattening of the curves in this temperature range.

The difference in room temperature mobilities and activation energies of the samples (Tab. 11.7) may be explained by the different morphologies caused by different molecular weights. Chang et al.[8, 9] also measured better performace of high M_W polymers when spin coating from high boiling temperature solvents, as in our experiments.

Mobilities extracted at high gate voltages (linear regime) were higher but had the same activation energies as those extracted at low gate voltages (saturation regime). Mobility dependence on gate bias is also common for high n models and were experimentally observed by other groups. Details about M_W and gate bias dependence in those experiments are given in part III of this work. The hystereses in transfer plots generally decreased with lower temperatures. For the Sigma Aldrich sample the hysteresis area could even be Arrhenius plotted and a fit gave a hysteresis activation energy of $E_a^{Hysteresis} = 170\,\text{meV}$. The hystereses could be explained by slow accumulation of quasi-immobile charges at the isolator interface that do not contribute to conductivity during the measurement process.

Table 11.7: Activation energies and mobility at room temperature for the three examined P3HT materials.

Sample	M_W $^{kg}/_{mol}$	PDI	rr %	μ $^{cm^2}/_{Vs}$	E_a meV
Sigma Aldrich	87	2.5	98	0.02	78
Plexcore OS 1100	50	2	95	0.001	130
P3HTTFT10	21	1.5	–	0.0004	165

---

[1] When tunneling occurs directly between two sites of the same energy.

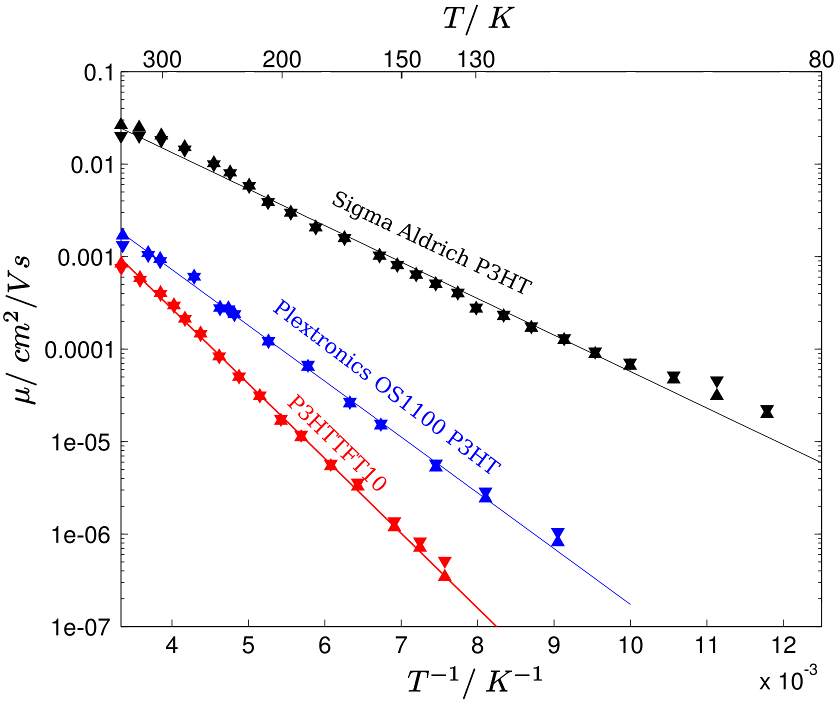

Figure 11.51: Temperature dependence of the mobilities of the three sample materials used in this work.

Chapter 12

Other measurements

12.1 Air exposure and conductivity

All three P3HT devices discussed in cryostatic measurement chapter experienced a high irreversible increase of the mobility after short exposure to air. Here, the measurements were repeated to confirm this. All production steps of these FETs are executed in argon atmosphere, there was no contact to ambient air. Device specifications are given in Tab. 12.1. After production, the devices were electrically characterized while still in argon atmosphere. They showed very low conductivities (Fig. 12.1). The conductivities increased to expected values after a very short exposure to ambient air[1] in darkness (Fig. 12.2) while retaining the same off-current. The origin of this sharp increase in mobility is not clear. A summary of the findings is given in Tab. 12.2.

Table 12.1: Production specifications for the device f243.

Fet 243	
Polymer	Co-polymer P3HTTFT10
Solvent	1,2,4-Trichlorobenzene, Aldrich, anhydrous, $\geq 99\%$
Substrate	Prime grade, $< 10\,\Omega/\mathrm{cm}$, 150 nmSiO_2
Plasma etching	100%, O_2 flow rate $8\,\mathrm{l/h}$, pressure: 0.2 mbar, duration: 30 s
Spincoating	1500 rpm, 40 s
Drying	2 h, 70 °C
Evacuation	overnight, final pressure 2×10^{-5} mbar
Contact evaporation	Au, thickness: 50 nm, duration 5 min

Table 12.2: Parameters for devices Tab. 12.1, before and after air exposure of a duration of $\approx 10\,\mathrm{s}$, $V_{DS} = -20\,\mathrm{V}$. Since the transfer curves before air exposure are very irregular, the first four fit parameters are not relyable.

	$\mu_{lin} \downarrow$ cm^2/Vs	$\mu_{lin} \uparrow$ cm^2/Vs	$V_{0lin} \downarrow$ V	$V_{0lin} \uparrow$ V	$\mu_{sat} \downarrow$ cm^2/Vs	$\mu_{sat} \uparrow$ cm^2/Vs	$V_{0sat} \downarrow$ V	$V_{0sat} \uparrow$ V	*Hysteresis* *a.u.*
dev. 1L, before exp.	-1.25e-05	-2.20e-05	-22.6	-64.5	3.12e-05	5.60e-05	10.3	-75.7	2.88e-06
dev. 2L, before exp.	-2.50e-06	-1.23e-05	-24.4	-77.2	3.27e-05	2.27e-05	-34.5	76.6	9.56e-07
dev. 1R, before exp.	2.35e-05	2.41e-05	-17.1	-22.4	1.58e-05	7.50e-06	-7.85	-3.2	2.18e-06
dev. 2R, before exp.	2.65e-05	3.08e-05	-9.77	-29	1.94e-05	1.47e-05	-2.95	-24.6	5.35e-06
dev. 1L, after exp.	2.24e-04	3.22e-04	35.6	-6.36	4.09e-04	2.47e-04	0.566	-5.55	4.19e-05
dev. 2L, after exp.	2.72e-04	4.06e-04	41.7	-5.19	4.64e-04	2.58e-04	4.76	-1.16	5.80e-05
dev. 1R, after exp.	3.25e-04	5.66e-04	60.3	-8.46	7.47e-04	4.63e-04	5.09	-7.63	1.07e-04
dev. 2R, after exp.	2.93e-04	4.97e-04	46.1	-14.2	7.27e-04	4.23e-04	-1.83	-13.3	8.30e-05

---

[1] The substrate was inside a petri dish wrapped in aluminium foil when exposed to air for some 10 seconds

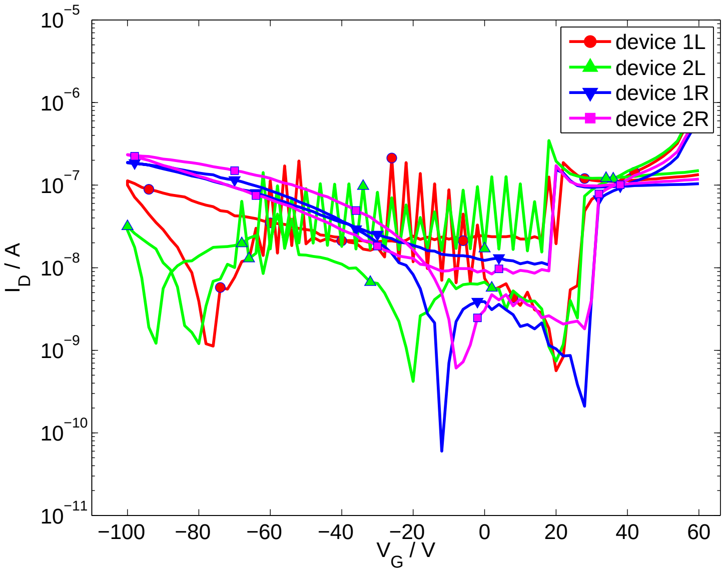

Figure 12.1: Transfer curves for four identical devices on the same substrate, shortly after contact evaporation, before air exposure at $V_{DS} = -20\,\mathrm{V}$. Device specifications are given in Tab. 12.1

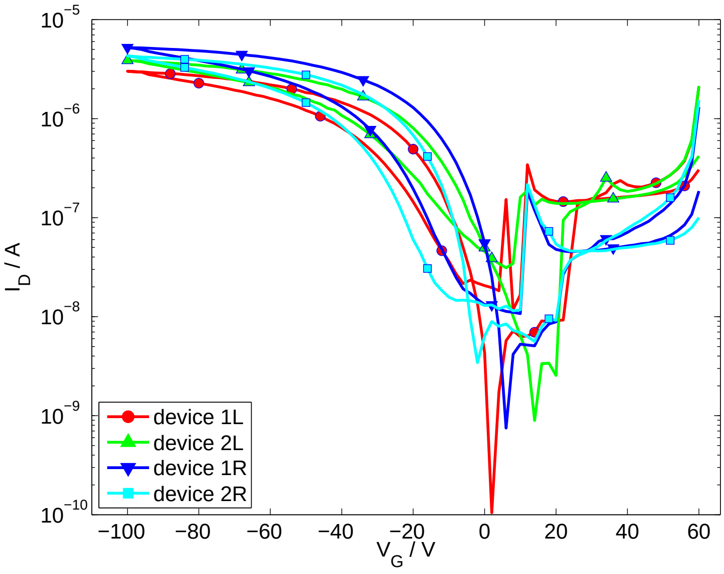

Figure 12.2: Transfer curves for four identical devices (the same as in Fig. 12.1) on the same substrate, after air exposure with a duration of $\approx 10\,\mathrm{s}$. The curves vere recorded with $V_{DS} = -20\,\mathrm{V}$. Device specifications are given in Tab. 12.1

12.2 Parametric analyser setup

In this section the setup of the measurement routine of the parametric analyser and the role of the leakage current are discussed. Depending on integration time per data point and delay time prior to recording each data point, the transfer curves for the same device under the same conditions did differ. The delay time is the length of time between applying the voltage to the device (in this case gate and drain voltage) and the actual current measurement (Fig. 12.3). This means, that the currents can reach a steady state, before being measured. In our experiments we used a 1 point average[2] except for low temperatures where noise occurred and higher average-numbers were used (up to 512).

Changing the integration time to 128 averages and setting the delay time from zero[3] to 0.1 sec has a big impact on the off current.

First the effect on the *leakage current* I_G is discussed. The off current changes from roughly 10×10^{-7} A to 10×10^{-8} A, when adding the leakage current I_G to I_D and doing a one point integration measurement (Fig. 12.4 and Fig. 12.7). The *setup of the parametric analyser* had further impacts on the measurements: The off-currents decreased further to 10×10^{-9} A when a longer integration time and delay time was used (Fig. 12.5 and Fig. 12.6). The gate current was also affected by the setup of integration and delay time. As seen in Fig. 12.4 and Fig. 12.5, it decreased by an order of magnitude, when the average number was increased from 1 to 128.

A comparison of transfer curves measured under the same conditions, but with different parametric analyser setups, are shown in the linear plot Fig. 12.8. An increase in the hysteresis and decreasing max. I_D were observed, when a higher average-number or longer delay time was chosen. This can be explained by higher bias stressing. On the positive side, the measured off-currents could also be influenced (in a range of two orders of magnitude), as shown in the logarithmic plot (fig. 12.9). All measurements were performed with devices described by Tab. 12.1.

These effects can probably be explained by quasi-immobile charges, that upon applying some voltage to the gate electrode of the device cause some I_D current until equilibrium is reached. By increasing the delay-time or the averaging-number, these currents are allowed to settle. On the other hand, if the quasi-immobile charges are allowed to reach full equilibrium state, a higher hysteresis emerges, since higher V_G is then required to inject mobile charges in order to reach the required conductivity.

Table 12.3: Fit parameters for transfer curves acquired with the parametric analyser set to different averaging numbers and delay times, on the same device, at the same conditions (darkness, argon atmosphere). Details on the device fabrication can be found in Tab. 12.1.

	$\mu_{lin} \downarrow$ cm^2/Vs	$\mu_{lin} \uparrow$ cm^2/Vs	$V_{0lin} \downarrow$ V	$V_{0lin} \uparrow$ V	$\mu_{sat} \downarrow$ cm^2/Vs	$\mu_{sat} \uparrow$ cm^2/Vs	$V_{0sat} \downarrow$ V	$V_{0sat} \uparrow$ V	*Hysteresis* *a.u.*
1 average, no delay time	3.72e-04	4.43e-04	35.9	13	7.02e-04	5.55e-04	0.298	-2.29	3.36e-05
128 averages, no delay time	3.16e-04	4.35e-04	46.1	3.32	5.94e-04	4.32e-04	3.22	-3.27	5.77e-05
128 avr. 0.1s delay time	3.10e-04	4.33e-04	42.9	-0.55	4.79e-04	3.74e-04	5.69	-3.11	6.56e-05

---

[2] One point average correlates to a time of 1/50 s for European 50 Hz mains.

[3] The standard delay time was zero in all our measurements.

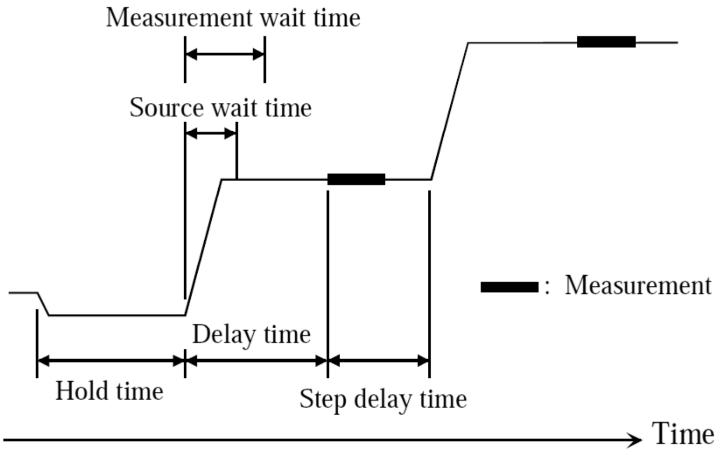

Figure 12.3: Parametric analyser sweep timings. The applied voltages are shown in the y-axis. Source: Agilent E5260 Series User's Guide

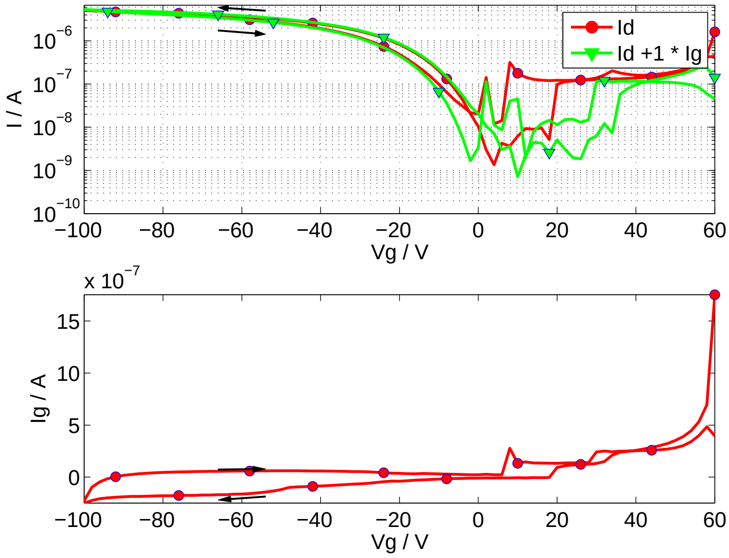

Figure 12.4: **Above)** measured drain current for $V_{DS} = -20\,\mathrm{V}$ and the same current corrected by adding the I_G and **below)** gate current I_G are shown as a function of gate voltage. The parametric analyser was set to **1 average** per data point and to **no delay time**. Details on the device fabrication can be found in Tab. 12.1.

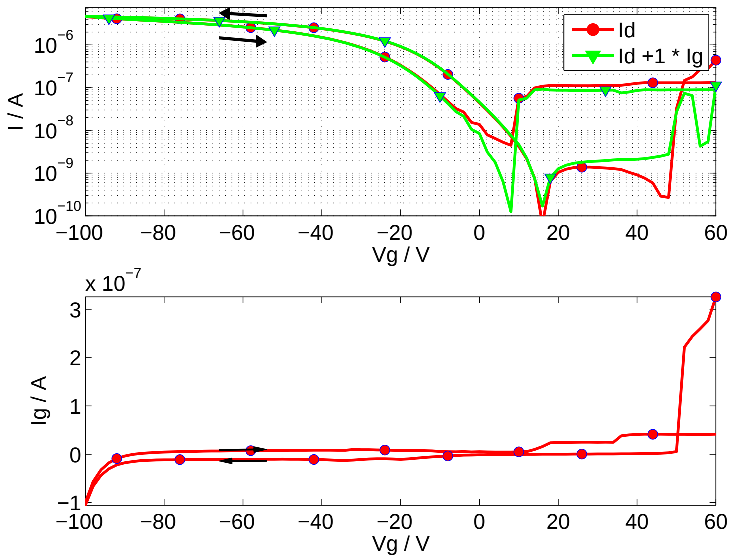

Figure 12.5: **Above)** measured drain current for $V_{DS} = -20\,\mathrm{V}$ and the same current corrected by adding the I_G and **below)** gate current I_G are shown as a function of gate voltage. The parametric analyser was set to **128 average** per data point and to **no delay time**. Details on the device fabrication can be found in Tab. 12.1

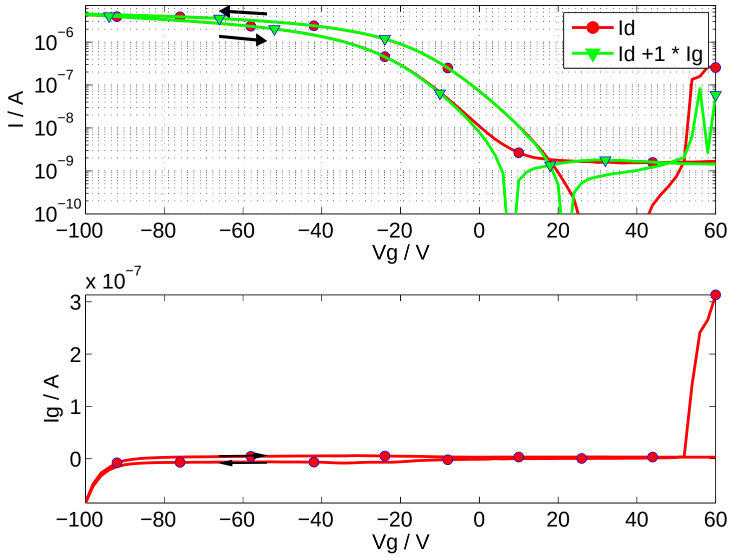

Figure 12.6: **Above)** measured drain current for $V_{DS} = -20\,\mathrm{V}$ and the same current corrected by adding the I_G and **below)** gate current I_G are shown as a function of gate voltage. The parametric analyser was set to **128 average** per data point and to **0.1 sec delay time**. Details on the device fabrication can be found in Tab. 12.1

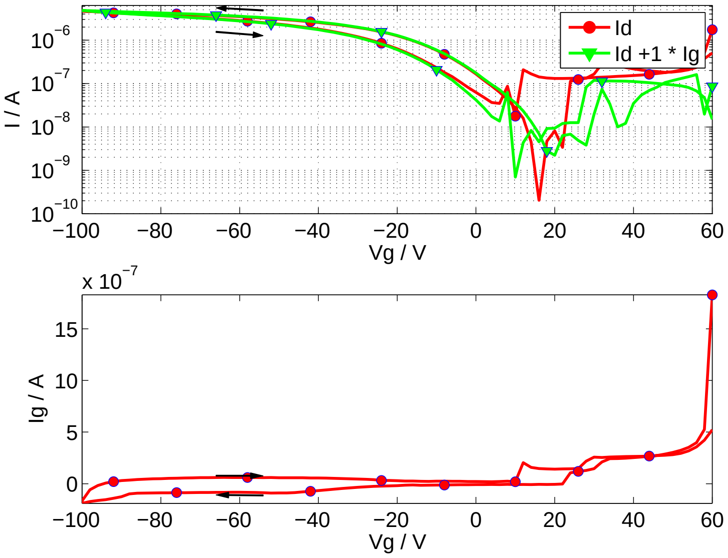

Figure 12.7: **Above)** measured drain current for $V_{DS} = -20\,\mathrm{V}$ and the same current corrected by adding the I_G and **below)** gate current I_G are shown as a function of gate voltage. The parametric analyser was set to **1 average** per data point and to **no delay time**. Acquired in the end of the measurement cycle. Details on the device fabrication can be found in Tab. 12.1.

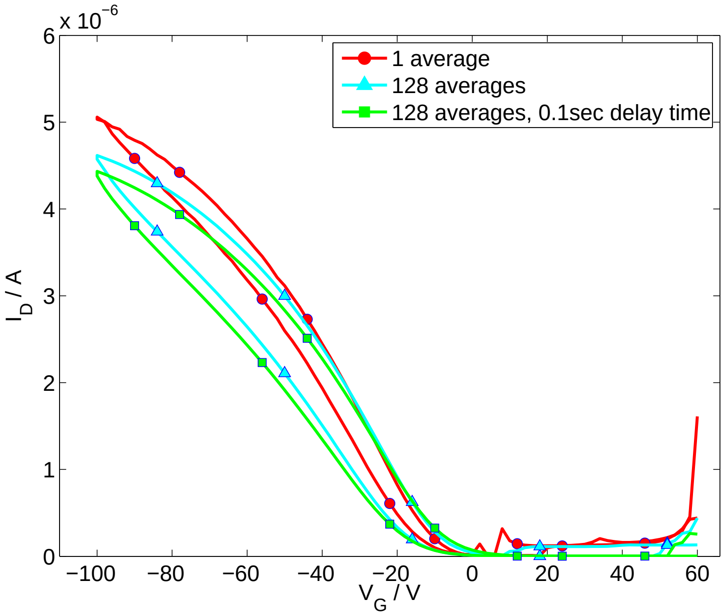

Figure 12.8: Plot of the transfer curves (with $V_{DS} = -20\,\mathrm{V}$) acquired with the parametric analyser at different settings for the averaging and the delay time. The device was under the same conditions at all measurements. Details on the device fabrication can be found in Tab. 12.1.

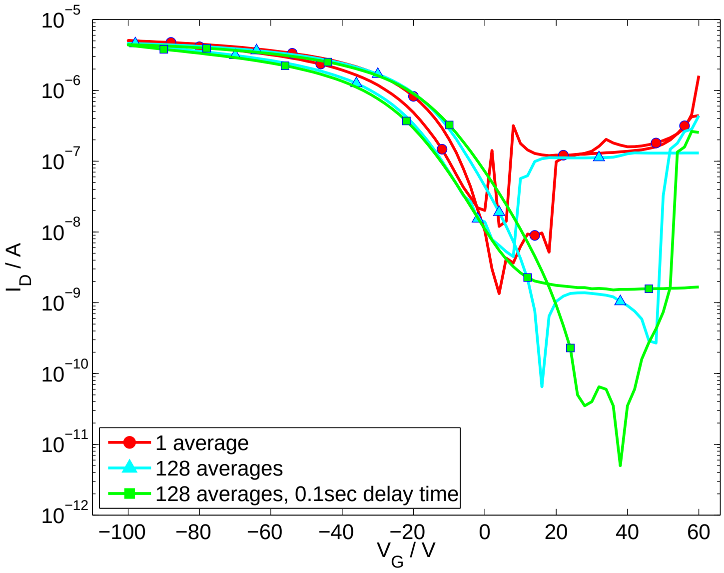

Figure 12.9: Logarithmic plot of the transfer curves (with $V_{DS} = -20\,\mathrm{V}$) acquired with the parametric analyser at different settings for the averaging and the delay time. The device was under the same conditions at all measurements. Details on the device fabrication can be found in Tab. 12.1.

12.3 Post annealing measurements

Motivated by publication cited above (Page 60) annealing experiments were performed on an P3HTTFT10 polymer based FET. The device was prepared as usually from P3HTTFT10 in TCB solution (Tab. 12.1). After fabrication it was exposed to ambient air for 10 seconds in order to achieve conductivity. Annealing and electrical characterisation were all made inside the glovebox. The device was annealed at temperatures from 110 °C up to 199 °C for a duration of 10 min with 10 °C steps in the dark. After each annealing step, subsequent to annealing, transfer curves were recorded at 26 °C.

The transfer curves did not change significantly until 160 °C. At higher temperatures, the mobility decreased. Transfer curves measured with $V_D = -20\,\mathrm{V}$ are shown in Fig. 12.10 and Fig. 12.11 and the fit parameters are summarized in Tab. 12.4. Transfer curves measured with $V_D = -40\,\mathrm{V}$ are shown in Fig. 12.12, Fig. 12.13 and the fit parameters are summarized in Tab. 12.5.

After 199 °C the transfer curves did not showed a meaningfull transfer characteristics, probably the SiO_2 layer was damaged through the shock of rapid temperature change, when the substrate was put on the hotplate. Improved mobility upon annealing at 150 °C as reported by Shinuk Cho at al.[11] could not be observed in this experiment.

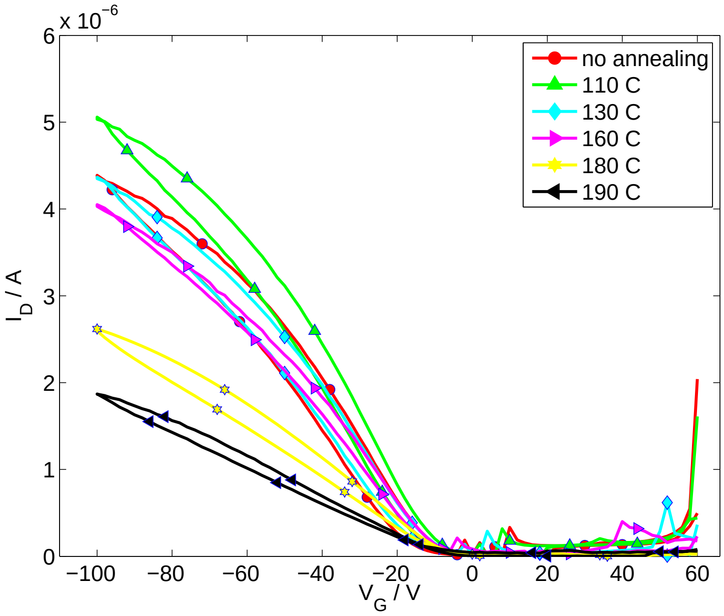

Figure 12.10: Plot of the transfer curve measured before annealing and of the transfer curves after subsequent annealing steps. Annealing temperatures ranged from 110 °C to 190 °C. After each annealing, the transfer curves were recorded at 26 °C. All data was measured at $V_{DS} = -20\,\mathrm{V}$. Details on the device fabrication can be found in Tab. 12.1.

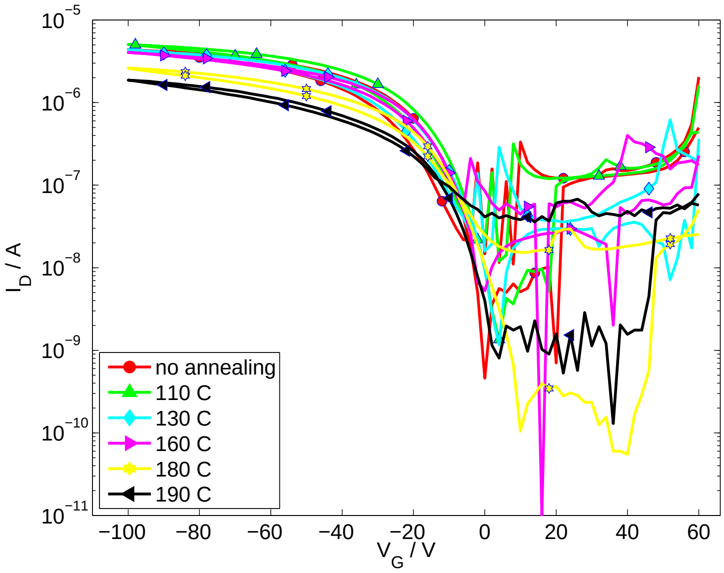

Figure 12.11: Logarithmic plot of the transfer curve measured before annealing and of the transfer curves after subsequent annealing steps. Annealing temperatures ranged from 110 °C to 190 °C. After each annealing, the transfer curves were recorded at 26 °C. All data was measured at $V_{DS} = -20\,\mathrm{V}$. Details on the device fabrication can be found in Tab. 12.1.

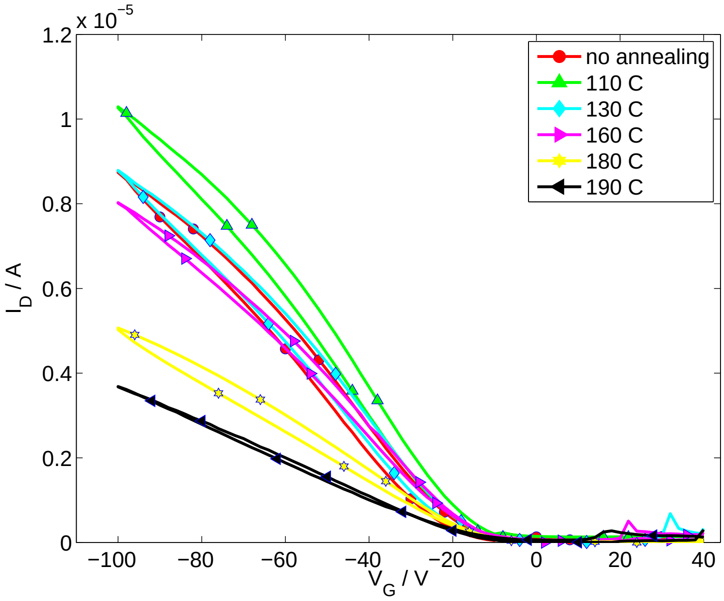

Figure 12.12: Plot of transfer curve measured before annealing and of transfer curves after subsequent annealing steps. Annealing temperatures ranged from 110 °C to 190 °C. After each annealing, the transfer curves were recorded at 26 °C. All data was measured at $V_{DS} = -40\,\mathrm{V}$. Details on the device fabrication can be found in Tab. 12.1.

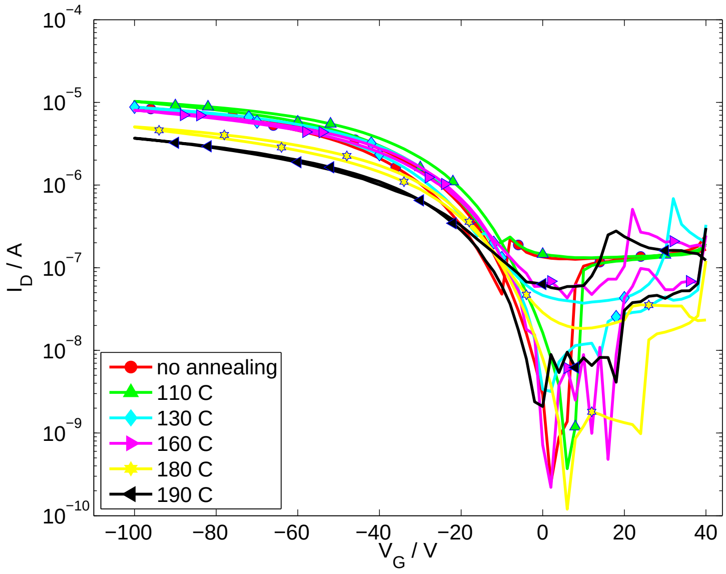

Figure 12.13: Logarithmic plot of the transfer curve measured before annealing and of the transfer curves after subsequent annealing steps. Annealing temperatures ranged from 110 °C to 190 °C. After each annealing, the transfer curves were recorded at 26 °C. All data was measured at $V_{DS} = -40\,\mathrm{V}$. Details on the device fabrication can be found in Tab. 12.1.

Table 12.4: Parameters extractet from the transfer curves that were recorded at 26 °C after each annealing step with different annealing temperatures. Both, parameters extracted from down-slope and up-slope parts of the transfer curves are listed. All transfer curves were measured with $V_{DS} = -20\,\mathrm{V}$.

	$\mu_{lin} \downarrow$ cm^2/Vs	$\mu_{lin} \uparrow$ cm^2/Vs	$V_{0lin} \downarrow$ V	$V_{0lin} \uparrow$ V	$\mu_{sat} \downarrow$ cm^2/Vs	$\mu_{sat} \uparrow$ cm^2/Vs	$V_{0sat} \downarrow$ V	$V_{0sat} \uparrow$ V	$Hysteresis$ $a.u.$
no annealing	3.32e-04	4.20e-04	32.6	4.33	6.34e-04	4.80e-04	-1.08	-5.67	3.74e-05
110 °C/ 10 min	3.72e-04	4.43e-04	35.9	13	7.02e-04	5.55e-04	0.298	-2.29	3.36e-05
120 °C/ 10 min	3.70e-04	4.34e-04	30.8	10.8	6.82e-04	5.39e-04	-1.25	-3.41	2.84e-05
130 °C/ 10 min	3.45e-04	4.07e-04	26.5	6.63	5.38e-04	4.37e-04	0.0547	-2.73	2.04e-05
140 °C/ 10 min	3.40e-04	4.03e-04	34.8	13.1	6.94e-04	5.20e-04	-0.0211	-2.27	2.31e-05
150 °C/ 10 min	3.47e-04	3.89e-04	30.9	16.1	6.97e-04	5.34e-04	-0.475	-1.18	1.38e-05
160 °C/ 10 min	3.22e-04	3.51e-04	25.4	14.9	5.69e-04	4.58e-04	-0.294	-0.546	4.48e-06
170 °C/ 10 min	2.50e-04	2.83e-04	42.9	25.6	4.75e-04	2.68e-04	11.2	14.2	1.27e-05
180 °C/ 10 min	2.20e-04	2.44e-04	20.1	3.81	3.21e-04	2.07e-04	1.87	3.57	1.70e-05
190 °C/ 10 min	1.77e-04	1.87e-04	7.59	-1.5	2.02e-04	1.10e-04	1.29	6.65	5.92e-06

Table 12.5: Parameters extractet from the transfer curves that were recorded at 26 °C after each annealing step with different annealing temperatures. Both, parameters extracted from down-slope and up-slope parts of the transfer curves are listed. All transfer curves were measured with $V_{DS} = -40\,\mathrm{V}$.

	$\mu_{lin} \downarrow$ cm^2/Vs	$\mu_{lin} \uparrow$ cm^2/Vs	$V_{0lin} \downarrow$ V	$V_{0lin} \uparrow$ V	$\mu_{sat} \downarrow$ cm^2/Vs	$\mu_{sat} \uparrow$ cm^2/Vs	$V_{0sat} \downarrow$ V	$V_{0sat} \uparrow$ V	$Hysteresis$ $a.u.$
no annealing	3.32e-04	4.62e-04	37.6	4.51	7.09e-04	6.34e-04	-2.92	-6.04	4.09e-05
110 °C/ 10 min	3.56e-04	4.88e-04	49.1	13.9	8.38e-04	7.21e-04	-0.319	-2.11	4.42e-05
120 °C/ 10 min	3.32e-04	4.66e-04	50.6	12.9	8.01e-04	6.79e-04	-1.87	-3.21	4.21e-05
130 °C/ 10 min	3.24e-04	4.49e-04	41	7.2	6.99e-04	5.88e-04	-1.48	-3.06	3.62e-05
140 °C/ 10 min	3.19e-04	4.39e-04	49.6	13.8	7.95e-04	6.44e-04	-1.54	-1.72	3.38e-05
150 °C/ 10 min	3.20e-04	4.15e-04	47.1	17.9	7.83e-04	6.15e-04	-1.2	0.348	2.35e-05
160 °C/ 10 min	2.99e-04	3.71e-04	40.2	16.8	6.68e-04	5.28e-04	-1.05	0.736	1.58e-05
170 °C/ 10 min	2.41e-04	3.24e-04	53.5	19.3	4.99e-04	3.89e-04	10.5	12.2	2.05e-05
180 °C/ 10 min	2.03e-04	2.91e-04	32	-3.1	3.81e-04	2.86e-04	0.6	2.59	2.31e-05
190 °C/ 10 min	1.81e-04	1.98e-04	11	3.25	2.60e-04	1.68e-04	-0.575	6.37	8.01e-07

Chapter 13

Summary

In conclusion, various aspects of OFETs with P3HT as active semiconductor were analyzed. From temperature dependent measurements in the range of 80 to 300 K it was shown that the charge transport mechanism could be explained best by models that account for high charge carrier concentration in the accumulation layer. Those models predict an Arrhenius dependence of mobility on temperature $\ln(\mu) \propto 1/T$, and a power dependence on gate bias. Arrhenius plots of mobility gave reasonable fit results and higher mobilities at increased gate bias could be observed in our experiments.

Investigated P3HT samples differed mainly in molecular weight $\mathrm{M_W}$ and in the case of P3HTTFT10 in composition. The impact of $\mathrm{M_W}$ on both mobility at room temperature and activation energy is in agreement with published data from other groups: when P3HT solvent deposition is done with low solvent evaporation rates, high $\mathrm{M_W}$ P3HT shows better mobilities and lower activation energy.

Other experiments done with P3HT based OFETs include post annealing, air exposure, effects of gate bias stressing and electrical characterisation at elevated temperatures. We could not achieve improved mobility upon annealing the devices, probably the film morphology was already relaxed into equilibrium state before annealing.

FETs that were briefly exposed to ambient air after their production showed a high irreversible increase of mobility, which still needs to be explained. Gate bias stressing was done indirectly as a consequence of testing higher integration times for each recorded data point by the parametric analyser. Increased integration times led to lower off currents but unfortunately also to higher hystereses in our curves. It was also tried to characterise the devices at higher temperatures than 300 K. Heating the devices with in-situ electrical measurements proved to yield poor results when done in the glovebox. The curves of heated devices showed very high hystereses.

Bibliography

[1] J. Pflaum S. Hirschmann W. Zhuang F. Jaiser U. Asawapirom J. ?P. Rabe U. Scherf D. Neher A. Zen. Effect of molecular weight and annealing of poly(3-hexylthiophene)s on the performance of organic field-effect transistors. *Advanced Functional Materials*, 14:757–764, 2004.

[2] A. N. Aleshin, H. Sandberg, and H. Stubb. Two-dimensional charge carrier mobility studies of regioregular p3ht. *Synthetic Metals*, 121:1449–1450, Mar 2001.

[3] Vinay Ambegaokar, B. I. Halperin, and J. S. Langer. Hopping conductivity in disordered systems. *Phys. Rev. B*, 4(8):2612–2620, Oct 1971.

[4] H. Bässler. Charge transport in disordered organic photoconductors a monte carlo simulation study. *physica status solidi (b)*, 175:15–56, 1993.

[5] A. R. Brown, C. P. Jarrett, D. M. de Leeuw, and M. Matters. Field-effect transistors made from solution-processed organic semiconductors. *Synthetic Metals*, 88:37–55, Apr 1997.

[6] L. Bürgi, T. J. Richards, R. H. Friend, and H. Sirringhaus. Close look at charge carrier injection in polymer field-effect transistors. *Journal of Applied Physics*, 94(9):6129–6137, 2003.

[7] L. Bürgi, H. Sirringhaus, and R. H. Friend. Noncontact potentiometry of polymer field-effect transistors. *Applied Physics Letters*, 80(16):2913–2915, 2002.

[8] Jui-Fen Chang, Jenny Clark, Ni Zhao, Henning Sirringhaus, Dag W. Breiby, Jens W. Andreasen, Martin M. Nielsen, Mark Giles, Martin Heeney, and Iain McCulloch. Molecular-weight dependence of interchain polaron delocalization and exciton bandwidth in high-mobility conjugated polymers. *Physical Review B (Condensed Matter and Materials Physics)*, 74(11):115318, 2006.

[9] Jui-Fen Chang, Henning Sirringhaus, Mark Giles, Martin Heeney, and Iain McCulloch. Relative importance of polaron activation and disorder on charge transport in high-mobility conjugated polymer field-effect transistors. *Physical Review B (Condensed Matter and Materials Physics)*, 76(20):205204, 2007.

[10] D. Chirvase, Z. Chiguvare, M. Knipper, J. Parisi, V. Dyakonov, and J. C. Hummelen. Electrical and optical design and characterisation of regioregular poly(3 -hexylthiophene-2,5diyl)/fullerene-based heterojunction polymer solar cells. *Synthetic Metals*, 138:299–304, Jun 2003.

[11] Shinuk Cho, Kwanghee Lee, Jonathan Yuen, Guangming Wang, Daniel Moses, Alan J. Heeger, Mathieu Surin, and Roberto Lazzaroni. Thermal annealing-induced enhancement of the field-effect mobility of regioregular poly(3-hexylthiophene) films. *Journal of Applied Physics*, 100(11):114503, 2006.

[12] Lay-Lay Chua, Jana Zaumseil, Jui-Fen Chang, Eric C. W. Ou, Peter K. H. Ho, Henning Sirringhaus, and Richard H. Friend. General observation of n-type field-effect behaviour in organic semiconductors. *Nature*, 434:194–199, Mar 2005. 10.1038/nature03376.

[13] J. T. Han Y. D. Park Y. Jang J. H. Cho M. Hwang K. Cho D. H. Kim. Single-crystal polythiophene microwires grown by self-assembly. *Advanced Materials*, 18:719–723, 2006.

[14] Jesús del Alamo. Microelectronic devices and circuits, lecture notes. MIT Open Courseware, 2005.

[15] A. S. Dhoot, G. M. Wang, D. Moses, and A. J. Heeger. Voltage-induced metal-insulator transition in polythiophene field-effect transistors. *Physical Review Letters*, 96(24):246403, 2006.

[16] Ananth Dodabalapur. Organic and polymer transistors for electronics. *Materials Today*, 9:24–30, Apr 2006.

[17] I. I. Fishchuk, V. I. Arkhipov, A. Kadashchuk, P. Heremans, and H. Bässler. Analytic model of hopping mobility at large charge carrier concentrations in disordered organic semiconductors: Polarons versus bare charge carriers. *Physical Review B (Condensed Matter and Materials Physics)*, 76(4):045210, 2007.

[18] Riadh Hajlaoui Habib Bouchriha Ramzi Bourguiga Mohcen Hajlaoui Gilles Horowitz. The concept of ldquothreshold voltagerdquo in organic field-effect transistors. *Advanced Materials*, 10:923–927, 1998.

[19] D. J. Gundlach, L. Zhou, J. A. Nichols, T. N. Jackson, P. V. Necliudov, and M. S. Shur. An experimental study of contact effects in organic thin film transistors. *Journal of Applied Physics*, 100(2):024509, 2006.

[20] S. Gunes, H. Neugebauer, and N.S. Sariciftci. Conjugated polymer-based organic solar cells. *Chemical Reviews*, 107(4):1324–1338, 2007.

[21] T. Hassenkam, D. R. Greve, and T. Bjørnholm. Direct visualization of the nanoscale morphology of conducting polythiophene monolayers studied by electrostatic force microscopy. *Advanced Materials*, 13:631–634, 2001.

[22] I. G. Hill. Numerical simulations of contact resistance in organic thin-film transistors. *Applied Physics Letters*, 87(16):163505, 2005.

[23] Tae Joo Shin Zhenan Bao Chang Y. Ryu Hoichang Yang. Structural transitions of nanocrystalline domains in regioregular poly(3-hexyl thiophene) thin films. *Journal of Polymer Science Part B: Polymer Physics*, 45:1303–1312, 2007.

[24] H. Hoppe and N. S. Sariciftci. Organic solar cells: An overview. *Journal of Materials Research*, 19:1924–1945, 2004.

[25] G. Horowitz, R. Hajlaoui, and F. Kouki. An analytical model for the organic field-effect transistor in the depletion mode. application to sexithiophene films and single crystals. *The European Physical Journal Applied Physics*, 1(3):361–367, mar 1998.

[26] Gilles Horowitz. *Organic Field-Effect Transistors*, chapter Charge Transport in Oligomers. CRC Press Taylor & Francis Group, 2007.

[27] G.R. Hutchison, M.A. Ratner, and T.J. Marks. Hopping transport in conductive heterocyclic oligomers: Reorganization energies and substituent effects. *Journal of the American Chemical Society*, 127(7):2339–2350, 2005.

[28] R. Jankowiak, K. D. Rockwitz, and H. Baessler. Adsorption spectroscopy of amorphous tetracene. *Journal of Physical Chemistry*, 87(4):552–557, 1983.

[29] G. Juška, K. Arlauskas, M. Viliūnas, and J. Kočka. Extraction current transients: New method of study of charge transport in microcrystalline silicon. *Phys. Rev. Lett.*, 84(21):4946–4949, May 2000.

[30] D.H. Kim, Y. Jang, Y.D. Park, and K. Cho. Layered molecular ordering of self-organized poly(3-hexylthiophene) thin films on hydrophobized surfaces. *Macromolecules*, 39(17):5843–5847, 2006.

[31] R.J. Kline, M.D. McGehee, E.N. Kadnikova, J. Liu, J.M.J. Frechet, and M.F. Toney. Dependence of regioregular poly(3-hexylthiophene) film morphology and field-effect mobility on molecular weight. *Macromolecules*, 38(8):3312–3319, 2005.

[32] Stergios Logothetidis. Flexible organic electronic devices: Materials, process and applications. *Materials Science and Engineering: B*, In Press, Corrected Proof, 2008.

[33] S. G. J. Mathijssen, M. Cölle, A. J. G. Mank, M. Kemerink, P. A. Bobbert, and D. M. de Leeuw. Scanning kelvin probe microscopy on organic field-effect transistors during gate bias stress. *Applied Physics Letters*, 90(19):192104, 2007.

[34] Richard D. McCullough. The chemistry of conducting polythiophenes. *Advanced Materials*, 10:93–116, 1998.

[35] Richard D. McCullough, Renae D. Lowe, Manikandan Jayaraman, and Deborah L. Anderson. Design, synthesis, and control of conducting polymer architectures: structurally homogeneous poly(3-alkylthiophenes). *The Journal of Organic Chemistry*, 58(4):904–912, 1993.

[36] Allen Miller and Elihu Abrahams. Impurity conduction at low concentrations. *Phys. Rev.*, 120(3):745–755, Nov 1960.

[37] N. F. Mott and E. A. Davis. *Electronic Processes in Non-Crystalline Materials.* Oxford University Press, 1979.

[38] M. Nonnenmacher, M. P. O'Boyle, and H. K. Wickramasinghe. Kelvin probe force microscopy. *Applied Physics Letters*, 58(25):2921–2923, 1991.

[39] S. V. Novikov, D. H. Dunlap, V. M. Kenkre, P. E. Parris, and A. V. Vannikov. Essential role of correlations in governing charge transport in disordered organic materials. *Phys. Rev. Lett.*, 81(20):4472–4475, Nov 1998.

[40] A. Ortiz-Conde, F. J. García Sánchez, J. J. Liou, A. Cerdeira, M. Estrada, and Y. Yue. A review of recent mosfet threshold voltage extraction methods. *Microelectronics Reliability*, 42:583–596, 00 2002.

[41] Matthew J. Panzer and C. Daniel Frisbie. *Organic Field-Effect Transistors*, chapter Contact Effect in Organic Fiel-Effect Transistors. CRC Press Taylor & Francis Group, 2007.

[42] L.-L. Chua M. Dipankar X.Y. Gao D.C. Qi A.T.-S. Wee J.-F. Chang R.H. Friend P.K.-H. Ho. Solvent effects on chain orientation and interchain π-interaction in conjugated polymer thin films: Direct measurements of the air and substrate interfaces by near-edge x-ray absorption spectroscopy. *Advanced Materials*, 19:215–221, 2007.

[43] V. Podzorov, E. Menard, J. A. Rogers, and M. E. Gershenson. Hall effect in the accumulation layers on the surface of organic semiconductors. *Physical Review Letters*, 95(22):226601, 2005.

[44] T.J. Prosa, M.J. Winokur, and R.D. McCullough. Evidence of a novel side chain structure in regioregular poly(3-alkylthiophenes). *Macromolecules*, 29(10):3654–3656, 1996.

[45] M. D. McGehee E. N. Kadnikova J. Liu J. M. J. Fréchet R. J. Kline. Controlling the field-effect mobility of regioregular polythiophene by changing the molecular weight. *Advanced Materials*, 15:1519–1522, 2003.

[46] N. Reitzel, D.R. Greve, K. Kjaer, P.B. Howes, M. Jayaraman, S. Savoy, R.D. McCullough, J.T. McDevitt, and T. Bjornholm. Self-assembly of conjugated polymers at the air/water interface. structure and properties of langmuir and langmuir-blodgett films of amphiphilic regioregular polythiophenes. *Journal of the American Chemical Society*, 122(24):5788–5800, 2000.

[47] Possaner S., Zojer K., Pacher P., Zojer E., and Schürrer F. Threshold voltage shifts in organic thin-film transistors due to self-assembled monolayers at the dielectric surface. Submitted to Advanced Functional Materials, 2008.

[48] D. Sainova, S. Janietz, U. Asawapirom, L. Romaner, E. Zojer, N. Koch, and A. Vollmer. Improving the stability of polymer fets by introducing fixed acceptor units into the main chain: Application to poly(alkylthiophenes). *Chemistry of Materials*, 19(6):1472–1481, 2007.

[49] A. Salleo, T. W. Chen, A. R. Völkel, Y. Wu, P. Liu, B. S. Ong, and R. A. Street. Intrinsic hole mobility and trapping in a regioregular poly(thiophene). *Phys. Rev. B*, 70(11):115311, Sep 2004.

[50] Alberto Salleo. Charge transport in polymeric transistors. *Materials Today*, 10:38–45, Mar 2007.

[51] DirkW. Schubert and Thomas Dunkel. Spin coating from a molecular point of view: its concentration regimes, influence of molar mass and distribution. *Materials Research Innovations*, 7:314–321, Oct 2003.

[52] Kazuhiko Seki and M. Tachiya. Electric field dependence of charge mobility in energetically disordered materials: Polaron aspects. *Phys. Rev. B*, 65(1):014305, Dec 2001.

[53] H. Sirringhaus, P. J. Brown, R. H. Friend, M. M. Nielsen, K. Bechgaard, B. M. W. Langeveld-Voss, A. J. H. Spiering, R. A. J. Janssen, E. W. Meijer, P. Herwig, and D. M. de Leeuw. Two-dimensional charge transport in self-organized, high-mobility conjugated polymers. *Nature*, 401:685–688, Oct 1999. 10.1038/44359.

[54] H. Sirringhaus, N. Tessler, and R. H. Friend. Integrated, high-mobility polymer field-effect transistors driving polymer light-emitting diodes. *Synthetic Metals*, 102:857–860, Jun 1999.

[55] G. Slanitsch. Oxidative defekte in konjugierten polymeren und deren einfluss auf den ladungstransport. Master's thesis, University of Technology TU-Graz, Graz, 2005.

[56] R. A. Street, W. S. Wong, S. E. Ready, M. L. Chabinyc, A. C. Arias, S. Limb, A. Salleo, and R. Lujan. Jet printing flexible displays. *Materials Today*, 9:32–37, Apr 2006.

[57] Robert A. Street. *Hydrogenated amorphous silicon.* Cambridge University Press, 1991.

[58] Cristina Tanase. *Unified charge transport in disordered organic field-effect transistors and light-emitting diodes.* PhD thesis, University of Groningen, 2005.

[59] V. Kažukauskas, M. Pranaitis, V. Čyras, L. Sicot, and F. Kajzar. Negative mobility dependence in polythiophenes p3ot and p3ht evidenced by the charge extraction by linearly increasing voltage method. *The European Physical Journal Applied Physics*, 37(3):247–251, mar 2007.

[60] M. C. J. M. Vissenberg and M. Matters. Theory of the field-effect mobility in amorphous organic transistors. *Phys. Rev. B*, 57(20):12964–12967, May 1998.

[61] Takakazu Yamamoto, Atsushi Morita, Yuichi Miyazaki, Tsukasa Maruyama, Hiroshi Wakayama, Zhen Hua Zhou, Yoshiyuki Nakamura, Takaki Kanbara, Shintaro Sasaki, and Kenji Kubota. Preparation of π-conjugated poly(thiophene-2,5-diyl), poly(p-phenylene), and related polymers using zerovalent nickel complexes. linear structure and properties of the π-conjugated polymers. *Macromolecules*, 25(4):1214–1223, 1992.

[62] H. Yang, T. J. Shin, L. Yang, K. Cho, C. Y. Ryu, and Z. Bao. Effect of mesoscale crystalline structure on the field-effect mobility of regioregular poly(3-hexyl thiophene) in thin-film transistors. *Advanced Functional Materials*, 15:671–676, 2005.

[63] George M. Whitesides Younan Xia. Soft lithography. *Angewandte Chemie International Edition*, 37:550–575, 1998.

[64] R. Zhang, B. Li, M.C. Iovu, M. Jeffries-EL, G. Sauve, J. Cooper, S. Jia, S. Tristram-Nagle, D.M. Smilgies, D.N. Lambeth, R.D. McCullough, and T. Kowalewski. Nanostructure dependence of field-effect mobility in regioregular poly(3-hexylthiophene) thin film field effect transistors. *Journal of the American Chemical Society*, 128(11):3480–3481, 2006.